Modelling and Testing of a Piezoelectric Sensor for Defect Detection in Steel Rods using Acoustic Guided Waves

by

Nicholas Benjamin Durham

A thesis submitted to

the Faculty of Graduate Studies

In partial fulfilment of

the requirements of the degree of

Master of Science

Department of Electrical and Computer Engineering

University of Manitoba

Winnipeg, Manitoba

August 21, 2018

Abstract

Corrosion in grounding electrodes is an emerging problem affecting electric power distribution systems worldwide. An effective means to detect acute corrosion within specific grounding rods remains elusive. However, a promising method for corrosion detection is being explored that is based on acoustic guided waves. An acoustic pulse is transmitted into a steel rod using a piezoelectric element. The transmitted wave echoes off of any defects which may be present, letting their size and location be made known. A transducer is developed that best transmits the longitudinal mode into the rod. A novel model of the pulse-echo system using PSpice is presented. The model is compared with lab experiments using frequency and time domain testing and show that our model is in close agreement with the lab measurements. A novel pulse-echo transceiver embedded system is developed and presented for use in field testing. Measurements obtained from the board are compared with bench-top equipment to verify accuracy and quality.

Table of Contents

Abstract ii

Table of Contents iii

Table of Figures x

1 Introduction 1

1.1 Pulse-Echo Method for Defect Detection 2

1.1.1 Description of Method 2

1.1.2 Pulse-Echo Method in Literature 3

1.2 Modelling of Piezoelectric Transducers 4

1.3 Scope of this Work 5

2 Derivation of Theory Relevant to Model 6

2.1 Equations Governing a Piezoelectric Medium 6

2.2 Characterization of Piezoelectric Transducers from Impedance Spectra 8

2.3 Leach's Controlled Source Analogous Circuit for Piezoelectric Transducers 10

2.3.1 Electric Analogous Circuit Implementation of Leach's Model 12

2.4 Development of Electrical Analogous Circuit for a Lossy Piezoelectric Transducer.... 14

2.5 Modelling Wave Propagation in Solids 16

2.6 Propagating Waves Incident on a Boundary 17

3 Initial Model with Symmetric Acoustic Load 19

3.1 Initial Model 19

3.2 Symmetric Acoustic Load Test of PSpice Model 21

3.2.1 Lab Setup for Symmetric Acoustic Load Test 21

3.2.2 PSpice Model of acoustic symmetric load test 22

3.2.3 Testing and Discussion of Results 23

3.3 Conclusions 24

4 Development of Specialized Corrosion Detection Sensor 26

4.1 Clamped Sensor Configuration 27

4.1.1 Discussion and Results of Testing with Clamped Configuration 29

4.2 Mass Backed Piezos 30

4.2.1 Discussion and Results of Testing with Mass-Backed Configuration 32

4.3 Development of the CRAS Sensor 33

4.3.1 Time Domain Response of CRAS sensor 37

4.4 Conclusions 38

5 Lossy Piezo Transducer Modelling in PSpice 40

5.1 Determination of Piezoelectric Electromechanical Constants 41

5.1.1 First Fit Applied to Piezo Resonant Curve using PRAP 42

5.1.2 Second Fit Applied to Piezo Resonant Curve using PRAP 43

5.1.3 Comparison of Results 44

5.2 Modelling Standalone Piezo Transducer 45

5.2.1 PSpice Implementation of Standalone Piezo Transducer Model 45

5.2.2 Testing and Results of Standalone Piezo Model 46

5.3 PSpice Modelling of First CRAS Variant 47

5.3.1 PSpice Schematic for First CRAS variant 48

5.3.2 Testing and Results of first CRAS variant PSpice Model 50

5.4 PSpice Modelling of Second CRAS Variant 53

5.4.1 PSpice Schematic of Second CRAS Variant 53

5.4.2 Testing and Results of Second Constructed Sensor Model 53

5.5 Conclusions 56

6 Modelling Corrosion Detection in Grounding Rods 58

6.1 Modelling Defect Detection Using Rod A 59

6.1.1 Simulation Results for Rod A at 32.5 kHz 60

6.1.2 Simulation Results for Rod A at 40 kHz 61

6.1.3 Simulation Results for Rod A at 50 kHz. 62

6.2 Modelling Defect Detection Using Rod D 63

6.2.1 Simulation Results for Rod D at 32.5 kHz 64

6.2.2 Simulation Results for Rod D at 40 kHz. 65

6.2.3 Simulation Results for Rod D at 50 kHz 66

6.3 Modelling Defect Detection Using Rod E 66

6.3.1 Simulation Results for Rod E at 32.5 kHz. 67

6.3.2 Simulation Results for Rod E at 40 kHz 68

6.3.3 Simulation Results for Rod E at 50 kHz 69

6.4 Conclusions 70

7 Hardware Implementation 71

7.1 Introduction 71

7.2 System Requirements 71

7.3 System Description 72

7.4 User Interface 73

7.4.1 Push Button Circuit 73

7.4.2 LED Feedback 73

7.5 Power Supplies 74

7.5.1 +5 VDC Converter 74

7.5.2 +12 VDC Supply 75

7.5.3 −12 VDC Converter 75

7.5.4 Teensy 3.6 Microcontroller 76

7.5.5 RTC Battery 77

7.6 Custom DAC Implementation 78

7.6.1 Voltage Sample Outputs from PIT IRQ Vector 78

7.6.2 Implementation of DAC Using an R2R Ladder 79

7.7 Output Circuit 80

7.7.1 Output Filter 81

7.7.2 Output Amplifier 82

7.7.3 Piezo Out 82

7.8 ADC Implementation 82

7.8.1 Configuration of ADCK 82

7.8.2 Determination of ADC Sampling Frequency from ADCK 83

7.9 Input Circuit 83

7.9.1 Piezo In 84

7.9.2 Input Filter 1 84

7.9.3 Input Amplifier 85

7.9.4 Input Filter 2 85

7.9.5 Clipping Circuit 86

7.9.6 Biasing Circuit 86

7.9.7 ADC Input 86

7.10 PCB Implementation 87

7.11 Testing and Results 88

7.11.1 DAC Testing 88

7.11.2 ADC Jitter Testing 90

7.11.3 Results of Sampling Repeatability Test 91

7.12 Comparison of Pulse-Echo Measurements with Digital Oscilloscope 95

7.13 Conclusions 100

8 Conclusions and Future Work 101

References 104

Table of Figures

Figure 2.1: Diagram of thickness-mode piezo transducer for reference 7

Figure 2.2: Electrical analogous circuit representation of electromechanical equations for piezo transducer, figure inspired by the one presented in Leach's work [13] 13

Figure 2.3: Typical rod with length L_{Rod} and defect length $L_{Defect.}$This situation can be modelled as three transmission lines in series as shown in the figure 17

Figure 3.1: PSpice Schematic of the simplified piezo transducer circuit model 19

Figure 3.2: Lab test setup for verification of circuit model in PSPICE. Two rods of equal lengths are placed on either side of the PZT transducer, and transverse waves travel symmetrically in their respective wave guides. 21

Figure 3.3: PSpice schematic of the model for the matched acoustic load test 22

Figure 3.4: Comparison of simulation to experiment for a symmetrically driven pair of rods. Shown here are three consecutive wave pulse reflections off the end of each rod. See Fig. 3 for a description of the test setup..... 24

Figure 4.1 Diagram representing the three different rods used in experiments for this work 26

Figure 4.2: Lab setup of clamped piezo configuration. Depicted are the two sets of clamps (A), having one pair of driving piezos and one pair of receiving piezos. A small backing mass (B) is

applied to the non-driving side of the piezos to provide motional inertia for better vibration generation into the rods 28

Figure 4.3: Results of testing on Rod D (top), and Rod A (bottom) for Clamped Configuration. Testing performed at 55 kHz and 5 Vpp applied to test sensor. 30

Figure 4.4 Diagram showing how the mass backed piezo transducer is fixed to the test rod, and the lab test setup 31

Figure 4.5: Picture of mass-backed piezo used in the experiment from section 4.2 32

Figure 4.6: Results of testing on Rod D (top), and Rod A (bottom) for mass-backed configuration. Testing performed at 75 kHz and 500 mVpp applied to piezo 33

Figure 4.7: Diagram of the all Ag-Epoxy constructed piezo transducer variant developed by Zhao and Thomson. The resonator is composed of four different components, silver epoxy, brass electrodes, PZT sensors, and steel end pieces 34

Figure 4.8 Picture of the actual CRAS transducer used in the experiments 35

Figure 4.9 Picture of lab setup for analyzing the impedance behaviour of the transducers in this work using the Agilent E4990A Impedance Analyzer 35

Figure 4.10: Impedance vs. Frequency curves for the two CRAS variations developed by Zhao and Thomson. The first variation uses a combination of polymeric epoxy and silver epoxy to hold the pieces together, and the second variation uses only silver epoxy. 36

Figure 4.11: Diagram showing the pulse-echo experiment for CRAS sensor connected to the test rod 37

Figure 4.12: Results of testing on Rod A (top), and Rod D (bottom) for CRAS Configuration. Testing performed at resonant frequency of sensor, 40 kHz, with 500 mVpp applied to transmitting piezo. 38

Figure 5.1: The first fit performed in PRAP. Fitting is applied to the tall parallel resonance peak of the impedance curve for the 1.21 mm transducer near its rated resonant frequency. 42

Figure 5.2: The second fit performed in PRAP. Fitting is applied to the wide parallel resonance of the impedance curve for the 1.21 mm transducer near its rated resonance 44

Figure 5.3: The model for the standalone piezoelectric transducer implemented in PSpice. 46

Figure 5.4: |Z| vs frequency A comparison of the results obtained for the different modelling parameters obtained from PRAP software. 47

Figure 5.5: Block diagram of PSpice model for the CRAS sensor, from Chapter 4. The two CRAS variations have identical topologies but differ in the elements that make up the Left and Right Sensor Sections. 48

Figure 5.6 PSpice implementation of the Left Sensor Section from Fig. 5.5 48

Figure 5.7 PSpice implementation of the Left Piezo, Epoxy + Electrode, and Right Piezo Sections from Fig. 5.5. 49

Figure 5.8 PSpice implementation of the Left Sensor Section from Fig. 5.5 49

Figure 5.9 PSpice implementation of the Electric Circuit Left and Electric Circuit Right Piezos from Fig. 5.5 49

Figure 5.10: Frequency Response of first CRAS sensor with frequency response of the PSpice model..... 51

Figure 5.11: The time domain response of the first CRAS sensor. The stimulus is a 5 cycle sine burst, 250 mVpp. at the resonant frequency of the sensor, 52 kHz. 52

Figure 5.12 PSpice implementation of Left Sensor Section for second CRAS variation, with reference to Fig. 5.5 53

Figure 5.13 PSpice implementation of Right Sensor Section for second CRAS variation, with reference to Fig. 5.5 53

Figure 5.14: Frequency Response of second CRAS sensor compared with frequency response of the PSpice model..... 54

Figure 5.15: The time domain response of the second CRAS sensor. The stimulus is a 5 cycle sinusoidal burst, 200 mVpp. at the resonant frequency of the sensor, 40 kHz. 56

Figure 6.1: Block diagram of corrosion detection model in PSpice. The rod model is connected in series with the CRAS model presented in Chapter 5. 58

Figure 6.2: Schematic of Rod A PSpice model. Connector marked “To Sensor" indicates where the rod model is connected to the CRAS model introduced in Chapter 5 59

Figure 6.3: Simulation and Lab results of CRAS sensor connected to Rod A, excited at 32.5 kHz, 5 cycle sine burst at 2 Vpp 60

Figure 6.4: Simulation and Lab results of CRAS sensor connected to Rod A, excited at 40 kHz, 5 cycle sine burst at 2 Vpp 61

Figure 6.5: Simulation and Lab results of CRAS sensor for Rod A, excited at 50 kHz, 5 cycle sine burst at 2 Vpp 62

Figure 6.6: Schematic of Rod D PSpice model. Connect marked “To Sensor" indicates where the rod model is connected to the CRAS model from Chapter 5 63

Figure 6.7 Simulation and Lab results of CRAS sensor connected to Rod D, excited at 32.5 kHz, 5 cycle sine burst at 2 Vpp 64

Figure 6.8 Simulation and Lab results of CRAS sensor connected to Rod D, excited at 40 kHz, 5 cycle sine burst at 2 Vpp 65

Figure 6.9: Simulation and Lab results of CRAS sensor connected to Rod D, excited at 40 kHz, 5 cycle sine burst at 2 Vpp 66

Figure 6.10: Schematic of Rod D PSpice model. Connect marked “To Sensor" indicates where the rod model is connected to the CRAS model from Chapter 5 67

Figure 6.11: Simulation and Lab results of CRAS sensor connected to Rod E, excited at 32.5 kHz, 5 cycle sine burst at 2 Vpp 68

Figure 6.12: Simulation and Lab results of CRAS sensor connected to Rod E, excited at 40 kHz, 5 cycle sine burst at 2 Vpp 69

Figure 6.13: Simulation and Lab results of CRAS sensor connected to Rod E, excited at 50 kHz, 5 cycle sine burst at 2 Vpp 69

Figure 7.1: Block diagram for the implementation of the pulse-echo transceiver board 72

Figure 7.2: Diagram for 5VDC Converter 74

Figure 7.3: Diagram for -12VDC Converter 75

Figure 7.4: Pinout diagram of Teensy 3.6 by PJRC 76

Figure 7.5: Diagram showing the 8 bits of Port D from Teensy MCU to DAC R2R ladder 79

Figure 7.6: Figure for voltage steps of DAC 80

Figure 7.7: Schematic of Output Amplifier Circuit 81

Figure 7.8 Schematic showing the implementation of the input circuit conditioning the signal from the piezo transducer 84

Figure 7.9: PCB Implementation of the Pulse-Echo Transceiver system 87

Figure 7.10 Results of frequency measurement experiment verifying the DAC Output 89

Figure 7.11: Diagram illustrating nature of the sampling repeatability test 90

Figure 7.12: Typical-case response of Jitter Test for ADCK = 20 MHz, 20% Duty Cycle 92

Figure 7.13: Worst-case response of Jitter test for ADCK = 20 MHz, 70% Duty Cycle 92

Figure 7.14: Best-case response of Jitter test for ADCK = 20 MHz, 50% Duty Cycle..... 93

Figure 7.15: Typical-case response of Jitter Test for ADCK = 24 MHz, 50% Duty Cycle 93

Figure 7.16: Worst-case response of Jitter test for ADCK = 24 MHz, 20% Duty Cycle 94

Figure 7.17: Best-case response of Jitter test for ADCK = 24 MHz, 40% Duty Cycle..... 94

Figure 7.18: Comparison of board measurement to oscilloscope for Rod A at 32.5 kHz 95

Figure 7.19: Comparison of board measurement to oscilloscope for Rod A at 40 kHz 96

Figure 7.20: Comparison of board measurement to oscilloscope for Rod A at 50 kHz 96

Figure 7.21: Comparison of board measurement to oscilloscope for Rod D at 32.5 kHz 97

Figure 7.22: Comparison of board measurement to oscilloscope for Rod D at 40 kHz 97

Figure 7.23: Comparison of board measurement to oscilloscope for Rod D at 50 kHz 98

Figure 7.24: Comparison of board measurement to oscilloscope for Rod E at 32.5 kHz 98

Figure 7.25: Comparison of board measurement to oscilloscope for Rod E at 40 kHz 99

Figure 7.26: Comparison of board measurement to oscilloscope for Rod E at 40 kHz 99

1 Introduction

Corrosion in grounding electrodes is an emerging problem in electric power distribution systems. As electric substations age, their grounding networks suffer more and more from the effects of corrosion, but maintaining their integrity is paramount to protect the substations and those who interact with them. It is especially difficult to proactively manage the deterioration of grounding networks because the nature of their existence is to be below the ground surface. Thus, the direct visual inspection of the numerous individual rods in a particular grounding network would require excavation which is expensive and cumbersome. Grounding networks, and the electrodes which constitute them, protect the substation from electrical disturbances such as lightning strikes or grounding faults of nearby equipment. Thus, a corroded grounding network directly presents a hazard to human safety [1]. If a grounding electrode corrodes, its electrical properties can be altered such that it can no longer provide the same level of protection to the surrounding area. In many cases, the corrosion can affect a wide area of electrodes within a substation, and if not detected, there is a significant risk of injury or equipment damage [1].

Currently, the most common means of detecting corrosion in grounding electrodes is to excavate them and perform visual inspection, which is cumbersome, costly and time consuming. Another common technique for determining the condition of the grounding grid involves measuring the soil conductivity. This method is effective at determining the overall condition of the grounding grid, but it does not provide a means to locate acute corrosion within it, nor can it necessarily determine which ground rod needs to be replaced [2]. Without the ability to locate acute corrosion within a grid, there are currently only two options for a utility: Replace all or part of a grounding

network, including those electrodes in good condition, or leave any corrosion within it largely unresolved. Therefore, the need arises for an efficient method to detect acute corrosion in a grounding network that requires little to no excavation. In this work we explore a pulse-echo method for the detection of corrosion within grounding rods.

1.1 Pulse-Echo Method for Defect Detection

1.1.1 Description of Method

The pulse-echo method is an imaging technique for the detection of defects in a solid using ultrasonic waves [3]. The general principle is that an acoustic pulse is generated by means of a transducer, and is transmitted into a material that acts as a waveguide. Once in the waveguide, assuming the dimensions of the waveguide are finite, the pulse travels unimpeded until it reaches the boundaries of the material, or some defect within it. A defect can take the form of cracks, air gaps, or a region of the material where the material properties have been altered in some way. At the defect/waveguide boundary, a portion of the incident pulse will reflect off the boundary, and the remainder will pass through the boundary. Part of the reflected wave, or echo, travels back to the transmitter, and carries with it information about the location of the defect. Commonly this information is extracted through a method known as time of flight (TOF) [3]. If the material properties of the waveguide are well known, then the velocity of the wave travelling in the material will also be known [4]. The location of the defect can be determined indirectly by first dividing the velocity of the travelling wave u, by the time elapsed from the pulse to the recorded echo Δt, and finally multiplying the result by one half; this factor of half is necessary since the wave travels

twice the desired distance in its journey from the transmitter, to the defect/waveguide boundary and then back to the transmitter [3].

1.1.2 Pulse-Echo Method in Literature

Piezoelectric pulse-echo techniques are a promising class of methods for effective defect detection. Researchers at Nippon Telegraph and Telephone Corporation (NTT) [5], [6] utilized a pulse-echo method for detecting corrosion in anchoring rods. In their work, the L(0,1) longitudinal wave mode was selectively generated by shear-mode piezoelectric transducers mounted on the side of the rod. Their experiments confirmed that the L(0,1) mode was optimum for inspecting steel anchor rods using acoustic guided waves due to the low attenuation of this mode in the selected frequency range [5], [6]. In their work a frequency of 60 kHz was selected [5], [6]. However, shear-mode transducers are more difficult to use with grounding electrodes since the entirety of their lengths are subsurface. Therefore, significant excavation would be required to mount the test apparatus to the rods effectively. Furthermore, the apparatuses that induce the longitudinal waves from shear-mode transducers add undesirable mechanical responses that obscure the response near to the surface of the rod. Shoji and Hirata created artificial defects in the test rods by removing a part of the rods cross-section at 0.5 m from the end of the rod. They performed testing to record reflections of the guided wave off of the defects. Shoji and Hirata explored the mechanical behavior of the rod but did not develop electrical models to predict the electro-mechanical coupling between the transducer and the rods.

Amjad et al. showed that the time of flight (TOF) of the L(0,1) mode was strongly affected by the level of corrosion present in steel bars [7]. Zheng and Lei investigated how the propagation of

guided waves in steel bars were affected by changing the physical properties of the surrounding concrete [8]. Sharma and Mukherjee successfully quantified the location and severity of simulated defects in steel reinforcing bars using a pulse-echo method [9]. They further showed that the progress of freshly poured concrete can be monitored through the use of embedded piezoelectric sensors on steel reinforcing bars [10]. Ervin et al. demonstrated that higher order longitudinal wave modes were useful for detecting uniform cross-sectional loss on steel bars embedded in mortar, particularly in the early stages of corrosion [11], [12].

1.2 Modelling of Piezoelectric Transducers

For most applications, having an accurate model of the piezoelectric transducer can improve the transducer design by providing insight that would not otherwise be possible. Methods for modelling the piezoelectric element have been widely reported in literature [13]–[19]. These techniques include RLC equivalent circuit models [15], [17], [20], Finite Element Methods (FEM) [14], and electrical analogous circuits using transmission lines [13], [18], [19]. In particular the Electrical Analogous Circuit model, first presented by Leach [13], presents an intuitive method for modelling the piezo transducer that is easily combined with other elements using transmission line theory [18], [21]. Leach introduced his electrical analogous equivalent circuit for the piezo transducer which could be implemented in PSpice [13]. In his work dependent voltage sources were used to model the conversion of electrical field to mechanical vibration and vice versa. He found this method was superior to previous methods involving ideal transformers presented by Mason and Redwood [15], [17]. As Leach points out, transmission line methods are more intuitive

than transformer methods since the transmission line model is conceptually easier to grasp than the transformer model [13].

1.3 Scope of this Work

In this work we explore the transmission line model implemented in PSpice for modelling a piezoelectric-based transducer used for defect detection in grounding rods. To aid in the design of future defect detection systems, a complete system model is desired, including the piezo-based transducer, its constituent elements, and the grounding electrode with and without defects. In Chapter 2 the theory related to modelling the defect detection system is presented. Then, in Chapter 3 a simplified model of the piezo transducer is presented that directly follows the lossless PSpice implementation presented by Leach [13]. From this initial modelling a piezoelectric sensor design is developed and presented in Chapter 4. An improved model of the piezo transducer which includes loss is presented in Chapter 5. In Chapter 6 the transducer model is combined with a model for the grounding rod to complete the defect detection model. Finally, in Chapter 7 the design and implementation of a hardware prototype of the defect detection system is presented.

2 Derivation of Theory Relevant to Model

In this chapter the equations and theory necessary for deriving the model of the Constructed Resonant Actuating Sensor (CRAS) [22] are developed. First the equations governing the electromechanical behavior of piezo ceramics are presented in Section 2.1. In Section 2.2, the equations for deriving the piezoelectric, elastic, and dielectric constants from the resonance spectra of piezo transducers are presented. In Section 2.3, the derivation of Leach's model for the electrical analogous circuit of a piezoelectric transducer [13] is expanded and presented. In Section 2.4, the work by Puttmer et al. [19] is presented which extends the lossless transmission line model developed by Leach to model lossy piezoelectric transducers. Finally, a brief discussion on wave motion in elastic solids is presented in Section 2.5, necessary for modelling acoustic waves travelling in elastic solid media.

2.1 Equations Governing a Piezoelectric Medium

The characterization of piezoelectric materials has been well documented in literature. Mason [17] derives the piezoelectric equations relating the tensors stress (T) and strain (S) to the vectors electric field ($\vec{E}$) and electric displacement ($\vec{D}$). These equations make use of piezoelectric constants relating T and S to $\vec{E}$ and $\vec{D}$, elastic constants relating T to S, and dielectric constants relating $\vec{E}$ to $\vec{D}$ [17]. The equations governing these relationships are geometry dependent, and many different variations of the equations can be derived based on the geometry of the piezoelectric transducer being considered [16].

Figure 2.1, inspired by [14], gives an illustration of a piezo transducer subject to an electric field, with vectors 1, 2, and 3 necessary for describing the constants which characterize it [14], [16]. With reference to Fig. 2.1, only those equations relating T, S, $\vec{E}$ and $\vec{D}$ in the 3 direction will be considered. In literature the 1, 2 and 3 notation is used in describing piezoelectric equations. The single subscript (e.g. $\vec{X}_i$) denotes that the vector $\vec{X}$ is with respect to the i direction, and the double subscript (e.g. x_{ij}) denotes a constant x relating some vector in the i direction to another vector in the j direction, where i and j can be 1, 2 or 3. Superscripts (e.g. x_{ij}^{y}) denote that y is held constant the determination of the constant x_{ij} from the relevant piezoelectric equation.

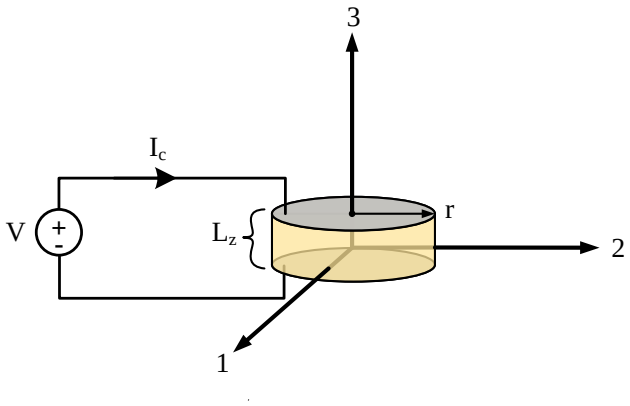

Figure 2.1: Diagram of thickness-mode piezo transducer for reference

From Mason, the piezoelectric equations for the thickness mode piezoelectric transducer, describing the relationship between T_3, S_3, $\vec{E}_3$ and $\vec{D}_3$, with S_3 and $\vec{D}_3$ as the independent variables, are [17]:

$$T_3 = c_{33}^{D} S_3 - h_{33} D_3 \tag{2.1}$$

$$E_3 = -h_{33} S_3 + \mathrm{D}_3/\varepsilon_{33}^{\mathrm{S}} \tag{2.2}$$

Where c_{33}^{D} is the stiffness elastic constant with $\vec{D}$ held constant, h_{33} is the piezoelectric constant, and ε_{33}^{S} is the permittivity with S held constant or clamped permittivity [16], [17].

2.2 Characterization of Piezoelectric Transducers from Impedance Spectra

The piezoelectric equations introduced in Section 2.2 make use of piezoelectric, dielectric and elastic constants relating tensors to vectors. These constants are difficult to measure directly [16], and often their values are found by analyzing the impedance versus frequency behavior of the transducer. Sherrit and Mukherjee present a derivation of the electromechanical equations governing a piezo transducer and how these constants can be found from their impedance spectra [16]. Only the relevant equations to this work are presented here, and the reader is encouraged to refer to their work for the full derivation. For a thickness-extensional transducer, the impedance of a piezo transducer as a function of frequency is given as [16]:

$$Z(\omega) = \frac{L_z}{j\omega \varepsilon_{33}^{S} A_z}\left(1 - \frac{k_t^2 \tan(\omega/f_p)}{\omega/4f_p}\right) \tag{2.3}$$

Where A_z is the cross-sectional area of the piezo in the z-direction, ω is the radial frequency, L_z is the thickness of the transducer, and k_t is the electromechanical coupling coefficient. The parallel resonant frequency f_p is where the resistance versus frequency spectrum is maximum, and is in contrast with the series resonant frequency f_s where the resistance spectrum is minimum. The first constant that can be obtained from the resonance curve is the elastic stiffness according to the equation:

$$c_{33}^{D} = 4\rho_{piezo} L_z^2 {f_p}^2 \tag{2.4}$$

The electromechanical coefficient k_t is related to f_s and f_p by the following equation:

$$k_t^2 = \frac{\pi}{2}\frac{f_s}{f_p}\tan\left[\frac{\pi}{2}\left(1-\frac{f_s}{f_p}\right)\right] \tag{2.5}$$

The piezoelectric constant h_{33} can be found from the coupling coefficient and the permittivity, using:

$$h_{33} = \sqrt{\frac{k_t^2 c_{33}^D}{\varepsilon_{33}^S}} \tag{2.6}$$

If (2.3) is rewritten in the following form:

$$Z(\omega) = a(\omega)A + b(\omega)B \tag{2.7}$$

with $a(\omega), b(\omega)$, A and B defined as:

$$a(\omega) = \frac{L_z}{j\omega A_z} \tag{2.8}$$

$$b(\omega) = \frac{4L_z f_p \tan\left(\frac{\omega}{4f_p}\right)}{j\omega^2 A_z} \tag{2.9}$$

$$A = \frac{1}{\varepsilon_{33}^S} \tag{2.10}$$

$$B = \frac{k_t^2}{\varepsilon_{33}^S} \tag{2.11}$$

One can apply a fitting algorithm to (2.7) and determine the coefficients from (2.8) – (2.11). Many curve fitting algorithms exist that are capable of fitting a curve to a given equation [14]. PRAP software is especially useful for fitting (2.7) to the resonance spectra of thickness-extensional piezoelectric transducers. PRAP and its usefulness is discussed in greater detail in Chapter 5 [23].

2.3 Leach's Controlled Source Analogous Circuit for Piezoelectric Transducers

Leach presents the development of a PSpice model for a lossless, thickness-mode piezoelectric transducer. He develops his model for the thickness mode transducer using (2.1) and (2.2). The derivation of his model is as follows [13]:

If S_3 is made equal to the differential particle displacement with respect to the z-direction $d\zeta/dz$, and T_3 is made equal and opposite to the ratio of force F to A_z then (2.1) and (2.2) become:

$$c_{33}^{D}\frac{d\zeta}{dz} = -\frac{1}{A_z}F + h_{33}D_3 \tag{2.12}$$

$$E_3 = -h_{33}\frac{d\zeta}{dz} + \frac{1}{\varepsilon_{33}^{S}}D \tag{2.13}$$

The differential force in terms of the particle velocity u and the Laplace variable s given as:

$$\frac{dF}{dz} = -\rho_{piezo}A_z s u \tag{2.14}$$

The total charge present on the electrodes of the ceramic, Q is related to the current I_c from Fig. 2.1 by:

$$Q = \frac{I_c}{s} \tag{2.15}$$

Since electric field intensity is charge per unit area, the electric field intensity is then related to current using the following equation:

$$D_3 = \frac{I_c}{A_z s} \tag{2.16}$$

The particle displacement is related to the particle velocity by the relationship:

$$\zeta = u/s \tag{2.17}$$

Leach then adds the term $-d(hI_c/s)/dz$ to (2.14). Since $dD/dz = 0$, this added term has no effect on the equation. Adding this term, and substituting (2.15) – (2.17), (2.12) and (2.14) become:

$$\frac{du}{dz} = -\frac{s}{c_{33}^D A_z}\left(F - \frac{hI_c}{s}\right) \tag{2.18}$$

$$\frac{d}{dz}\left(F - \frac{hI_c}{s}\right) = -\rho_{piezo} A_z s u \tag{2.19}$$

Leach then points out that his (2.18) and (2.19) are now in the form of the telegraphist's equations for the voltage V_T and current I_T of an electrical transmission line:

$$\frac{dV_T}{dz} = -LsI_T \tag{2.20}$$

$$\frac{dI_T}{dz} = -CsV \tag{2.21}$$

Leach shows that (2.18) and (2.19) can be made analogous to the telegraphist equations by making V_T analogous to the quantity $(F - hI_c/s)$, and the current I_T analogous to the particle velocity u. Thus, a transmission line model for (2.18) and (2.19) can be obtained where the per unit inductance and per unit capacitance of the analogous transmission line are found using:

$$L' = \rho_{piezo} A_z \tag{2.22}$$

$$C' = \frac{1}{c_{33}^D A_z} \tag{2.23}$$

Therefore, wave motion in the piezo ceramic as a function of the applied electric field can be modelled as an electrical transmission line, whose per unit parameters are analogous to the piezo ceramic material parameters according to (2.22) and (2.23).

The equations presented so far model the forward piezoelectric equations, those which govern the relationship between the applied electric field into mechanical strain. To incorporate the converse relationship (i.e. strain inducing an electric field), (2.16) and (2.17) are first substituted into (2.13) to obtain:

$$E_3 = -h_{33}\frac{du}{dz}\frac{1}{\mathrm{s}} + \frac{1}{\varepsilon_{33}^S}\frac{I_c}{A_z s} \tag{2.24}$$

Then, (2.24) is integrated in the z-direction over the piezo thickness from $z = 0$, to $z = L_z$ to obtain the voltage induced in the ceramic as function of the applied stress:

$$V = \frac{h_{33}}{s}(u_1 - u_2) + \frac{1}{C_0 s}I_c \tag{2.25}$$

Where the piezo transducer's static capacitance is found according to the well-known relation:

$$C_0 = \frac{\varepsilon_{33}^S A_z}{L_z} \tag{2.26}$$

From (2.25) we observe the term $\mathrm{h}(u_1 - u_2)/s$ is the change in particle displacement on either side of the transducer with $u_1 = u(z = 0)$ and $u_2 = u(z = l_z)$.

2.3.1 Electric Analogous Circuit Implementation of Leach's Model

Equations (2.18) (2.19) and (2.25) can be combined to give a complete model for a lossless piezoelectric transducer as shown in Fig. 2.2, inspired by the figure from Leach's work [13].

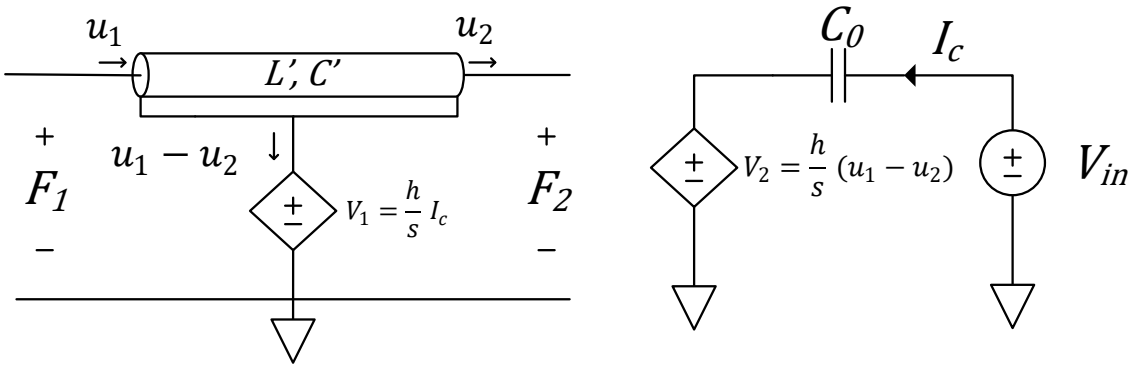

Figure 2.2: Electrical analogous circuit representation of electromechanical equations for piezo transducer, figure inspired by the one presented in Leach's work [13]

Equations (2.18) and (2.19) are realized by the circuit on the LHS of Fig. 2.2, by means of the transmission line and the controlled source V_1. The voltage on the transmission line is analogous to the quantity $(F - hI_c/s)$, and V_1 implements the hI_c/s term. Thus the net voltage on the transmission line is the difference between the voltage present on the line, $F = F_1 - F_2$ and the voltage of the source V_1. The circuit on the RHS of Fig. 2.2 realizes (2.25) via the controlled source V_2. The current $(u_1 - u_2)$ is multiplied by h and integrated via the s operator. Hence, the electrical circuit realizes the converse electromechanical behavior of the piezo transducer.

This equivalent circuit can be implemented in PSpice using an ideal lossless transmission line, and two controlled sources. PSpice offers the ability to model Laplace operations with its Analog Behavior Modelling feature. Specifically, the Laplace voltage source ELAPLACE is ideal for this purpose. Therefore, the h/s terms in each controlled source can be directly modelled in PSpice without any additional simplifications or circuit modifications.

2.4 Development of Electrical Analogous Circuit for a Lossy Piezoelectric Transducer

Puttmer et al. furthered the transmission line model presented by Leach by incorporating mechanical losses into the transmission model [19]. Since Leach's model does not include mechanical or electrical losses in the piezo transducer, the transient responses of his simulated transducer were substantially different from the measured response [19] in order to model the behavior of piezo that is closer in agreement to a real piezo, mechanical losses in the ceramic must be accounted for.

To develop the model for the lossy transducer Puttmer presents the equations for the characteristic impedance Z_0 of a transmission line, and the wave propagation function γ:

$$Z_0 = \sqrt{\frac{R' + j\omega L'}{G' + j\omega C'}} \tag{2.27}$$

$$\gamma = \alpha + j\beta = \sqrt{(R' + j\omega L')(G' + j\omega C')} \tag{2.28}$$

where α is the attenuation constant of the transmission line and β is the phase constant, from which the phase velocity v_p can be derived.

In the low loss case both the dielectric and conductor losses are considered small, such that $R \ll \omega L'$ and $G \ll \omega C'$ [19], [24] . Therefore, the (2.27) and (2.28) can be simplified to:

$$Z_0 = \sqrt{\frac{L'}{C'}} \tag{2.29}$$

$$\alpha \approx \frac{R'}{2}\sqrt{\frac{C'}{L'}} \tag{2.30}$$

$$\beta \approx \omega\sqrt{L'C'} = \frac{\omega}{u} \tag{2.31}$$

Combining (2.30) and (2.31) gives the relationship:

$$\alpha \approx \frac{\omega}{2v_p}\frac{R'}{\omega L'} = \frac{\omega}{2v_p}\delta_m \tag{2.32}$$

From which an equation for R' can be defined as:

$$R' = \omega L' \delta_m \tag{2.33}$$

Where δ_m is the mechanical loss tangent, equivalent to $1/Q_m$, the mechanical quality factor of the transducer [13], [19], [25]. Q_m and δ_m are often cited by material manufacturers, thus the loss can be reasonably predicted from the specifications given in the datasheet. Q_m can also be measured from the resonance spectra of a piezo transducer according to the following relation with Z_m being the magnitude of the impedance at f_s [25].

$$Q_m = \frac{1}{2\pi f_s Z_m C_0}\left(\frac{f_p^2}{f_p^2 - F_s^2}\right) \tag{2.34}$$

The electrical losses, occurring in the piezo ceramic, called dielectric losses, can also be determined. If the dielectric is considered as having a complex permittivity with real and imaginary parts $\varepsilon_r + i\varepsilon_i$, the loss tangent of the dielectric can then be determined according the relationship given in [16]:

$$tan\,\delta_e = \frac{\left(\varepsilon_i + \frac{\sigma}{\omega}\right)}{\varepsilon_r} \tag{2.35}$$

where σ is the conductivity at DC of the dielectric. Puttmer et al. conclude [19], in most piezoelectric materials the loss in the dielectric is largely the result of a polarization lag, and this

is much greater than the contribution of the losses due to the DC conductance term σ. Therefore, δ_e can be approximated as $tan\,\delta_e = \varepsilon_i/\varepsilon_r$ [19]. Puttmer et. al assume that for in piezo ceramics the dielectric losses are negligible [19]. However, Sherrit and Mukherjee argue that many piezoelectric materials have been shown to demonstrate non-negligible dielectric losses, and their inclusion can therefore improve the accuracy of any model for the piezoelectric transducer [16].

In the lossy piezo transducer model, the lossless line in Fig. 2.2 is replaced with a lossy transmission line having per unit parameters R', L', C', and G' and length L. Puttmer et al. argue that the losses due to resistance and those due to conductance cannot be separated, and choose to make G' = 0 [19]. The length of the lossy line is determined by the ceramic thickness L_z.

2.5 Modelling Wave Propagation in Solids

To develop a model for the defect detection system, models for the non-piezoelectric elements of the system are required. Graff in [4] describes wave motion in elastic solids. Graff states that wave motion in an elastic solid can be modelled as an acoustic transmission line according to the following equations:

$$Z_0 = A_z Z_A = A_z \sqrt{\frac{E}{\rho}} \tag{2.36}$$

$$u = \sqrt{\frac{E}{\rho}} \tag{2.37}$$

where Z_A is the acoustic impedance of the medium, E is the Young's modulus, and ρ is the material density. Examining (2.22), (2.23) and (2.29) in relation to (2.36), and taking into account that for

isotropic media the elastic constant is the same as Young's modulus [16], we can establish a relationship for the per unit parameters of the solid as follows:

$$L' = \frac{1}{A_z \rho_m} \tag{2.38}$$

$$C' = \frac{1}{A_z E} \tag{2.39}$$

If the loss in the elastic solid is considered small, the non-piezo components of our model can be modelled as acoustic transmission lines having per unit parameters L' and C' according to (2.38) and (2.39), and propagate along the transmission line according to (2.28), (2.30) and (2.31).

2.6 Propagating Waves Incident on a Boundary

In this work we model the steel rod using an electrically analogous transmission line. To model the reflections off of defects in the physical rod, we also need a model for the defect in connection to the rod. We choose to model the defect as a transmission line, having impedance Z_{defect}, of length L_{defect}, and connected in series with the rod transmission line of impedance Z_{Rod}, and length L_{Rod}, as shown in Fig. 2.3.

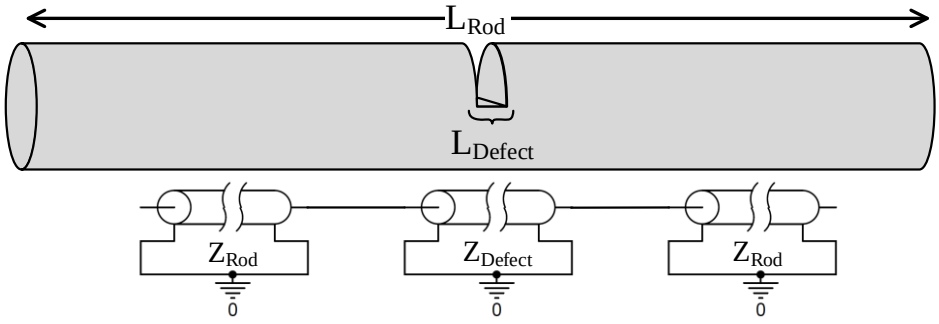

Figure 2.3: Typical rod with length L_{Rod} and defect length L_{Defect}. This situation can be modelled as three transmission lines in series as shown in the figure

The wavelength of the wave travelling in the rod can be found according to:

$$\lambda = \frac{v_p}{f} \tag{2.40}$$

With a $v_p = 5110$ m/s in steel, and given that the maximum frequency modelled in this work is 55 kHz, the wavelength of the signal will be $\lambda > 9.29\,cm$. Thus, for $L_{Defect} = 1\,cm$, the wavelength can be considered as $\lambda \gg L_{Defect}$. Therefore, from Pozar [24], a wave travelling down the transmission line of the rod, will partially reflect off of the boundary between the rod and the defect according to:

$$\Gamma = \frac{Z_{defect} - Z_{Rod}}{Z_{defect} + Z_{Rod}} \tag{2.41}$$

And since $\lambda \gg L_{Defect}$, we can neglect the resulting reflections between the defect and the rod at the second defect/rod boundary. Therefore, the part of the wave that is not reflected will continue to the end of the rod according to:

$$\mathrm{T} = 1 + \Gamma = \frac{2Z_{defect}}{Z_{defect} + Z_0} \tag{2.42}$$

3 Initial Model with Symmetric Acoustic Load

In this work the development of the PSpice model and the development of the sensors was an iterative process. In this chapter, the initial work on the PSpice model and the sensor is described. This was tested with a double transmission line. Our initial model of the system was based on the SPICE model presented by Leach [13]. The PSpice circuit used in the initial study closely resembled that presented by Leach in his work. Similarly, mechanical and electrical losses were not considered initially.

3.1 Initial Model

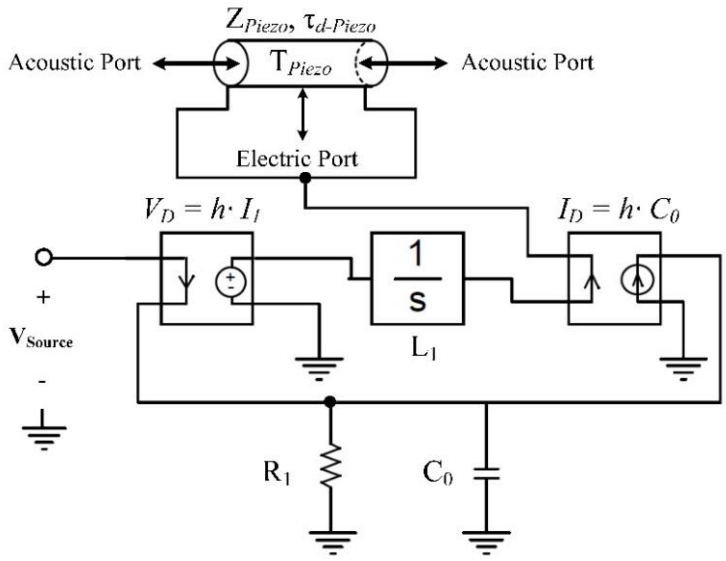

Figure 3.1: PSpice Schematic of the simplified piezo transducer circuit model

The model derived by Leach makes use of two dependent voltage sources, both proportional to h/s [13]. Leach makes a simplification to his model by using a Norton Equivalent Circuit. In the electrical analogous circuit portion of the model, the dependent voltage source in series with a capacitor is replaced by a current source in parallel with a capacitor [13]. The model presented

below is a PSpice realization of the equivalent circuit shown in Fig. 2.2, with a Norton Equivalent Circuit modification performed to the electrical analogous circuit part of the model. To find the equivalent circuit parameters of the materials modelled in the circuit, the following equations were used.

$$Z_0 = A_z\sqrt{E \cdot \rho} \tag{3.1}$$

$$\tau_d = \frac{L_z}{v_p} \tag{3.2}$$

$$v_p = \sqrt{\frac{E}{\rho}} \tag{3.3}$$

where A_z is the cross-sectional area of in the z-direction, E is Young's Modulus, ρ is the density, and v_p is the phase velocity of the wave in the material. In our experiments we selected carbon steel rods having density $\rho = 7870\ kg/m^3$ and a Young's Modulus of $E = 205\ GPa$ [26]. For the piezoelectric transducer, E, h, and ρ were found directly off of the datasheet for the piezo transducers used in the experiment [27]. The parameter h (N/C) was not listed in the datasheet, but the parameter d (C/N) was. Both constants are commonly referred to as the "piezoelectric constant" in literature [16], [17], and their units are inverses of each other. The parameter h was thus assumed to be the inverse of the value listed in the data sheet. While this was a substantial simplification, it would prove to be acceptable for the initial model. Similar to what Atlinger et. al did, the resistor R_1 was added to adjust the voltage level of the echo received by the transducer in order to achieve the results presented in Fig. 3.4 [19].

3.2 Symmetric Acoustic Load Test of PSpice Model

Following the development of the initial model it was desired to verify that the model was giving reasonably accurate results in comparison to real world behavior. To verify the model a unique test setup was developed that was simulated in PSpice and performed in the lab. A symmetric configuration was chosen that would be easily produced both in the lab and in simulation. Identical loads on either side of the piezoelectric transducer results in symmetrically launched waves in waveguides. The launched waves would rebound simultaneously off the end of each rod and then constructively interfere with each other at the transmitter. This eliminated the need to design a properly matched load on the non-driving end of the transducer.

3.2.1 Lab Setup for Symmetric Acoustic Load Test

Figure 3.2 shows the configuration used in the lab, where a thickness-mode piezoelectric transducer (SMD15T21R111WL) was placed between two 12.5 mm diameter rods, 1 m long rods.

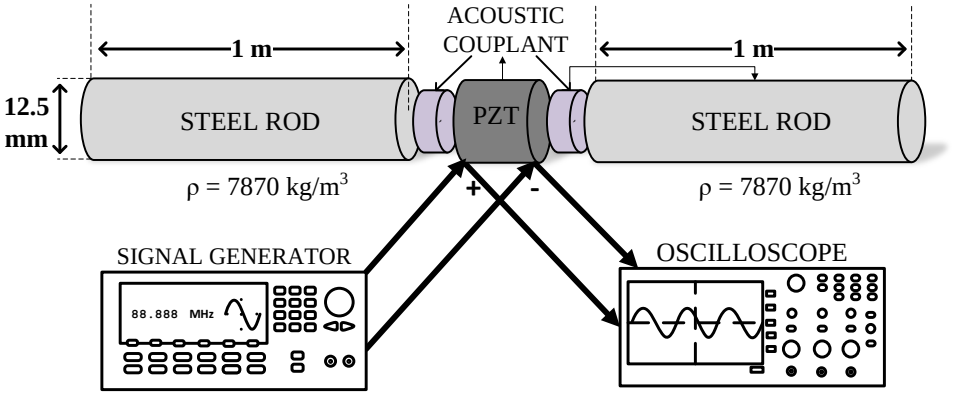

Figure 3.2: Lab test setup for verification of circuit model in PSPICE. Two rods of equal lengths are placed on either side of the PZT transducer, and transverse waves travel symmetrically in their respective wave guides.

The physical rods were chosen to be the same material, having equal densities, and have the same cross-sectional area as the PZT transmitters, $A_{Z_{piezo}} = 1.77 \times 10^{-4}\, m^2$. A signal generator was used to send a 5-cycle, 55 kHz, 10 Vpp, electric pulse to the PZT transmitter. The vibration of the transmitter is transferred into the rod via the acoustic couplant at each face of the transducer. The waves launched travel in opposite directions, rebound simultaneously off each rod end, and return to the transmitter where they constructively interfere. The differential voltage across the PZT is recorded using an oscilloscope.

3.2.2 PSpice Model of acoustic symmetric load test

In the PSpice model, two identical transmission lines, modeling the steel rods, are placed at the acoustic ports of the PZT transducer. The complete circuit for this experiment is shown in Fig. 3.3.

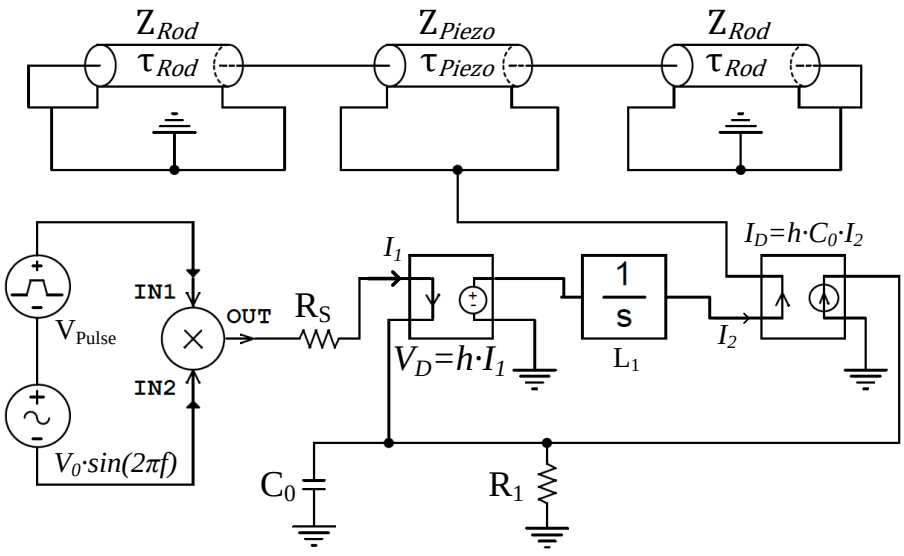

Figure 3.3: PSpice schematic of the model for the matched acoustic load test

The transmission lines representing the steel rods were assigned equal impedance and time delay (1) – (3). Acoustic loss in the rods was not considered. A short-circuit termination for each

transmission line was chosen to model the interface between steel and air. Steel has a much greater acoustic impedance than air, and therefore, the motion of steel vibrating in air can be approximated as an electrical short circuit [4], [21]. The acoustic couplant was modeled as an ideal acousto-mechanical connection between the PZT transducer and the steel rods. The signal source was configured as 10 V_{pp} and $f = 55$ kHz to match the laboratory test conditions. The results of the simulation were compared against the test results obtained in the lab.

3.2.3 Testing and Discussion of Results

The symmetric test was chosen because it was thought that such a configuration would produce the most well-known excitation of the system. The acoustic impedance seen by the piezoelectric would be the same on both faces, and therefore symmetric waves would propagate outwards on either side of the transducer. A comparison of the simulation and experimental results is shown in Fig. 8. The simulation result is in grey with the experimental results in black. The resistance R_1 was adjusted to match the peak-to-peak amplitude of the reflected signals of the experiment and simulation. If R_1 was left as an open circuit, modelling no electric loss, the waves peak-to-peak value was found to be 16 mV compared to the 23 mV peak-to-peak wave found experimentally. when R_1 was adjusted to 750 Ω in the simulation, an optimized value of 27 mV peak-to-peak was obtained. Thus, the ratio of applied to detected voltage in both the simulation and the experiment is found to be approximately 1000:1.

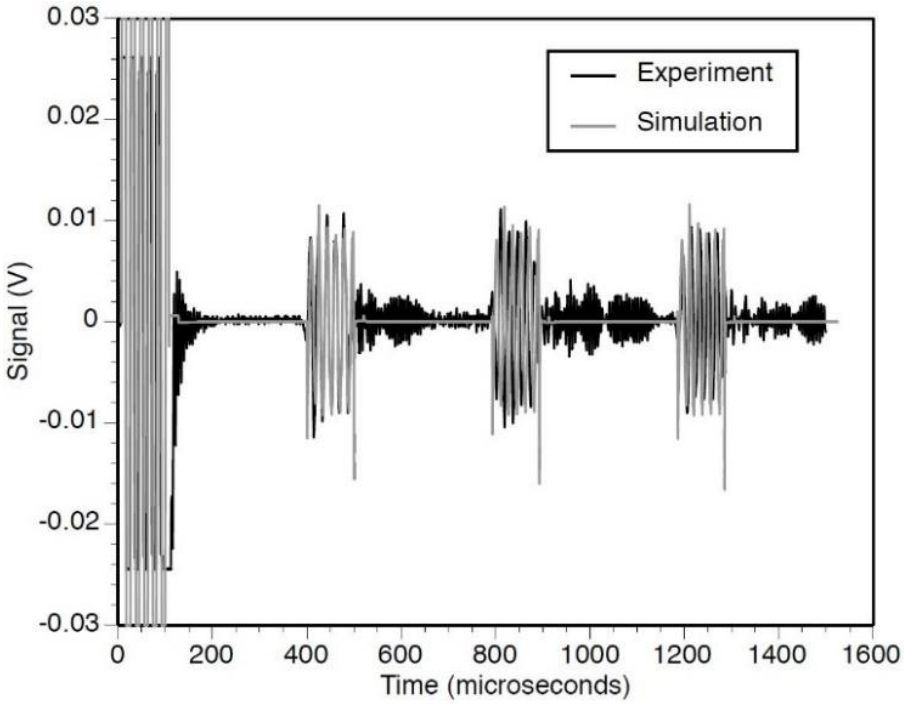

Figure 3.4: Comparison of simulation to experiment for a symmetrically driven pair of rods. Shown here are three consecutive wave pulse reflections off the end of each rod. See Fig. 3 for a description of the test setup.

In the experiment some of the energy coupled into the rod is converted into other modes of vibration such as flexural modes. These modes travel more slowly and can be seen arriving later in time than the longitudinal modes at approximately 500 μs. However, we chose not to model these additional modes in our simulation. We conclude that our model provides a close match with our experimental results.

3.3 Conclusions

An idealized, lossless model was developed as a basis for further development. To verify the model, an experiment involving a symmetrically-driven pair of steel rods was used to demonstrate that the model reproduces the major features of the signal generated in lab testing. However, many

simplifications were made. To produce a model that has more real-world significance, loss needs to be added to the model. Additionally, the piezoelectric parameters need to be more accurately determined. Datasheets are reliably unreliable, so an accurate determination of the piezo electromechanical constants is also necessary. Specifically, an accurate value for h needs to be determined since the simplification of $h = 1/d$ will not hold when adding more levels of complexity.

4 Development of Specialized Corrosion Detection Sensor

For the corrosion detection system outlined in this work, a piezoelectric-based transducer is required to transmit an acoustic pulse into the rod and detect the reflected acoustic waves. The PZT, thickness-extensional transducer used in our experiments is not suitable on its own for acoustic wave generation in grounding rods. This is largely due to the acoustic impedance mismatch between the piezo transducer (~6000 Ω) and the steel rod (~ 11000 Ω); this fact was also made evident over the course of many experiments in the lab. Therefore, different configurations involving a piezo transducer and a backing mass were experimented with. In this section a brief background is given to the development of the Constructed Resonant Actuating Sensor (CRAS) sensor developed by Zhao and Thomson [22], which was arrived at after several iterations of conception and implementation of different transducer configurations involving TE piezoelectric sensors.

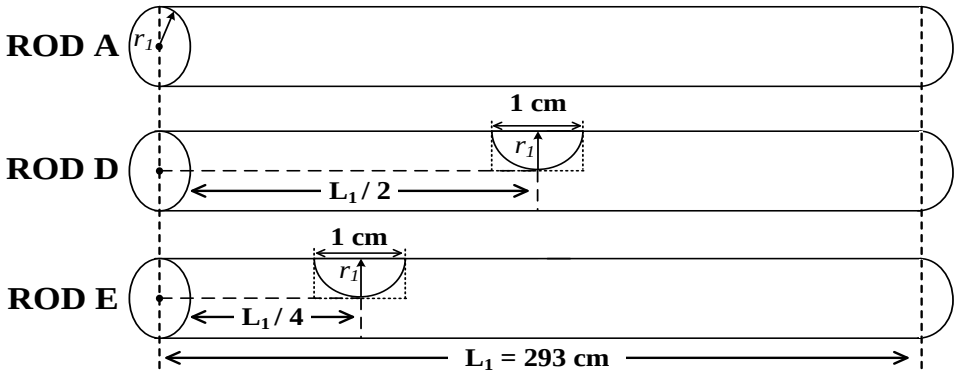

Figure 4.1 Diagram representing the three different rods used in experiments for this work

The sensors developed and presented in this chapter were tested on steel rods with physical properties closely matching the actual grounding rods. Three rods were used in the experiments

presented in this work, named Rod A, D and E. Rod A is a clean, defect-free rod, used as the control specimen. Rods D and E have had half of their cross-sectional areas removed at half length for Rod D and one quarter length for Rod E. In both rods the portion of the cross section removed is 1 cm for both rods. A diagram of these rods is presented in Fig. 4.1.

4.1 Clamped Sensor Configuration

The first successful configuration implemented and test was inspired by the work of Shoji et al. at NTT [5], [6]. Shoji and Hirata fixed shear-mode piezo transducers to customized clamps to generate an acoustic pulse in anchor rods. They found their clamped setup produced good detection of simulated defects which they produced in the lab. Similarly, Zhao and Thomson [26] developed a clamped setup using PZT Thickness-Extensional (TE) transducers. TE mode transducers were chosen in favour of shear mode transducers since they more reliably produced first order longitudinal mode acoustic waves in the rod. Furthermore, Zhao and Thomson found experimentally that shear-mode transducers produced a variety of undesirable wave modes in the rod that made corrosion detection substantially more difficult [26].

A picture of the clamped setup experimented with in the lab is shown in Fig. 4.2. Two sets of clamps were attached to the rod using two sets of screws to clamp either side around the rod. Two piezos were attached to each clamp pair, one on each half, as depicted in Fig. 4.2. The intent of piezo pairs was to generate a symmetric wave with respect to the rod circumference and the longitudinal axis. A small backing mass was attached to the non driving-side of each piezo.

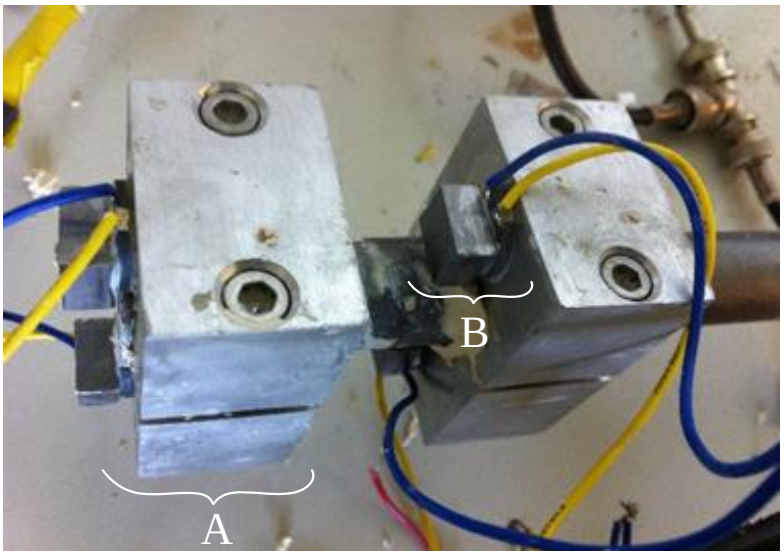

Figure 4.2: Lab setup of clamped piezo configuration. Depicted are the two sets of clamps (A), having one pair of driving piezos and one pair of receiving piezos. A small backing mass (B) is applied to the non-driving side of the piezos to provide motional inertia for better vibration generation into the rods

The backing mass provided motional inertia to the piezo, such that the backing mass provides momentum to produce a larger vibration into the clamp and ultimately into the rod to which the clamp is fixed. There were three main disadvantages to using this configuration.

i. Securing the clamps to the rods required a substantial amount of time. This difficulty was exacerbated by field testing when the rods were buried in the ground, and attaching the clamps with the rods were positioned vertically proved to be more difficult.

ii. Achieving successful acoustic coupling between the clamps and the rod is also challenging. Careful application of acoustic couplant was required, and even then achieving repeatable and consistent coupling was nearly impossible. Also the surafce of the rods in the field was uneven and made the coupling uncertain.

iii. The clamps had the effect of adding an extra vibrating mass, such that when the pulse was applied to the piezos, the clamps continued to vibrate for several hundred microseconds after the pulse burst has completed. This excessive vibration could not be tolerated since it would have a cloaking effect over any potential defects present in the rod. Thus to stop the vibration at the end of the pulse wet clay was used to dampen the ringing. The clay attenuated the excessive vibrations but not perfectly, and in field testing this ringing proved even more challenging.

4.1.1 Discussion and Results of Testing with Clamped Configuration

The results of testing the clamped configuration are presented. Testing was performed on two bare rods, one having no defects, named Rod A, and the other having a simulated 50% cross-sectional loss at the half way point of the rod, named Rod D. The test was performed at 55 kHz, with an applied voltage of 5 Vpp. Clay was applied around the clamps to reduce the excessive vibration in the clamps. The launching piezos are separate from the receiving piezos so that saturation in the amplifier is avoided. The received signal is passed to an operational amplifier with a gain factor of 120 and a having a 60 Hz filter. The results of this test are shown in Fig. 4.3 for the two rods.

The test reveals that the signal level received by the echo-pulse is sizeable with respect to the input signal. The input signal is 5 Vpp, and the echo signal received is close to 10 Vpp after being amplified. Thus the ratio of the signal transmitted to signal received is approximately 60:1. However, the excessive vibration is still apparent as the detected stimulus pulse does not die-out until after 250 μs. When compared with the 91 μs of the burst applied, we see that it continues to ring more than 2.5 times as long.

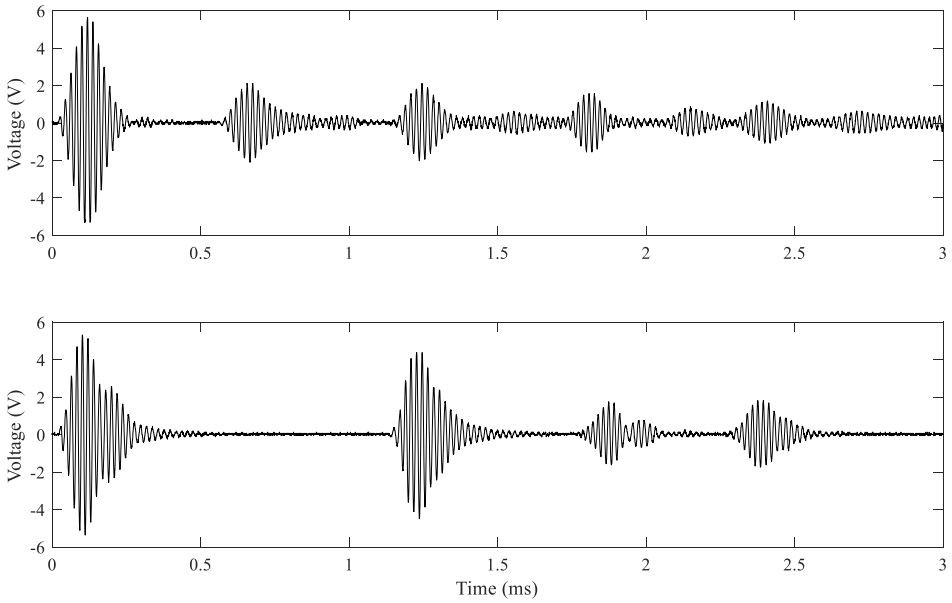

Figure 4.3: Results of testing on Rod D (top), and Rod A (bottom) for Clamped Configuration. Testing performed at 55 kHz and 5 Vpp applied to test sensor.

The implications of this excessive ringing is that if any defects are present at the beginning of the rod, they will not be detected due to the excessive ring-time of the applied stimulus. Also, modes are present in the signal other than the intended L(0,1) mode. These can be observed in the Rod A response of Fig 4.3 at 2 ms, where an echo is recorded that is neither the end of the rod, nor a defect. This other mode travels slower than the longitudinal mode and thus is observed arriving after the L(0,1) echo from the end of the rod. The introduction of non L(0,1) modes is undesirable since they distort the signal and can be mistakenly interpreted as defects which are not actually present.

4.2 Mass Backed Piezos

The second piezo configuration implemented and tested was a significant departure from the first. As a result of the initial modelling that was performed, we began to think of the rod and transducer elements of the test setup as transmission lines. As a result, we were able to make guided decisions

to match their impedances in such a way that maximized signal transmission and minimized ringing [4]. We did away with the clamps which indirectly transmitted the longitudinal wave into the rod, and chose instead to apply the piezo directly to the end of the rod as shown in Fig. 4.4.

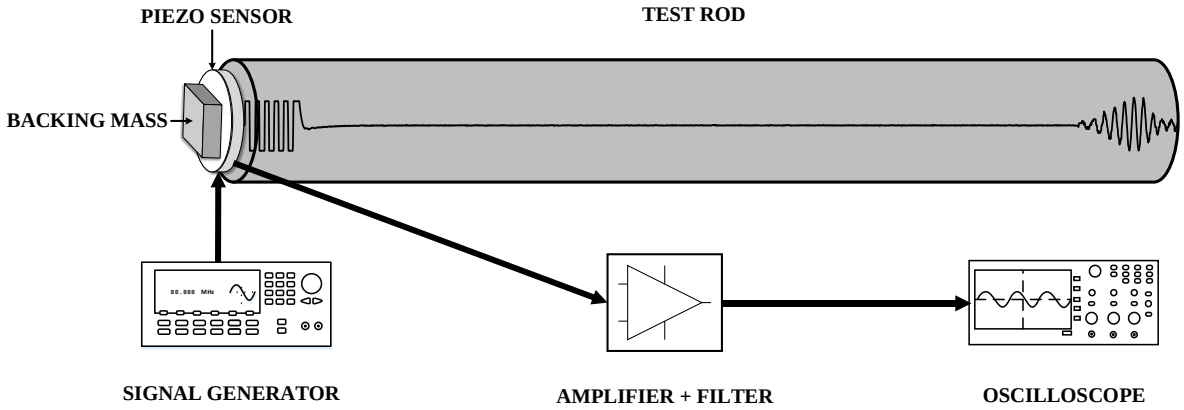

Figure 4.4 Diagram showing how the mass backed piezo transducer is fixed to the test rod, and the lab test setup

The first iteration of the new test configuration was adding to the non-driving side of the piezo a mass from a build-up of silver epoxy. The epoxy provided some momentum to the back of the piezo as it pulsed and generated the longitudinal wave into the rod. The intent of the piezo and mass at the end of the rod was to stimulate the longitudinal wave in the rod without inadvertently introducing other wave modes. The decision to move from the clamped piezo configuration to the piezo at the rod end was inspired in part by the PSpice model presented in the previous chapter. As discussed in Chapter 2, the PSpice model had the piezo in series with the rod, modelling the physical piezo at the rod end. The modelling revealed that adding a mass to the non-driving side of the piezo resulted in larger vibrations in the rod. Thus, it was decided to implement the configuration modelled in PSpice in the lab as well. One iteration of the mass backed piezo is shown in the Fig. 4.5.

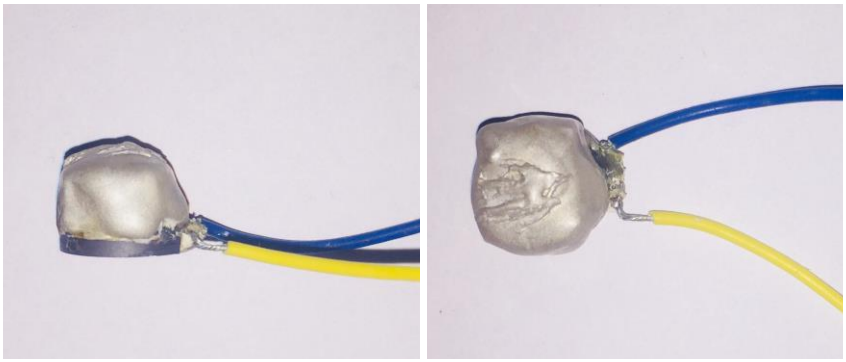

Figure 4.5: Picture of mass-backed piezo used in the experiment from section 4.2

The advantage of this configuration over the clamped configuration is that the process of fixing the transducer to the end of the rod was quick and straightforward. The disadvantage of this configuration is that the process of making the sensor is largely trial and error. It is difficult to predict the behavior of the transducer before performing the test.

4.2.1 Discussion and Results of Testing with Mass-Backed Configuration

The results of testing the mass-backed configuration are presented. The test was performed on the same two bare rods, Rod A and Rod D. The test was performed over a range of frequencies and the results were analyzed to find the best time domain response of the mass-backed transducer. It was found the 75 kHz, with an applied voltage of 500 mVpp produced the best results for this configuration. Like the clamped configuration test, the received signal is passed to an operational amplifier with a 120x gain and 60 Hz filter. The results of this test are shown in Fig. 4.6 for the two rods.

The results show that the signal level is much lower for the mass-backed piezo than the clamped configuration. The input signal is 500 mVpp, and the echo signal received is nearly 400 mVpp after being amplified by an op-amp with a gain of 120. Thus, the ratio of the signal transmitted to

signal received is approximately 75:1. The signal levels shown in Fig. 4.6 are after gain is applied with the operational amplifier.

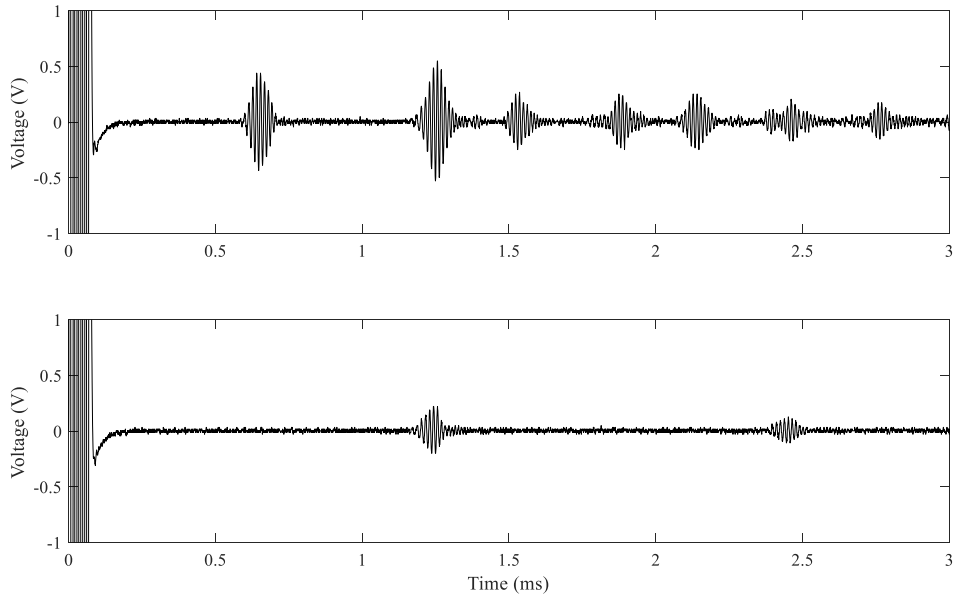

Figure 4.6: Results of testing on Rod D (top), and Rod A (bottom) for mass-backed configuration. Testing performed at 75 kHz and 500 mVpp applied to piezo

Since the signal level is lower than the clamped configuration, it is not suitable for our application. The attenuation factor of the buried rod is very high. Thus, a small signal level of the sensor is not acceptable, since the wave will definitely attenuate greatly before it is detected by the data acquisition system. Furthermore, since the signal level is low, the signal to noise ratio will also be much worse.

4.3 Development of the CRAS Sensor

The CRAS sensor was developed by Zhao and Thomson [22] to overcome the disadvantages of the previous piezo configurations developed and test in the lab experiments. The CRAS sensor was designed to be a resonator, such that its physical design would give rise to a predictable

function response. Zhao and Thomson developed a constructed piezo symmetrical resonator, which they designed to have a resonant frequency near 75 kHz. A diagram of the developed sensor is shown in the Fig. 4.7 [22].

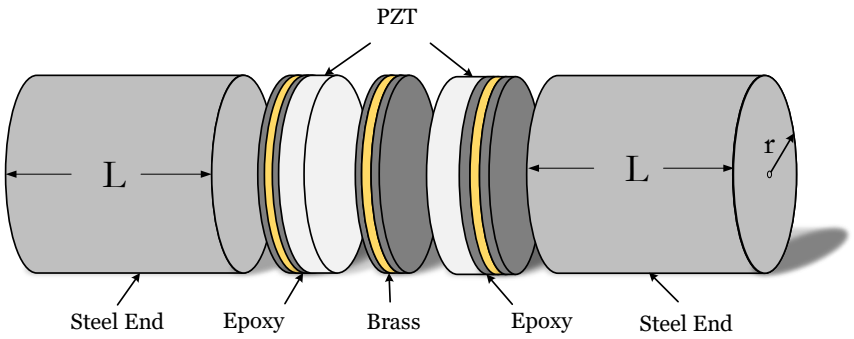

Figure 4.7: Diagram of the all Ag-Epoxy constructed piezo transducer variant developed by Zhao and Thomson. The resonator is composed of four different components, silver epoxy, brass electrodes, PZT sensors, and steel end pieces

The resonator is composed of four different components and is symmetrical by design. Two piezos are fixed between two steel cylinders, and three brass electrodes are interspaced between them. The two piezos form the transmitter and receiver of the device, respectively. The brass electrode on the left and right side of Fig. 4.7 represent the positive electrodes for the sending and receiving piezos, respectively. The middle brass electrode is the common ground electrode shared by the two transducers. By varying the length of the steel cylinders the resonant frequency of the transducer shifts proportionally. The brass, piezos and steel pieces are fixed together in place with epoxy. Two different variations of this constructed resonator were developed in the lab. In the first variation the epoxy attaching the brass electrodes to the steel pieces was a polymeric epoxy. In the second variation all the epoxy layers are made of silver conducting epoxy. In Fig. 4.8 the actual CRAS sensor is shown.

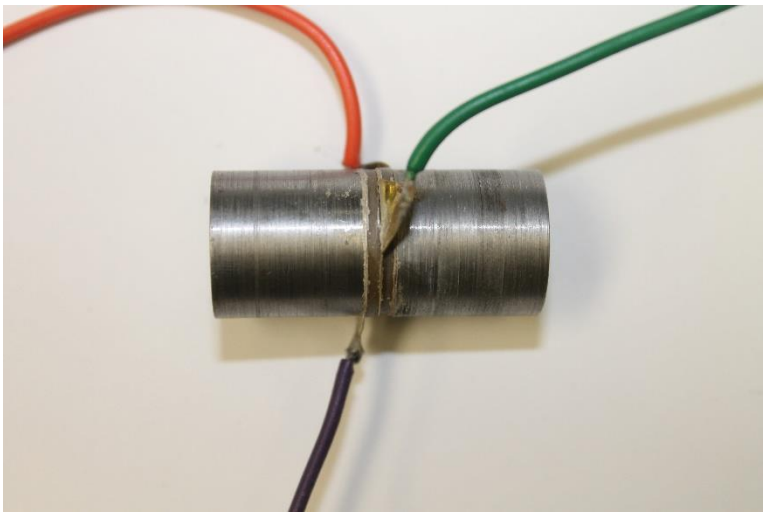

Figure 4.8 Picture of the actual CRAS transducer used in the experiments

The resonance behavior of each CRAS variation was plotted using an impedance analyzer, as shown in Fig. 4.9. The impedance analyzer measurement was to demonstrate that the resonator does indeed demonstrate strong resonance attributes, and to compare the measured resonant frequency value with the predicted value.

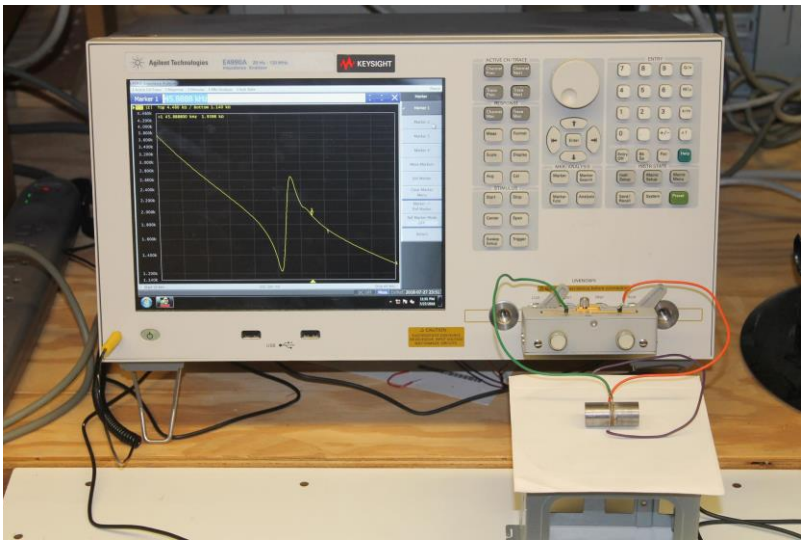

Figure 4.9 Picture of lab setup for analyzing the impedance behaviour of the transducers in this work using the Agilent E4990A Impedance Analyzer

The results of the impedance measurement for the two variations are presented in the Fig. 4.9. From the resonance curves, the two variations demonstrate different resonant behaviors. Specifically, the first variation has a series resonant frequency at 52.3 kHz and $|Z_s| = 540\ \Omega$, and parallel resonance at 54.5 kHz and $|Z_p| = 4220\ \Omega$. The second variation has a resonant peak at 40.1 kHz and $|Z_s| = 916\ \Omega$, and parallel resonance at 41.1 kHz and $|Z_p| = 3652\ \Omega$.

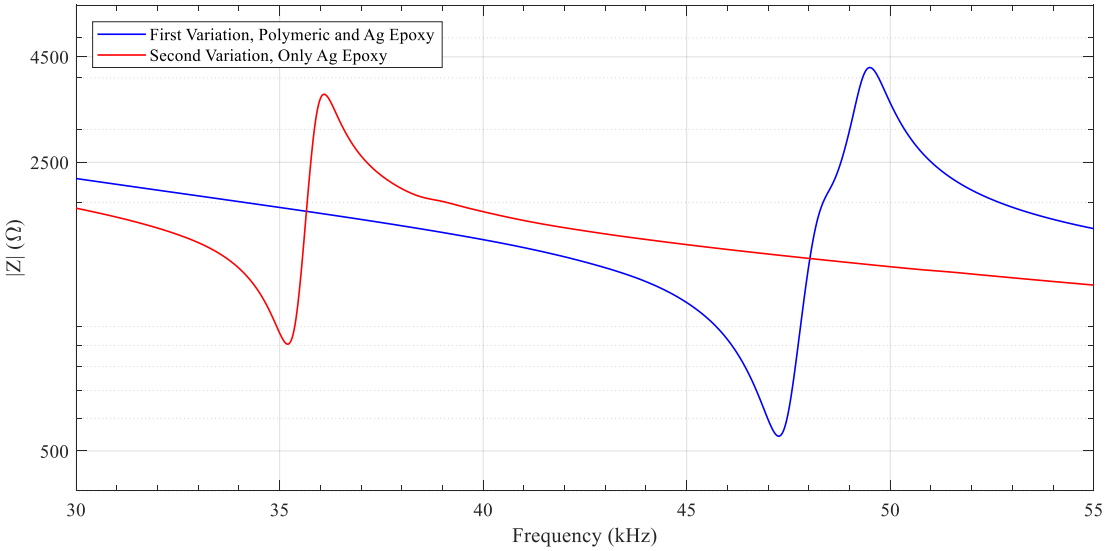

Figure 4.10: Impedance vs. Frequency curves for the two CRAS variations developed by Zhao and Thomson. The first variation uses a combination of polymeric epoxy and silver epoxy to hold the pieces together, and the second variation uses only silver epoxy.

The shapes of the two resonant curves are also different. While the curve between the series and parallel resonances of the second variation is a straight line, the curve connecting the series and parallel resonances of the first variation is not. The reason for this is not certain, however it is likely the result of the non-ideal nature of the piezo transducers themselves.

4.3.1 Time Domain Response of CRAS sensor

A time domain test of the first piezo variation is presented. Both CRAS variations produce very similar time domain behaviour when fixed to a grounding rod. Thus, only the results of the second variation is presented. The test was performed with a 5 cycle 40 kHz sine burst, at 500 mVpp. A diagram of the CRAS transducer attached to the rod is shown in Fig. 4.11.

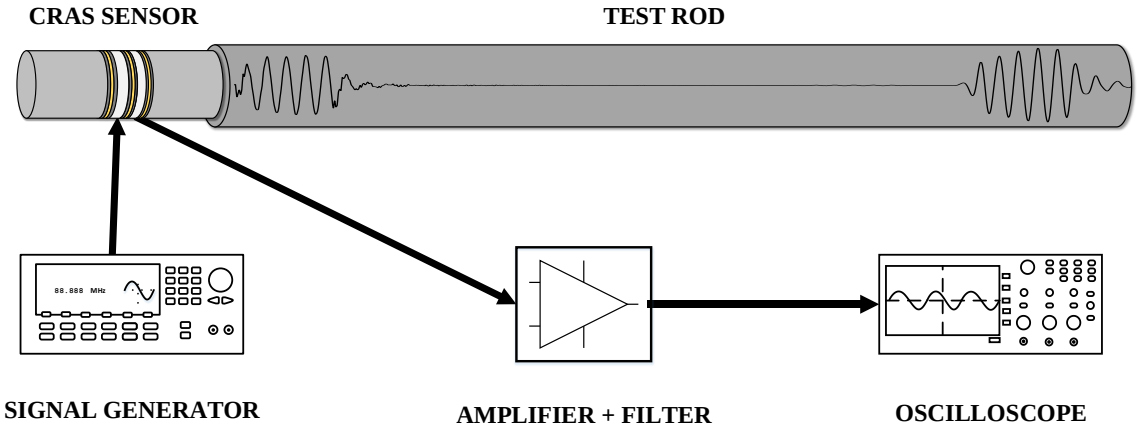

Figure 4.11: Diagram showing the pulse-echo experiment for CRAS sensor connected to the test rod

The intent of driving at resonance is that the resonator will naturally vibrate at its resonant frequency, so the transmitted and recorded echo pulses will have ideal signal level at resonance. The results of the test are shown in Fig. 4.12.

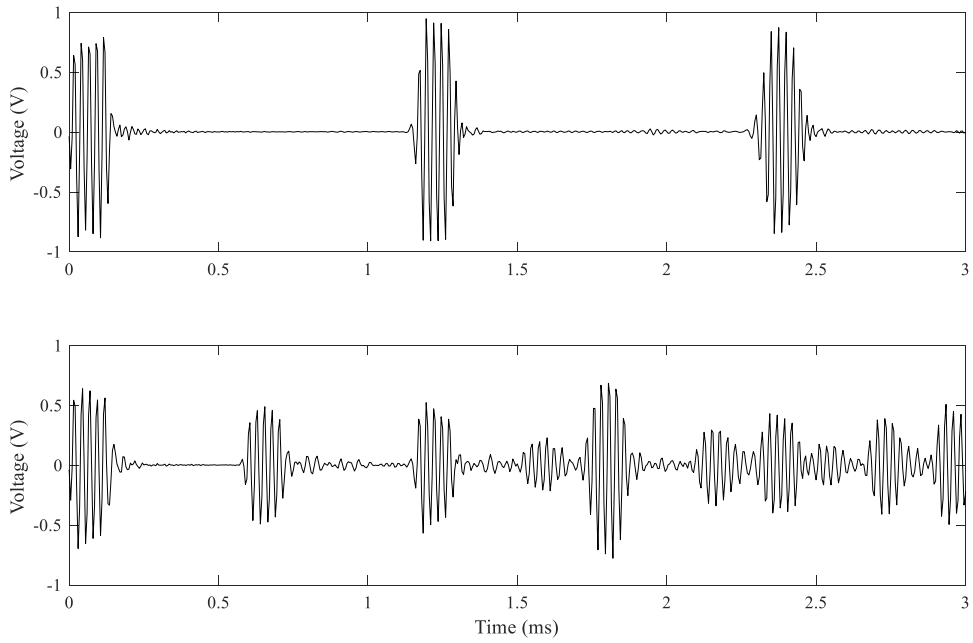

Figure 4.12: Results of testing on Rod A (top), and Rod D (bottom) for CRAS Configuration. Testing performed at resonant frequency of sensor, 40 kHz, with 500 mVpp applied to transmitting piezo.

The results show that the CRAS sensor configuration produces echo pulses superior to the previous two configurations. There is also very little mode conversion with the maximum being less than 1% of the peak-to-peak reflected signal. The signal level applied is 500 mVpp, and the recorded signal is close to 1.5 V for the wave generated into rod D. While this signal is largely dependent on how well the transducer is fixed to rod end, the ratio of signal transmitted to signal received is still 40:1 in the worst case. Furthermore, there is no apparent excessive ringing observed by the receiving piezo. Thus, this transducer configuration is ideal for corrosion detection testing in the field. It offers the best signal transmitted to signal received of the 3 configurations presented.

4.4 Conclusions

Three different configurations were tested in the process of developing a transducer suitable for defect detection in a steel bar. The clamped configuration, a mass-backed piezo and the CRAS

configuration all demonstrated effective defect detection within a steel bar. However, the configuration with the largest output-to-input signal ratio was by far the CRAS. The CRAS most effectively generated the first order longitudinal wave mode in the rod without adding other undesirable modes as was observed in the mass-backed and clamped configurations. The CRAS is chosen as the best suited transducer configuration for defect detection in steel bars. In the next chapter a model of the PZT transducer is developed that can be combined with other elements to produce a model of the CRAS sensor presented in this chapter.

5 Lossy Piezo Transducer Modelling in PSpice

In this chapter the model presented in Chapter 3 is further developed. As described in Chapter 3, many simplifications to piezo model were made in the first iteration; the most significant simplifications being that mechanical losses in the piezo were neglected, and the piezo transducer model parameters were assumed to be the same as those reported in the datasheet for the piezo. After departing from the idealized, matched transmission line model, it soon became apparent early on that these simplifications would not produce a meaningful model for defect detection in grounding rods. Mechanical losses in most piezo transducers are not negligible [19] and any model which does not include them will not be useful for modelling real-world applications. To produce a useful model of the piezo transducer able to simulate experiments performed in the lab, the model required a fundamental redesigned. In this chapter we present a model for the piezo transducer based on the equations developed for a lossy piezo transducer presented in Chapter 2. The PSpice implementation we present in this chapter directly follows the equations developed by Leach (Fig 2.1), where a second integrating dependent voltage source is used in place of the Norton equivalent circuit simplification presented in his PSpice implementation. Following in the steps of Atlinger et. al [19], we modify our model to incorporate mechanical loss, while losses in the dielectric are not considered. To obtain a more accurate model of the piezo transducer, we follow in the steps of Dahiya et. al [18] and use PRAP software [23] to determine the piezoelectric parameters for the transducer used in our experiments based on its resonant behaviour. The piezo model is then combined with other elements to produce a model of the Constructed Resonant Actuating Sensor (CRAS) developed by Zhao and Thomson [22].

5.1 Determination of Piezoelectric Electromechanical Constants

Piezoelectric Resonance Analysis Program (PRAP) is a software produced by TASI Technical Software Inc. [23]. It uses a curve-fitting algorithm to determine the electromechanical constants of a piezo transducer based on its behavior near resonance. The user specifies the density, thickness, and piezo transducer type (sheer, thickness extensional, bimorph, etc.) and uploads their measured data into the software. PRAP applies its analysis algorithm to the resonant peak of their choosing. The algorithm then applies its fitting algorithm to the resonant data, and yields the piezoelectric constants that result from the fitted curve. Among others, PRAP gives values for the parameters h, C_{33}^{D}, and ε_{33}^{S}. In turn, from equations (2.22)-(2.26) these constants are used to derive the static and per unit capacitance of the piezo PSpice model. The per unit inductance is not affected by the PRAP fit since it is dependent on ρ_{piezo}, which is found from the datasheet. In its output PRAP displays a graph of the user-uploaded data and a fit to four different model types commonly used by researchers. The first, named "Fit", is a fit to the impedance equations presented in 2, (2.3), (2.7) – (2.11) . The other three fits are for different circuit models of the piezoelectric transducer that are not discussed here. The PRAP outputs for the fitting algorithm applied to measured data of the piezo transducer is presented in Fig. 5.1 and 5.2. An ideal piezoelectric resonator would have one peak at its parallel resonant frequency, and a single series resonant frequency where its impedance is minimal and entirely real. As seen in Fig. 5.1 and 5.2, the measured resonant behavior is non-ideal. Several parallel resonance peaks are observable in a small bandwidth. This non-ideal behavior makes it impossible to determine a perfect first order model for the transducer. However, PRAP gives the ability to select one resonant peak of interest and provides a unique fit to that selected peak. In this work two resonant significant peaks were

chosen for analysis. The first fit was to the dominant parallel resonant peak and the results are shown in Fig. 5.1. The second fit presented in Fig. 5.2 was selected so that the overall or average of the resonance behavior was represented by the fit.

5.1.1 First Fit Applied to Piezo Resonant Curve using PRAP

Figure 5.1 shows the first fit applied in PRAP to the resonance data measured for the 1.2 mm piezo transducer.

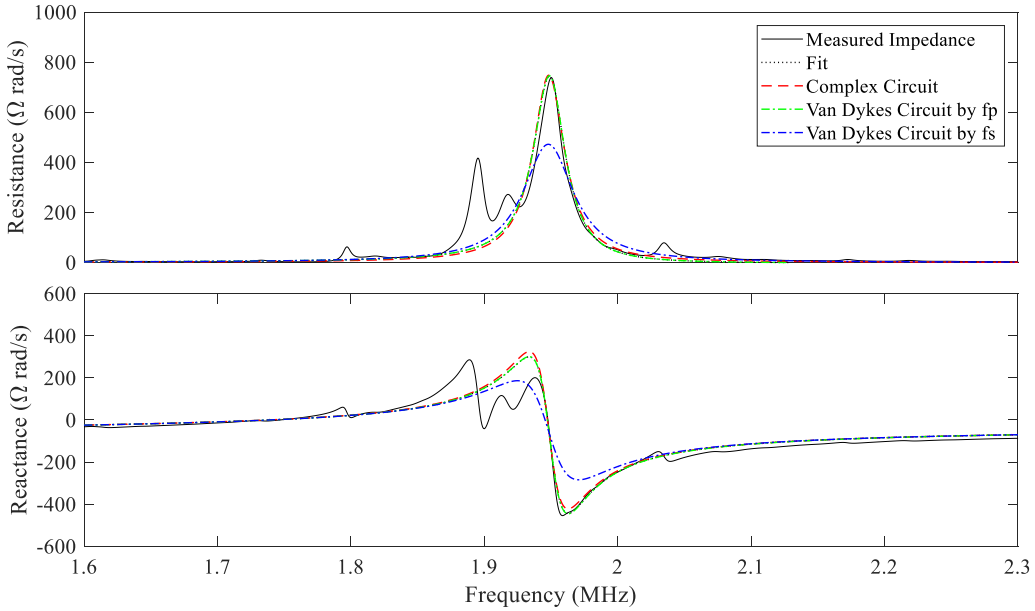

Figure 5.1: The first fit performed in PRAP. Fitting is applied to the tall parallel resonance peak of the impedance curve for the 1.21 mm transducer near its rated resonant frequency.

The first fit largely ignores the two peaks to left of the dominant resonant peak at 1.95 MHz in the resistance vs. frequency plot. The line marked "Fit" is perfectly coinciding with the red line marked "Complex". From the reactance plot, we observe that the "Fit" curve ignores the multiple resonances occurring at 1.9 MHz. The parameters yielded from the first fit give h_{33} = 2.06 GN/C, c_{33}^{D} = 170 GPa, and ε_{33}^{S} = 9.75 nF/m. PRAP provides complex values for the piezoelectric

parameters, but only the real parts of these constants are used in the models hereon presented. The significance of complex piezoelectric parameters vs real-valued parameters is not discussed in this work.

The values relevant to the piezo model obtained from the first PRAP fit along with their derived parameter values found using (2.23) and (2.26) are presented in Table 5.1.

Table 5.1: Fitted parameters obtained from PRAP fit to tall resonance peak and the associated derived parameters

Fitted Parameter	Fitted Value From PRAP	Derived Parameter	Derived Parameter Value
c_{33}^{D}	$1.7117 \times 10^{11} + \mathrm{i}2.5614 \times 10^{9}$	C'	$33.006\ \mathrm{nF/m}$
ε_{33}^{S}	$9.7496 \times 10^{-9} + \mathrm{i}8.9431 \times 10^{-12}$	C_0	$1.426\ \mathrm{nF}$
h_{33}	$2.0557 \times 10^{9} + \mathrm{i}7.5295 \times 10^{6}$	$-$	$-$

5.1.2 Second Fit Applied to Piezo Resonant Curve using PRAP

The second fit applied to the resonance data is presented in Fig. 5.2. The line marked "Fit" directly coincides with the red line marked "Complex". Unlike the first fit, the "Fit" curve ignores the dominant resonant peak observed at 1.95 MHz. Instead the overall resonance behavior is more closely fitted. From the resistance data the "Fit" line takes into consideration the first two resonance peaks observed near 1.9 MHz. Similarly, in the reactance data the resonances occurring at 1.9 MHz are taken into account for the applied fit. The parameters yielded from the second fit give a $h_{33} = 2.44$ GN/C, $c_{33}^{D} = 172\ GPa$, and $\varepsilon_{33}^{S} = 7.05\ nF/m$.

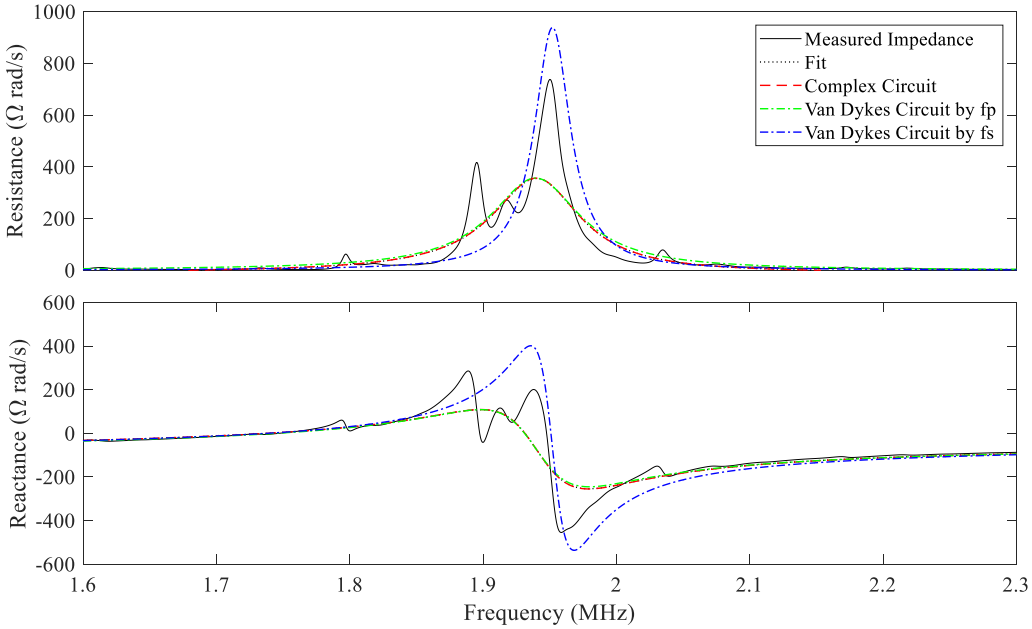

Figure 5.2: The second fit performed in PRAP. Fitting is applied to the wide parallel resonance of the impedance curve for the 1.21 mm transducer near its rated resonance

The values relevant to the piezo model and the derived values obtained from them using (x) and (y) are presented in Table 5.2.

Table 5.2: Fitted parameters obtained from PRAP fit to wide resonance peak and the associated derived parameters

Fitted Parameter	Fitted Value From PRAP	Derived Parameter	Derived Parameter Value
c_{33}^{D}	$1.7184 \times 10^{11} + \mathrm{i}2.8737 \times 10^{9}$	C'	32.879 nF/m
ε_{33}^{S}	$7.0445 \times 10^{-9} + \mathrm{i}7.3505 \times 10^{-12}$	C_0	1.030 nF
h_{33}	$2.4422 \times 10^{9} + \mathrm{i}1.0039 \times 10^{7}$	–	–

5.1.3 Comparison of Results

Comparing the two fits obtained from PRAP, it becomes clear that depending on what peak is selected, C_0 and h vary significantly, but the C' remains constant regardless of which peak is selected. A larger h results in a larger output voltage for a given vibrational stimulus than a piezo having a smaller h, and vice versa. A larger C_0 will cause the piezo to have a smaller impedance

at DC, and vice versa. Thus, changing C_0 has the affect of shifting the piezo's resonant curve up or down over its entire bandwidth. In the next section the revised model for the piezo transducer is presented and a comparison between the results of each PRAP fit are compared.

5.2 Modelling Standalone Piezo Transducer

While Leach chooses a Norton equivalent circuit simplification in the electrical analogous circuit [13], this simplification was rejected in the model presented in this chapter. The reason for this is that in Leach's work he models a standalone piezo transducer and is not in connection to other solid elements such as a steel bar, as in this work. In developing a model for the constructed sensor, it was discovered that Leach's Norton Equivalent Circuit simplification was giving results that were not in agreement with results obtained in the lab. Furthermore, using a dependent current source in PSpice makes the circuit cumbersome to manage, as a wire needs to be placed between the two sources. Hence, for simplicity, a Laplace voltage source in series with a capacitor was chosen in place of the Norton equivalent current source presented by Leach. Using the dependent voltage simplifies the troubleshooting of the model and is also conceptually easier to follow as it directly results from the equations presented in Chapter 2 as shown in Fig. 2.1.

5.2.1 PSpice Implementation of Standalone Piezo Transducer Model

The revised model of the standalone piezo transducer is presented in Fig. 5.3. The resistors R_B and R_F model the air impedance at the front and back face of the piezo transducer, respectively as seen in [19]. The Laplace voltage sources E1 and E3 implement the behavior described by (2.18), (2.19). The voltage sources V2 and V3 are 0 V sources which provide a reference current for the two

Laplace sources; using reference sources is a requirement of the PSpice software. C_0 indicates the static capacitance of the piezo transducer, and the per unit parameters L', C', and R' are contained within the transmission line labelled "Piezo" in Fig. 5.3. C_0, C', and L' prime were found according to (2.22), (2.23) and (2.26) using the piezoelectric parameters found from the PRAP fitting performed in Section 5.1.

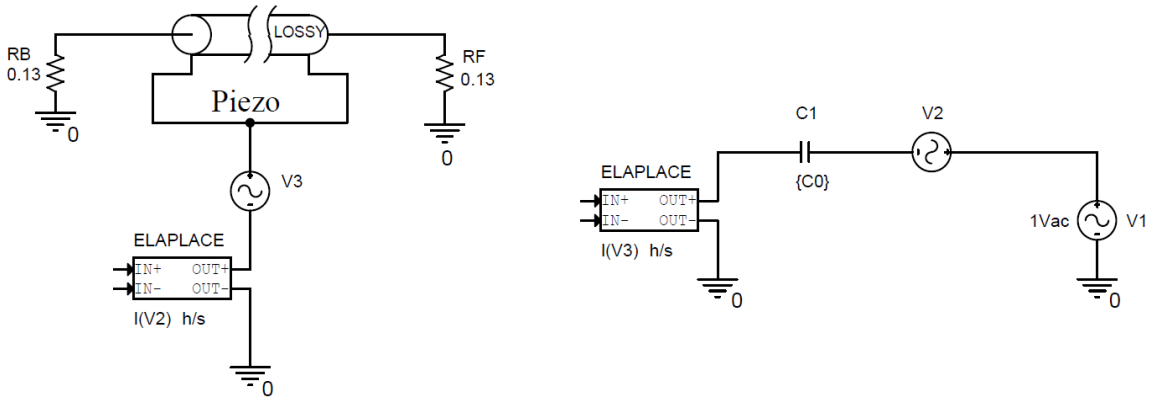

Figure 5.3: The model for the standalone piezoelectric transducer implemented in PSpice.

5.2.2 Testing and Results of Standalone Piezo Model

A linear frequency sweep over a 900 kHz bandwidth between 1.3 MHz to 2.2 MHz was performed on the PSpice model presented in Section 5.2.1. The sweep was done twice, once for each set of parameters obtained from the first and second PRAP fits performed in Section 5.1. The impedance vs. frequency curves for the two simulated frequency sweeps are shown in Fig. 5.4 along with the measured data.

The results from Fig. 5.4 show that the results of the PSpice simulation using parameters obtained from PRAP are in good agreement with the measured data of the piezo. The line marked "Fit for

Wide Peak" is in best agreement with the measured data. In the next section the standalone piezo model is extended to model the CRAS sensor developed by Zhao and Thomson [22].

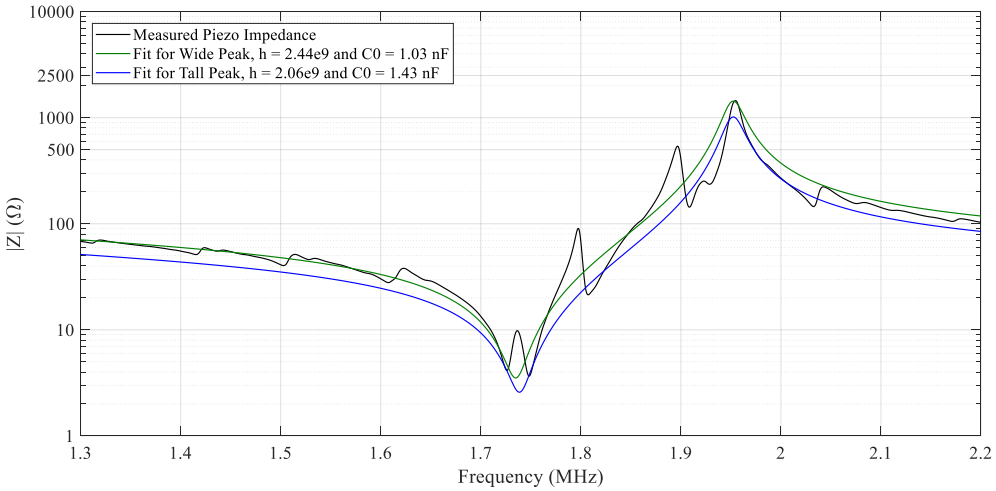

Figure 5.4: |Z| vs frequency A comparison of the results obtained for the different modelling parameters obtained from PRAP software.

5.3 PSpice Modelling of First CRAS Variant

The standalone piezo model is extended to model the CRAS sensor presented in Chapter 4. The standalone PZT model is used as a base, and the different elements comprising the CRAS sensor are individually modelled and combined to form a complete model of the transducer. The physical materials comprising the CRAS sensor are modelled as transmission lines, with per unit parameters related to their unique physical properties as described in Chapter 2. The PSpice model is verified using a similar frequency analysis to the one described in Section 5.2. Further verification is done for the CRAS sensor using a transient analysis in the time domain.

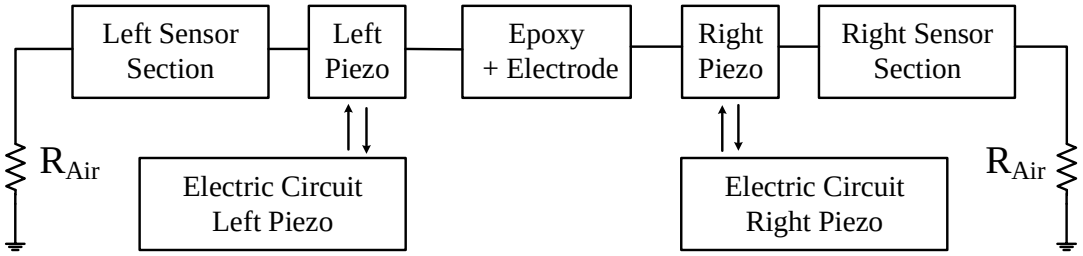

Figure 5.5: Block diagram of PSpice model for the CRAS sensor, from Chapter 4. The two CRAS variations have identical topologies but differ in the elements that make up the Left and Right Sensor Sections.

A model for each CRAS variation is developed and presented. The PSpice implementation of the two variations are nearly identical and have the same general topology. A block diagram showing how both CRAS sensors are modelled in PSpice is presented in Fig. 5.5.

5.3.1 PSpice Schematic for First CRAS variant

The PSpice model is composed of 7 sections in total. The circuit is divided into two main parts, the mechanic analog circuit, and the electrical analog circuit. The mechanical analog circuit is composed of the Left and Right Sensor Sections, the piezo mechanical analog circuit, and the middle section containing the epoxy and ground electrode. Starting from the left, the Left Sensor Section is that part of the schematic modelling the steel end piece, the resin epoxy, left brass electrode, and silver epoxy. The PSpice implementation of this section is shown in Fig. 5.6.

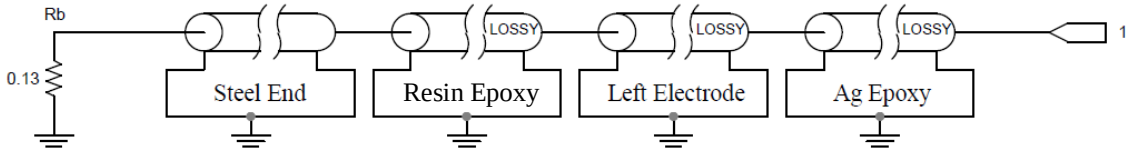

Figure 5.6 PSpice implementation of the Left Sensor Section from Fig. 5.5

The next section is that part of the model containing the mechanical portions of the two piezo models, their shared ground electrode and the three epoxy layers joining them. The PSpice implementation of the middle section is shown in Fig. 5.7.

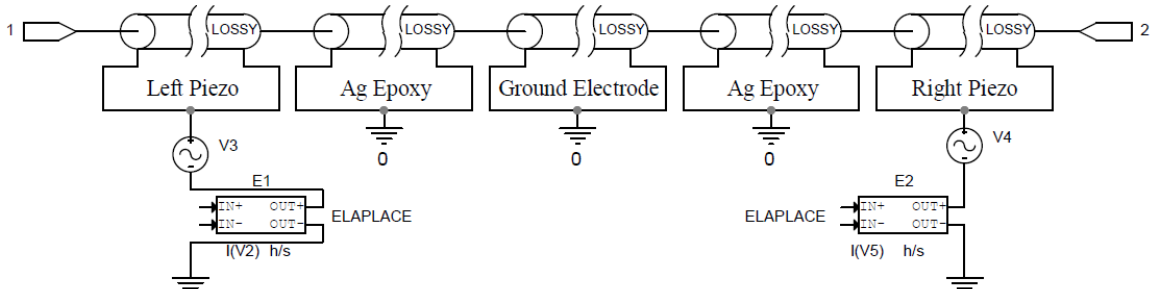

Figure 5.7 PSpice implementation of the Left Piezo, Epoxy + Electrode, and Right Piezo Sections from Fig. 5.5.

The right most section is a mirror image of the leftmost section, containing the second rod end piece, the right electrode and the epoxy layers joining them. The PSpice implementation of this section is shown in Fig. 5.8.

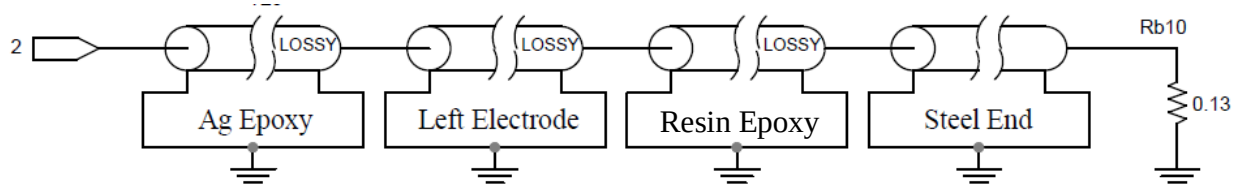

Figure 5.8 PSpice implementation of the Left Sensor Section from Fig. 5.5

The electrical analog portion of the PSpice schematic is that part which models the electrical circuits of the piezo transducers. A schematic of the electrical analog circuit is shown in Fig. 5.9. The left circuit in Fig. 5.9 models electric circuit of the driving piezo, marked Left Piezo in Fig. 5.5. The right circuit of Fig. 5.9 models the sensing piezo, marked Right Piezo of Fig. 5.5.

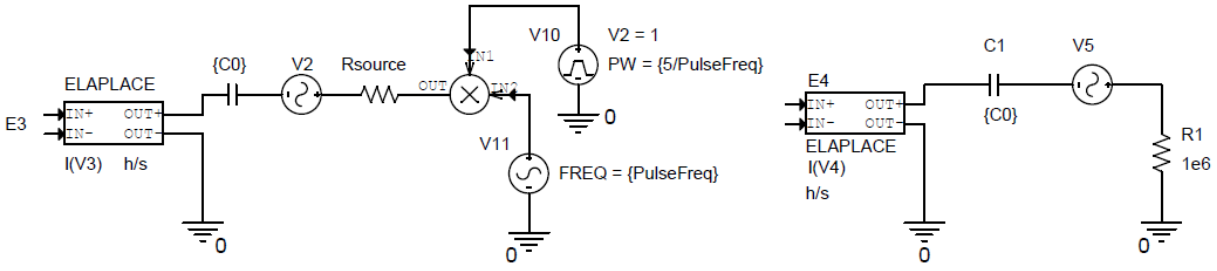

Figure 5.9 PSpice implementation of the Electric Circuit Left and Electric Circuit Right Piezos from Fig. 5.5

The model of the source for the driving piezo is a sinusoid multiplied by a square pulse. This was necessary because PSpice does not have a sinusoid burst component in its library. To implement a 5-cycle sinusoidal burst the frequency of the sinusoidal source sets the width of the pulse such that the pulse width is five times the period of the sinusoidal source.

The amplitude of the square pulse sets the amplitude of the sine wave, where the sinusoidal source has a constant amplitude of 1 V.

5.3.2 Testing and Results of first CRAS variant PSpice Model

In this section the testing results of the PSpice model for the CRAS transducer are presented. Two different sets of experiments were performed to verify the models. The results of each test were compared with physical measurements performed in the lab. In the first experiment, a frequency domain test was performed to compare the resonant behaviour of the model with that of the physical sensor. In the second experiment a time domain test was performed where the sensor was stimulated with a 5-cycle pulse at its resonant frequency of 52.3 kHz. The resulting vibration was then measured and compared with the physical sensor's transient response.

5.3.2.1 Frequency Domain Test of First CRAS Sensor

A frequency domain test was performed on the model for the first CRAS variation and the results are presented in Fig. 5.10. The frequency domain test is an important indicator of how well the model matches the behavior of the physical sensor. The measured resonance plot displays a skewed line between the series and parallel resonances, (52.27 kHz, 500 Ω) and (54.5 kHz, 4500 Ω).

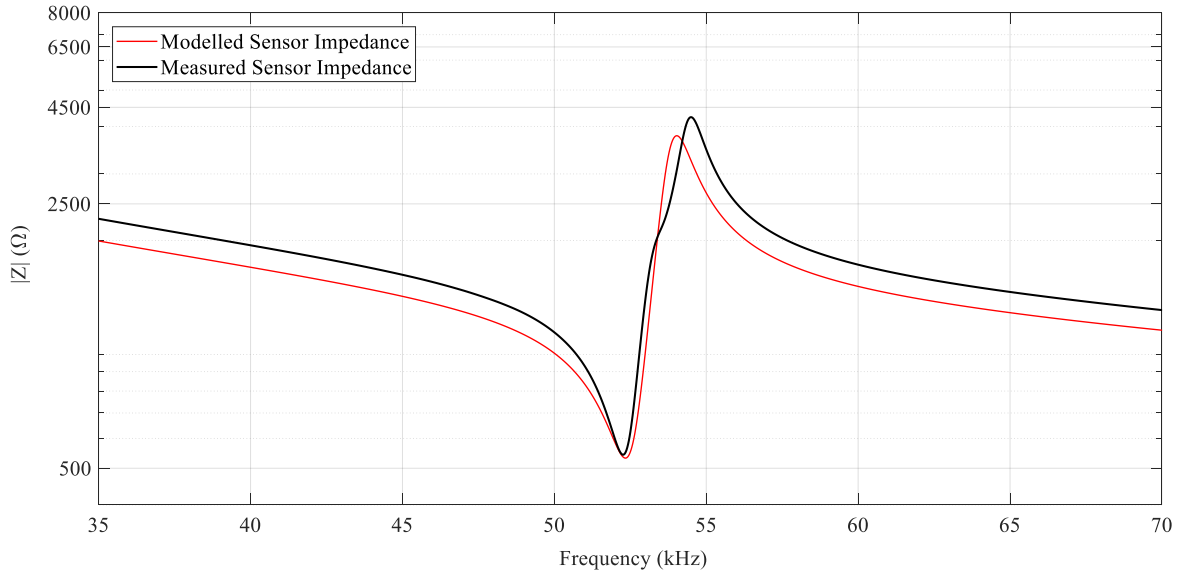

Figure 5.10: Frequency Response of first CRAS sensor with frequency response of the PSpice model

This skewing behavior, not captured in the model, is likely the result of multiple resonances in close proximity to the resonant frequency of the standalone piezo transducer, as observed in figs. 5.1, 5.2 and 5.4. It was found that an equivalent single resonator model which more closely matches the impedance plot of the measured sensor would have a much higher piezoelectric constant ($h_{33} \approx 3.5\, GN/C$). Thus, the multiple resonances have the effect of increasing the piezoelectric constant of the resonator when considered as a first order resonator.

5.3.2.2 Time Domain Response of First CRAS Sensor

In the lab the sensor was stimulated with a 5-cycle 250 mVpp sinusoidal burst, at the resonant frequency of the sensor, 52.3 kHz, and the same stimulus was applied to the model. The results of the lab test and the simulation are presented in Fig. 5.11. The measured and simulated results are taken before amplification, directly at the output of the sensing piezo.

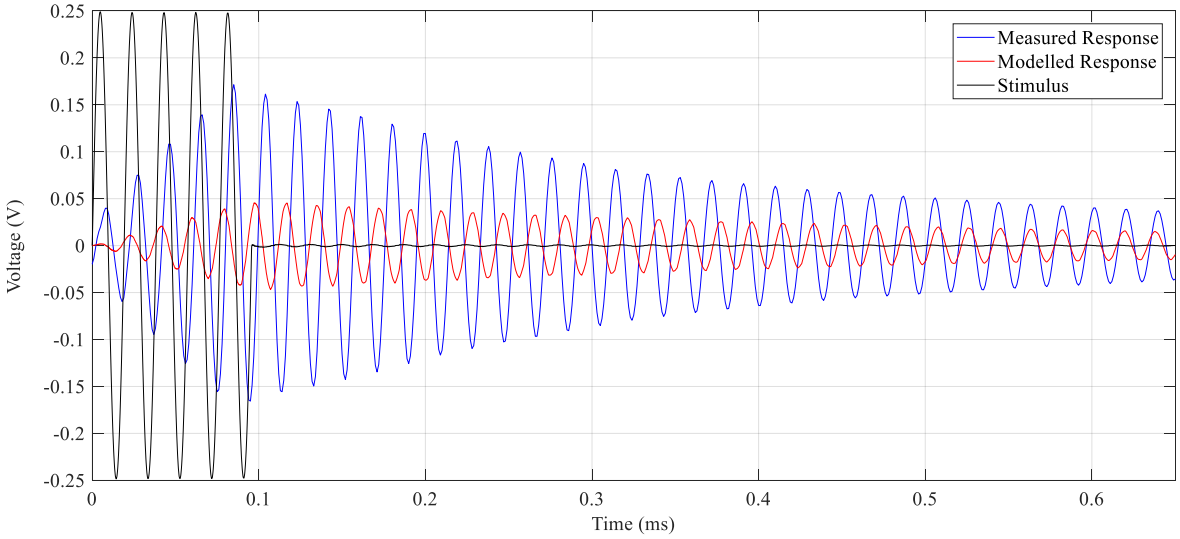

Figure 5.11: The time domain response of the first CRAS sensor. The stimulus is a 5 cycle sine burst, 250 mVpp. at the resonant frequency of the sensor, 52 kHz.

The maximum amplitude achieved by the model is a factor of two smaller than the measured response. This provides support to the assumption that the multiple resonance, noticeable from the skewed impedance behaviour of the physical sensor, has the effect of increasing the piezoelectric constant h. Using a larger piezoelectric constant in the model would cause the simulated transient response to more closely match the measured. However, increasing h_{33} would also greatly affect the frequency domain response of the transducer such that the modelled and measured impedance plots of the CRAS sensor would be further out of agreement. To produce a PSpice model that more closely resembles the real physical sensor behavior, a more sophisticated, multi-order resonant model would need to be produced.

5.4 PSpice Modelling of Second CRAS Variant

Here a PSpice model of the second CRAS variation is presented. As performed for the first CRAS variation, frequency and time-domain simulation were performed and their results were compared with measurements obtained in the lab.

5.4.1 PSpice Schematic of Second CRAS Variant

The PSpice model for the second variation is nearly identical to that of the first, except for the elements contained in the blocks “Left Sensor Section” and “Right Sensor Section”. In both the Left and Right Sensor Sections the Resin Epoxy transmission line is replaced with an Ag Epoxy transmission line. The PSpice implementation of the Left and Right Sensor sections is presented in Fig. 5.12 and 5.13.

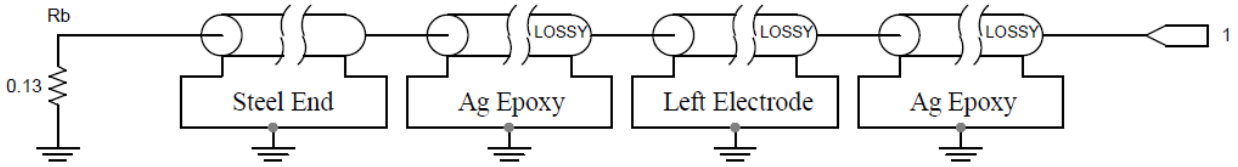

Figure 5.12 PSpice implementation of Left Sensor Section for second CRAS variation, with reference to Fig. 5.5

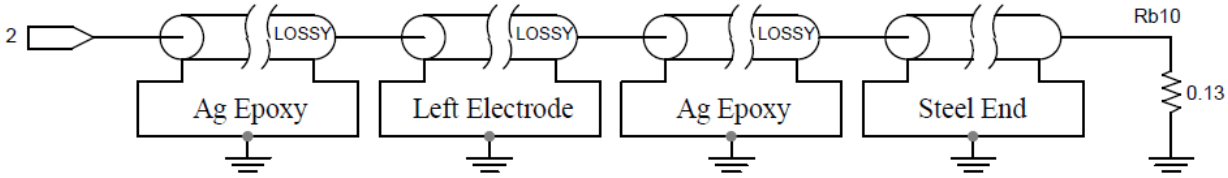

Figure 5.13 PSpice implementation of Right Sensor Section for second CRAS variation, with reference to Fig. 5.5

5.4.2 Testing and Results of Second Constructed Sensor Model

In this section the testing and results of the PSpice model for the second CRAS variant are presented. As for the first variant, two experiments were performed to verify the PSpice model of

the second CRAS variation. First, a frequency domain test was performed to compare the resonant behaviour of the model with that of physical sensor. Second, a time domain test was performed where the sensor was stimulated with a 5-cycle pulse at the series resonant frequency of the sensor 40 kHz.

5.4.2.1 Frequency Response of Second Constructed Sensor

A frequency domain test was performed on the model for the second CRAS variation and the results are presented in Fig. 5.14. Unlike the first variation, the second CRAS sensor has a straight smooth line

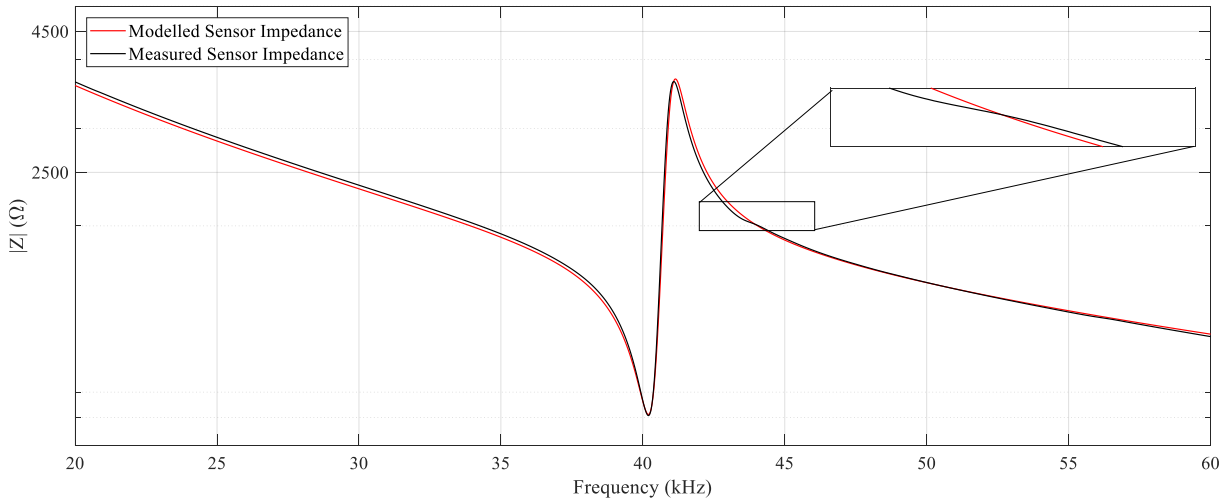

Figure 5.14: Frequency Response of second CRAS sensor compared with frequency response of the PSpice model

connecting its series and parallel resonances. The series resonance occurs at 40 kHz, and an impedance of 900 Ω; and the parallel resonance at 41 kHz, with an impedance of 3700 Ω. This series resonance impedance larger than the 500 Ω resonant impedance observed in the first CRAS variation. From these results we can infer that the Ag epoxy increases the losses of the constructed transducer. The second CRAS sensor does not demonstrate the same multi-resonance behaviour

near its series resonant frequency. The modelled resonance behavior is in strong agreement with that of the measured resonance. Therefore, it is possible to model the second CRAS sensor as a single resonator and achieve an impedance measurement that is in strong agreement with the measured result. The model and physical sensor coincide for most of the measured bandwidth. A portion of the plot where the curves do not coincide is highlighted in Fig. 5.14. The zoomed in region shows a small resonance mode in the measured impedance that is not captured in the model. The piezoelectric parameters used in the model were taken from the PRAP fitting performed in Section 5.1. When performing modelling of the second CRAS sensor, neither set of parameters was suitable for fitting the impedance curve of the measured sensor to that of the model. The fit achieved in Fig. 5.14 was obtained by combining the two PRAP fits. The C_0 value obtained from the first PRAP fit was combined with the h_{33} value obtained from the second PRAP fit. In this way the close matching between the modelled and measured resonance curves was achieved.

5.4.2.2 Time Domain Response of Second Constructed Sensor

The modelled and physical sensors are stimulated with a 5-cycle 200 mVpp sinusoidal burst, at the resonant frequency of 40 kHz. The results of this experiment are presented in Fig. 5.15. The measured and simulated results are taken before amplification, directly at the output of the sensing piezo.

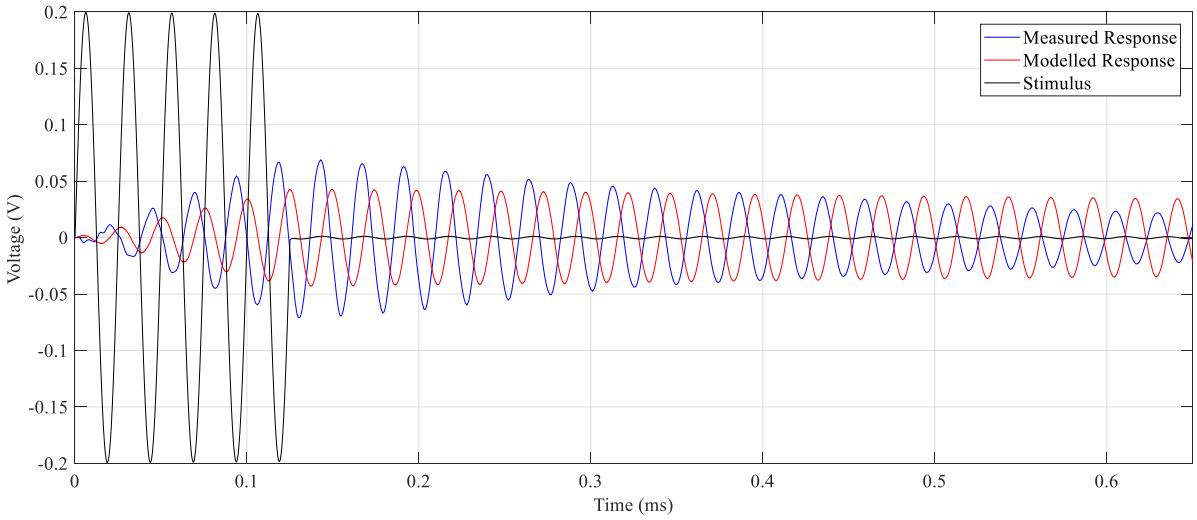

Figure 5.15: The time domain response of the second CRAS sensor. The stimulus is a 5 cycle sinusoidal burst, 200 mVpp. at the resonant frequency of the sensor, 40 kHz.

From Fig. 5.15 we observe that the transient response of the PSpice model is in good agreement with the transient response of the physical sensor. The modelled response reaches a peak value of 50 mV after a compared with a measured amplitude of 60 mV. The close agreement between modelled and measured transient responses can be attributed to the fact that the physical sensor more closely resembles a single resonator. If it were a multiple resonator, as seen in the first CRAS variation, the effective h of the single resonator model would need to be much higher to achieve an agreement in the voltage amplitude obtained after the 5-cycle sinusoidal burst at resonance is applied.

5.5 Conclusions

PSpice models for the standalone piezo transducer and the two CRAS variations were presented. The piezoelectric parameters for the PZT transducer used in our experiments were determined using PRAP analysis software. Using the parameters from PRAP, a model of the standalone piezoelectric transducer was developed. The two sets of parameters obtained from the PRAP fitting

were applied to the standalone sensor model and two different resonant curves were achieved for the modelled standalone piezo. Both impedance curves were in close agreement with the measured resonance curve of the piezo. The standalone piezo model was then combined with other elements to form PSpice models for the two CRAS variations. The CRAS models were verified by frequency and time domain testing, and the results were compared with those obtained in the lab. The results showed that model of the second CRAS variant were in strong agreement with the lab results. This close agreement can be attributed to the fact that the physical sensor does not have multiple resonances near its resonant frequency of 40 kHz. Unlike the second CRAS variant, the results obtained for the PSpice model of the first variant were not in good agreement with the lab results. This was attributed to the multi-resonance of the first CRAS sensor near its resonance frequency of 52 kHz. We conclude that the second CRAS sensor is the more suitable sensor to be used for future testing for corrosion in grounding rods. In the next chapter a PSpice model for corrosion testing in grounding rods is presented.

6 Modelling Corrosion Detection in Grounding Rods

The model developed in Chapter 5 for the second CRAS variation is here extended to model defect detection in grounding rods. The second CRAS variation will hereon be referred to as the CRAS sensor. The three grounding rod analogs introduced in Chapter 4, Rods A, D and E, are here modelled in PSpice. The modelled rods are connected in series with the CRAS model to model the physical connection of the CRAS sensor and the rods. A block diagram of the CRAS model connected to the rod model is shown in Fig. 6.1.

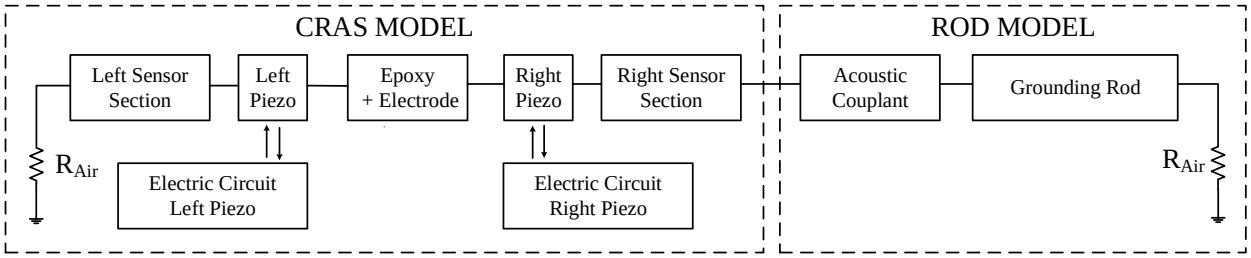

Figure 6.1: Block diagram of corrosion detection model in PSpice. The rod model is connected in series with the CRAS model presented in Chapter 5.

For each rod, modelled and physical, the CRAS sensor is excited by a 2 Vpp, 5-cycle sine burst at three different frequencies, 32.5 kHz, 40 kHz, and 50 kHz. These frequencies were chosen because of their proximity to the resonant frequency of the CRAS sensor, where 32.5 kHz and 50 kHz are above and below the resonant frequency, and 40 kHz coinciding with resonance. The modelled responses are compared with experiments performed in the lab. An ideal non-inverting operational amplifier was added at the model output with voltage gain equal to that used in the lab testing. This op-amp model is not included in the circuit schematics presented here, since its primary purpose was for matching the modelled signals to those obtained in the lab.

6.1 Modelling Defect Detection Using Rod A

In this section the PSpice model of Rod A is connected to the CRAS PSpice model, and the results of the simulation are compared with experiments performed on Rod A in the lab. The Rod A model consists of one transmission line element modelling the steel rod, and a second transmission line element modelling the acoustic couplant between the sensor and the rod. Mechanical losses are considered for the rod but neglected in the couplant. The steel rods in the lab have $L_{Rod} = 2.93\ m$, E_{steel} = 205 GPa, $\rho_{steel} = 7850\ kg/m^3$ and $A_{Rod} = 2.84 \times 10^{-4}\ m^2$. The lumped element values for the rod transmission line are then found according to (2.22), (2.23) and (2.26). The mechanical losses of the rod were accounted for by adjusting the per unit resistance of the transmission line for rod A. This resistance was found experimentally to be 1 $k\Omega$, and was assumed to be constant over the entire bandwidth. The acoustic couplant was modelled as a lossless transmission line, with electrical parameters $Z_{0_{cpl}}$ and $\tau_{d_{cpl}}$. These parameters are difficult to determine since acoustic impedance information for acoustic couplants are not readily available, and thus only typical values could be found according to datasheets from similar couplants [28].

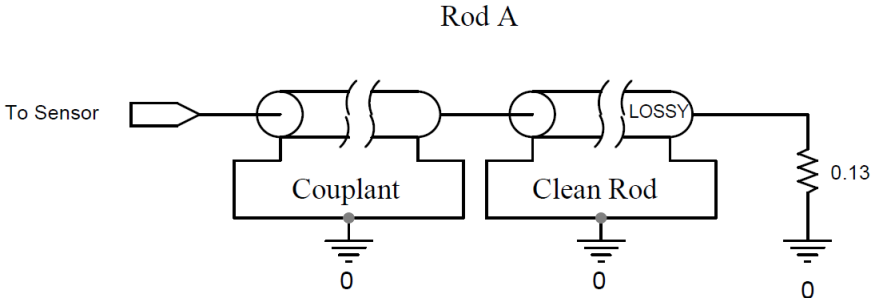

Figure 6.2: Schematic of Rod A PSpice model. Connector marked "To Sensor" indicates where the rod model is connected to the CRAS model introduced in Chapter 5

In all the rod experiments the acoustic impedance of the couplant was chosen to be $Z_{0_{cpl}} = 250\ \Omega$ and the time delay $\tau_{d_{cpl}} = 3.33 \times 10^{-8}\ s$, according to $v_p = 1500\ m/s$ in the couplant, and an estimated couplant thickness of 50 μm. The schematic of the Rod A model implemented in PSpice is shown in Fig. 6.2.

6.1.1 Simulation Results for Rod A at 32.5 kHz

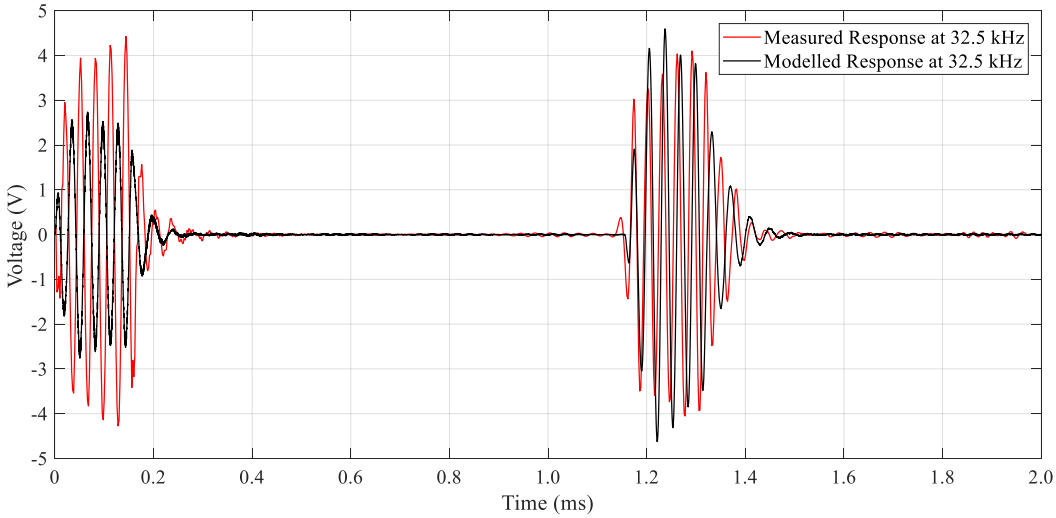

Figure 6.3: Simulation and Lab results of CRAS sensor connected to Rod A, excited at 32.5 kHz, 5 cycle sine burst at 2 Vpp

The simulation results for defect detection in Rod A is compared with the experimental results in Fig. 6.3. The simulated result matches the main features of the measured results. The timing of the injected pulse and the received echo are well matched, with the echo off the end of rod occurring at approximately 1200 μs. The voltage levels are also well matched. The excitation pulse of the model is 60% less than the measured result. This difference is likely the result of an imperfect modelling of the CRAS sensor itself. As seen from Fig. 5.15, the maximum amplitude achieved by the sensing piezo is 15 mV less in the model than the physical sensor. The root cause of this

difference is not certain, but a possible explanation is that the piezoelectric constant, h, of the CRAS sensor is larger than the value used in the model, $2.44\times 10^{9}\ N/C$. A larger h results in larger vibrations, from smaller voltages, and vice versa. However, since a larger h has a strong effect on the observed resonant behavior of the device, it is not a simple matter of adjusting the h to make the output amplitude of the model the same as the observed amplitude.

6.1.2 Simulation Results for Rod A at 40 kHz

The model was changed so that the CRAS sensor was excited at the CRAS resonant frequency of 40 kHz. The simulation and experimental results are compared in Fig. 6.4. It is observed that main features are matched between the model and the experiment. However, the amplitude of the echo off of the end of the rod at the resonant frequency in the model is considerably less than the echo observed in the experiment.

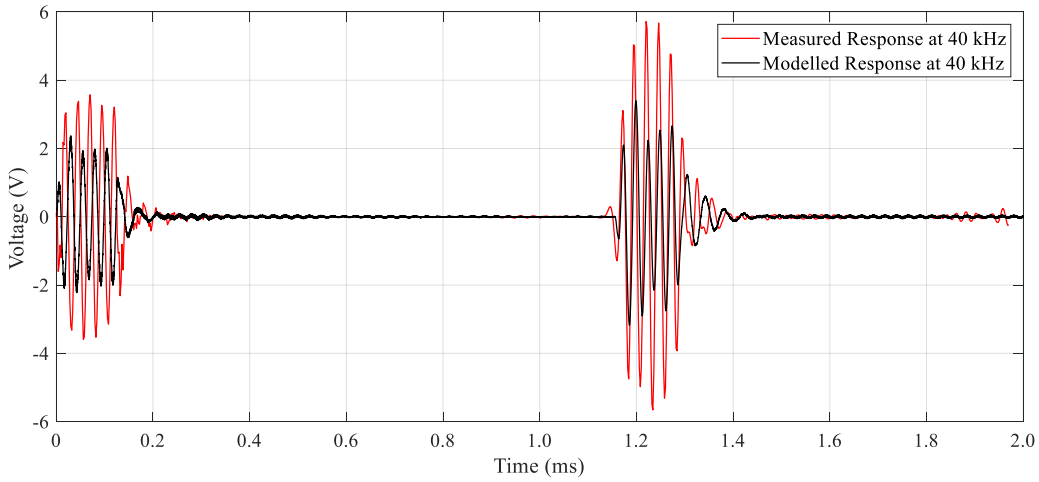

Figure 6.4: Simulation and Lab results of CRAS sensor connected to Rod A, excited at 40 kHz, 5 cycle sine burst at 2 Vpp

Whereas the echo is well matched at 32.5 kHz, as observed in Fig. 6.3, there is a considerable difference observed at 40 kHz. A possible cause of this difference is that the rod is modelled as

having constant loss over the entire bandwidth. Closer matching of the modelled to experimental results may be achieved by introducing a better model for the rod which incorporates a frequency dependent loss. It is also possible that the coupling between the CRAS sensor and the rod is also frequency dependent. Thus, a more developed model of the coupling between the CRAS and rod may also improve the model's accuracy.

6.1.3 Simulation Results for Rod A at 50 kHz.

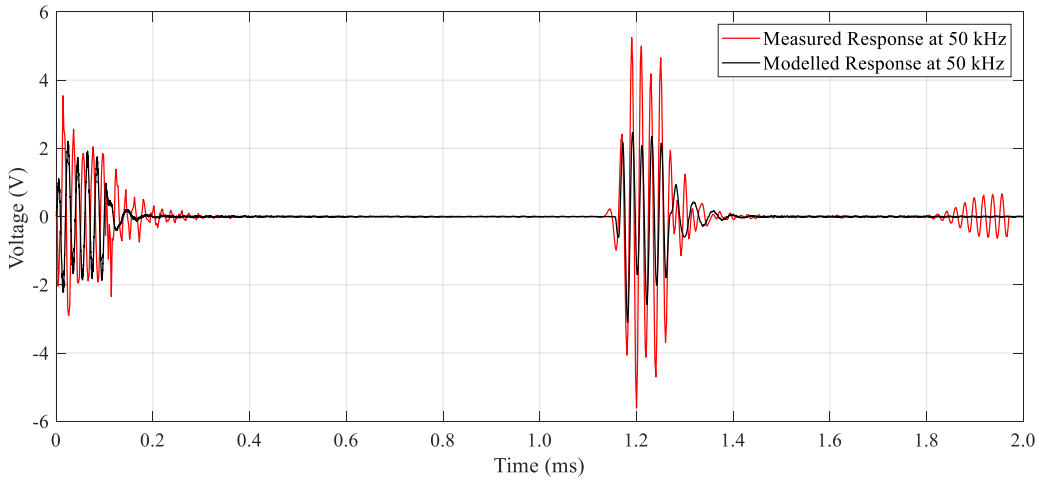

Figure 6.5: Simulation and Lab results of CRAS sensor for Rod A, excited at 50 kHz, 5 cycle sine burst at 2 Vpp

The simulation and experimental results for Rod A at 50 kHz are presented in Fig. 6.5. The modelled pulse amplitude is well matched to the experimental results at 50 kHz. However, the echo signal off the end of the rod is not. The amplitude of the echo wave in the experiment is a factor two greater than the injected pulse. However, in the model the pulse and the echo have nearly the same amplitude. As mentioned in 6.1.2, a more accurate model for the rod, one which includes frequency dependent loss in the rod, might reduce this discrepancy. Observed in the experiment but not in the model is a vibration occurring at 1.8 ms. This vibration is caused by a

slower wave mode travelling in the rod introduced by the CRAS sensor which is not captured in the model.

6.2 Modelling Defect Detection Using Rod D

In this section the PSpice model of Rod D is connected to the CRAS model, and the results of the simulation are compared with experiments performed on Rod D in the lab. As observed in Fig. 6.6, Rod D is modelled as three different transmission line elements, having lengths 1.46 m, 0.01 m, and 1.46 m, respectively.

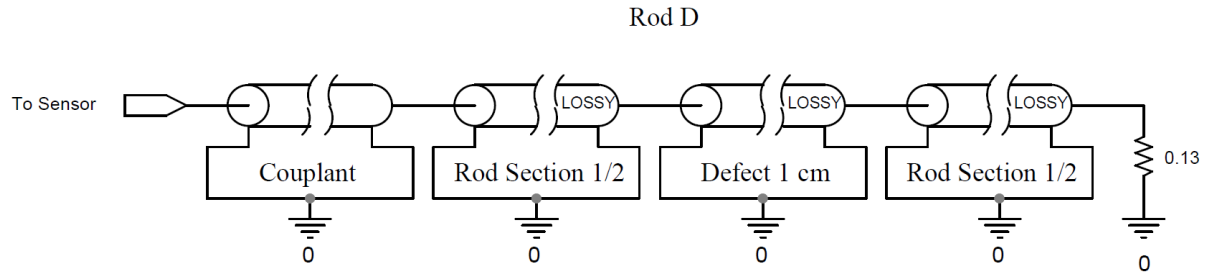

Figure 6.6: Schematic of Rod D PSpice model. Connect marked "To Sensor" indicates where the rod model is connected to the CRAS model from Chapter 5

The three transmission lines together constitute the full rod length of 2.93 m. The long transmission lines, representing the defect-free portions of Rod D, have identical properties to Rod A apart from their length. The defect is modelled according to its physical properties, having length $L_{defect} = 0.01\,m$, $A_{defect} = A_{steel}/2 = 1.42 \times 10^{-4}\,m^2$, $\rho_{defect} = \rho_{steel}$ and $E_{defect} = E_{steel}$. The transmission line parameters for the defect are then found from (2.36) – (2.39). The defect effectively introduces an impedance mismatch at the boundary between the two half Rod Sections. Since A_{defect} is half that of the rod, from (2.36) we see that so also will Z_{defect} be half that of the rod. Thus, from (2.40), the acoustic wave incident on the defect will have reflection coefficient

$\Gamma_{defect} = 0.5$. Thus, we expect the amplitude of the echo off of the defect to be half the amplitude of the pulse injected into the rod.

6.2.1 Simulation Results for Rod D at 32.5 kHz

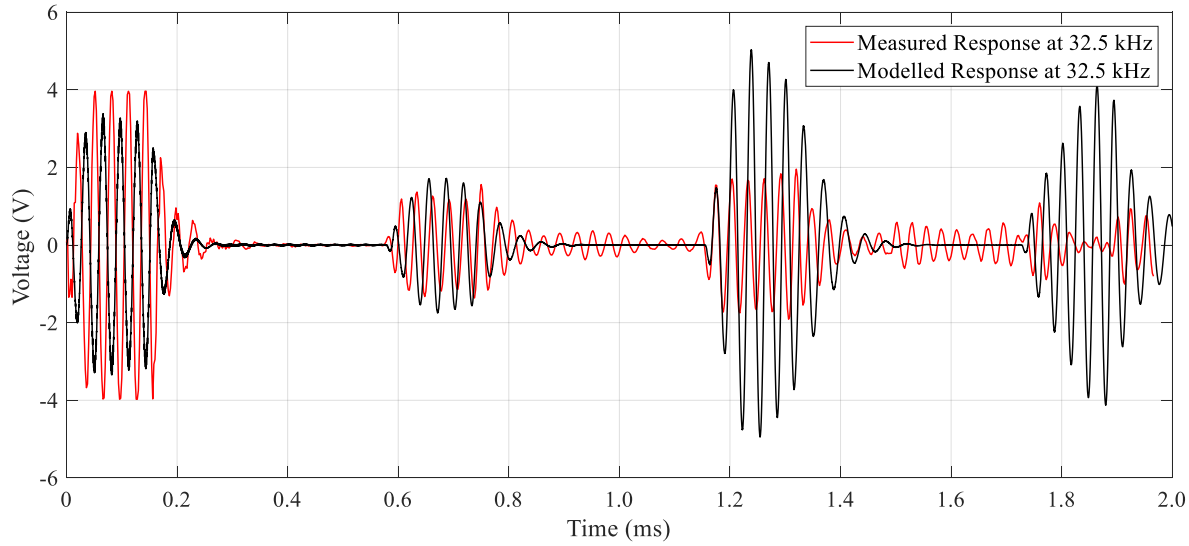

Figure 6.7 Simulation and Lab results of CRAS sensor connected to Rod D, excited at 32.5 kHz, 5 cycle sine burst at 2 Vpp

The simulation results for defect detection in Rod D at 32.5 kHz is compared with experimental results and presented in Fig. 6.7. The main artifacts of the measured result are well matched by the model. The amplitude of the injection pulse and echo off of the defect are well matched. However, the measured echo off the end of the rod is a factor of two less than the echo observed in the model. One explanation for this behavior is mode conversion occurring at the defect-rod interface. Mode conversion may result in vibrational modes that destructively interfere with each other. This interference may be an explanation for the discrepancy in the measured to modelled signal at the defect, and rod end, in Fig. 6.7. This provides further evidence that the model for the rod and defect require further consideration to better match the experimental results.

Not captured in the model is wave mode conversion occurring at the defect as observed in the measured result. A smaller echo is observed arriving at the CRAS sensor shortly after the first echo of the defect. This is certainly the result of mode conversion. Mode conversion is likely the cause of the distorted echo observed in the measured result around 1.8 ms. As observed in the model, another relatively large echo is expected at that interval, but in the measurement the echo is missing entirely. A possible reason for this missing echo is the result of destructively interfering echoes in the rod resulting from mode conversion at the defect – rod boundary.

6.2.2 Simulation Results for Rod D at 40 kHz.

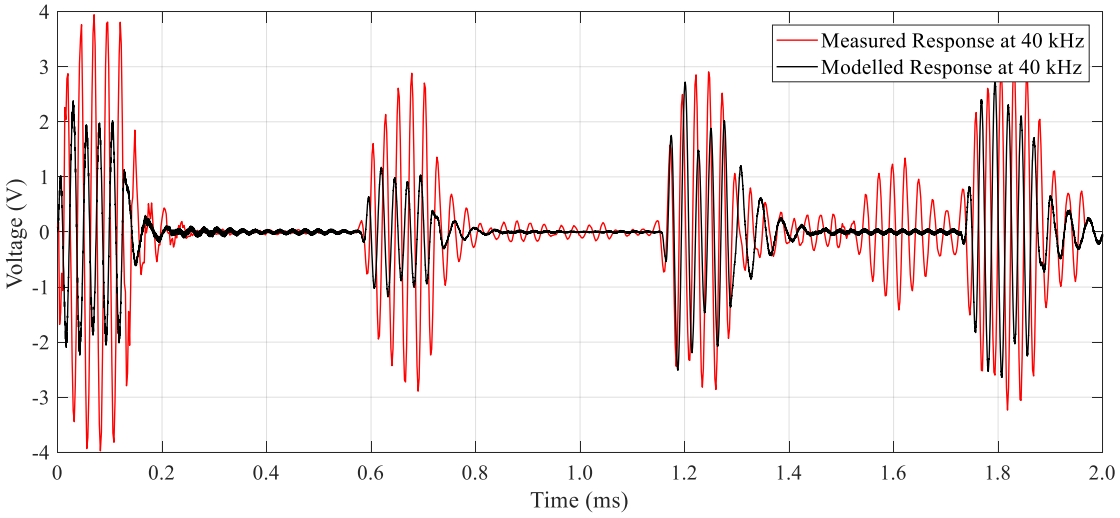

Figure 6.8 Simulation and Lab results of CRAS sensor connected to Rod D, excited at 40 kHz, 5 cycle sine burst at 2 Vpp

The simulation result for 40 kHz excitation and the associated measured result are presented in Fig. 6.8. The modelled echo off the end of the rod at 40 kHz is more closely matched to the measurement than at 32.5 kHz. However, the echo off the defect is not as well matched. The measured echo off the defect is a factor of two greater than the modelled echo off the defect. Mode conversion is observed after the third echo at approximately 1.6 ms. The fourth modelled echo is

well matched to the measured result. It is not certain why the echo off the defect is larger in the experiment than what is predicted by the model.

6.2.3 Simulation Results for Rod D at 50 kHz

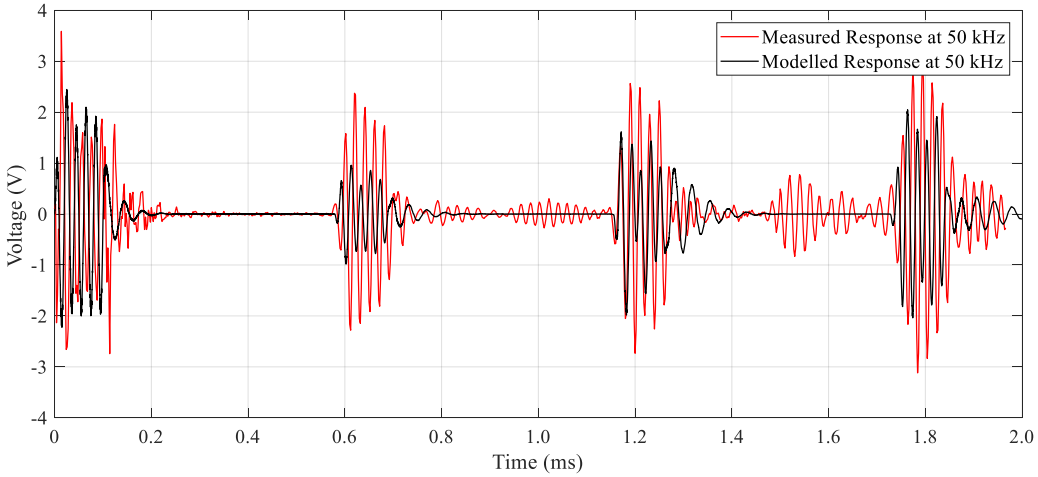

Figure 6.9: Simulation and Lab results of CRAS sensor connected to Rod D, excited at 40 kHz, 5 cycle sine burst at 2 Vpp

The simulation result for 50 kHz excitation and the associated measured result are presented in Fig. 6.9. The pulse amplitude of the model is well matched to the measured pulse. Mode conversion is observed at 1.0 ms, 1.5 ms and 1.9 ms. As was observed in the 40 kHz experiment for Rod D, the echo off of the defect is a factor of two greater in the measurement than what is observed in the model.

6.3 Modelling Defect Detection Using Rod E

In this section the PSpice model of Rod E is connected to the CRAS model, and the results of the simulation are compared with experiments performed on Rod E in the lab. The PSpice model of Rod E is nearly identical to Rod D, where the defect is modelled exactly the same as in Rod D,

and the two defect-free portions of the rod differ only in their lengths. To model the defect as being at a quarter-length distance down the rod, the first Rod Section is 0.7275 m, and the second Rod Section is 2.1925 m. The schematic of the model for Rod E as implemented in PSpice is presented in Fig. 6.10.

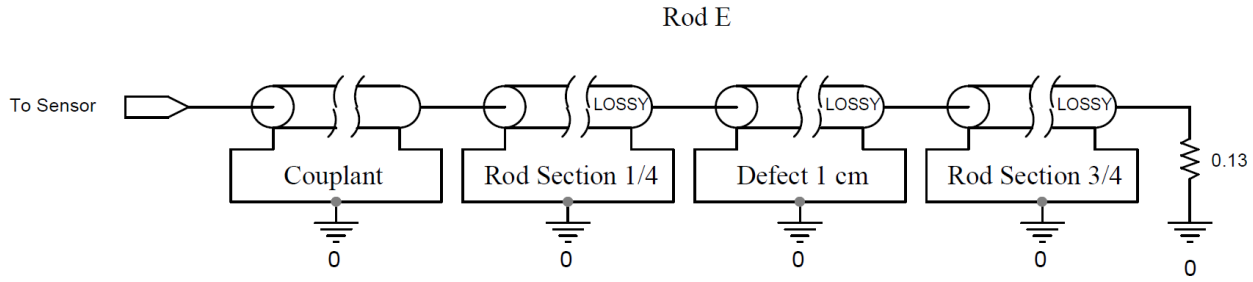

Figure 6.10: Schematic of Rod D PSpice model. Connect marked "To Sensor" indicates where the rod model is connected to the CRAS model from Chapter 5

6.3.1 Simulation Results for Rod E at 32.5 kHz.

The simulation results for defect detection in Rod E at 32.5 kHz is compared with experimental results and presented in Fig. 6.11. The main artifacts of the measured result are matched by the model. The amplitudes of the echoes in the model are significantly greater than the recorded echoes. It is apparent that the model predicts much greater amplitudes for the echoes and even the injection pulse. From the modelled results, the amplitude of the injection pulse is uniformly affected by the modelled; regardless of whether there was defect in the rod model or not, the injection pulse amplitude remained constant when each rod was excited at the same frequency. However, comparing the result present in Fig. 6.11 to Fig. 6.7, it seen that the amplitude of the measured pulse is nearly a factor of two less than the measured pulse in rod D at 32.5 kHz. Thus, it is apparent that repeatability for the measured results is difficult due to the nature of how the pulse injected into the rod. Depending on how well the CRAS is fixed to the rod, the pulse

amplitude will be similarly affected. What is uncertain is why the amplitude of the echoes in the measurement relative to the pulse amplitude is significantly different than what is observed in the model.

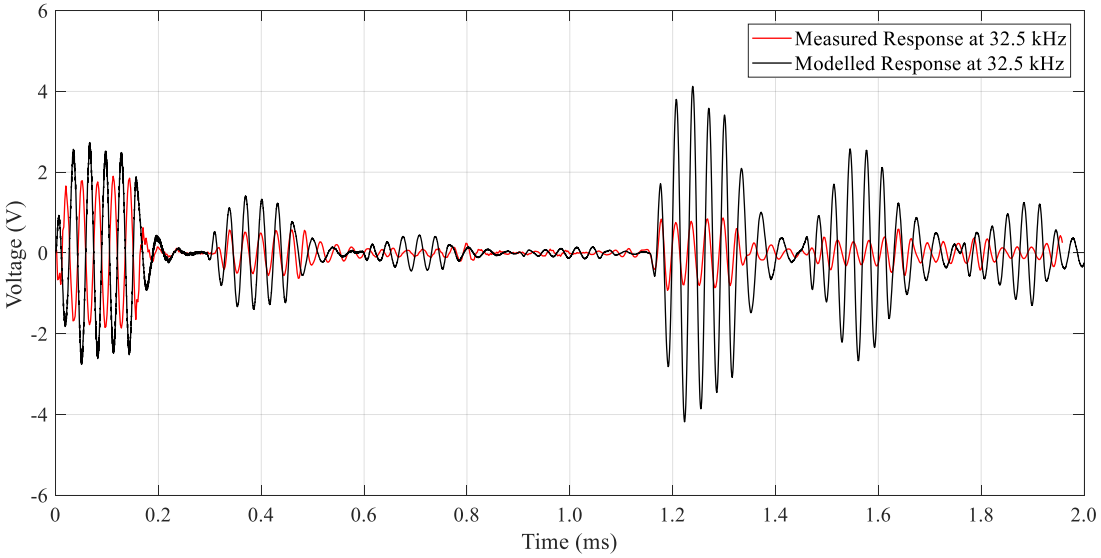

Figure 6.11: Simulation and Lab results of CRAS sensor connected to Rod E, excited at 32.5 kHz, 5 cycle sine burst at 2 Vpp

6.3.2 Simulation Results for Rod E at 40 kHz

The simulation result for 40 kHz excitation and the associated measured result are presented in Fig. 6.12. The modelled echo off the end of the rod at 40 kHz is more closely matched to the measurement than at 32.5 kHz for Rod E. The echo off the end of the rod in the model is well matched to the experimental results. Mode conversion is observed after the echo off of the defect, at approximately 0.8 ms, as well as after the 4th large echo at 1.6 ms.

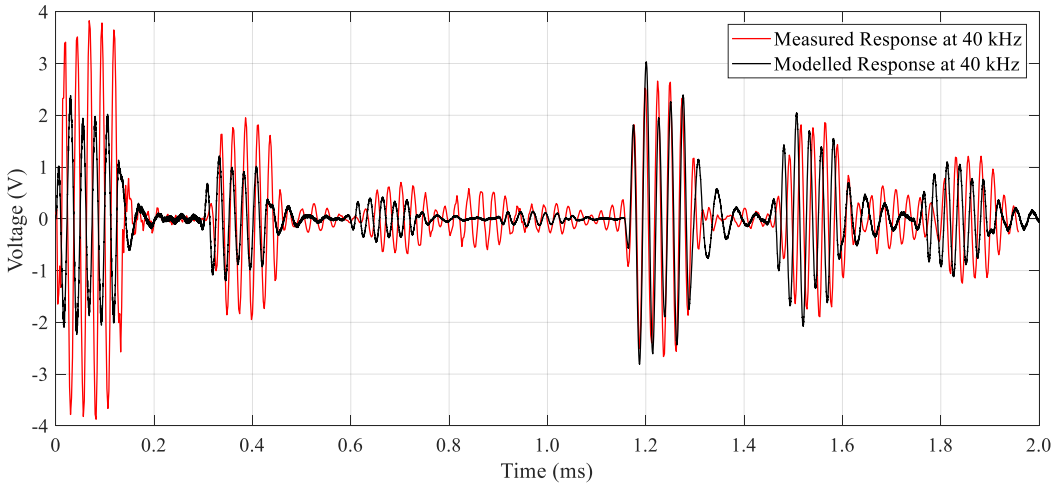

Figure 6.12: Simulation and Lab results of CRAS sensor connected to Rod E, excited at 40 kHz, 5 cycle sine burst at 2 Vpp

6.3.3 Simulation Results for Rod E at 50 kHz

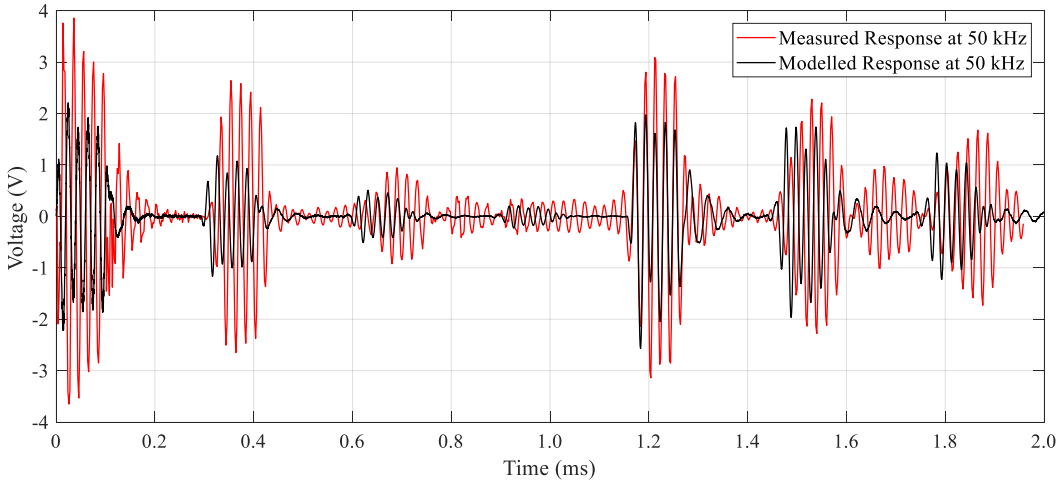

Figure 6.13: Simulation and Lab results of CRAS sensor connected to Rod E, excited at 50 kHz, 5 cycle sine burst at 2 Vpp

The simulation result for 50 kHz excitation and the associated measured result are presented in Fig. 6.13. Unlike the other rods excited at 50 kHz, the amplitude of the measured pulse is much larger than what is expected. Using Fig. 6.5 and 6.9 as a reference, the physical coupling of the sensor to the rod in the experiment was less in this experiment. As a result of this reduced coupling

a larger amplitude is observed in the CRAS sensor than what is predicted by the model. This larger amplitude is because the rod does not dampen the pulse as much when the quality of the coupling between the rod and the sensor is reduced.

6.4 Conclusions

The model developed for the CRAS transducer was extended to model defect detection in grounding rods. Three grounding rod analogs, Rods A, D and E, were modelled in PSpice and connected in series with the CRAS model. The three rod models were tested with identical stimuli for three different frequencies, 32.5 kHz, 40 kHz, and 50 kHz. The results show that the model demonstrates close agreement with the measurements performed in the lab. However, the modelled defects resulted in simulation results that were not in close agreement to the measured behavior. Further development of the model for the rods, and in particular their defects, is an important consideration for future work.

7 Hardware Implementation

7.1 Introduction

It was important to have a portable testing device that can be brought to and from the field for testing. The benchtop setup in the lab is big, heavy, requiring many hours to complete a test due the inconvenience of using benchtop equipment. The function generator needs to be programmed at each frequency of interest, and the oscilloscope needs to be painstakingly tended to in order to make sure that the correct functionality is observed. This functionality includes correct averaging, configuring the time and voltage scales for each frequency, and the tedious task of using the knobs and buttons to name each CSV file for saving to the USB flash drive. Therefore, a portable and automated testing device was required to making field testing much easier and faster.

7.2 System Requirements

Table 7.1 Table of requirements for pulse-echo transceiver embedded system board

No.	Description of Requirement
1	Be equipped with ADC to capture pulse-echo signals with approximately 1 Sample per μs
2	Be capable of generating a sinusoidal burst of varying frequencies from [20 – 100 kHz]
3	Be fitted with an output circuit to condition output signal suitable for CRAS sensor
4	Input Amplifier with minimum 200 kHz BW and gain of 100, with filter for 60 Hz
5	Be fully automated with limited user input
6	Perform a sweep over 32 frequencies with an adjustable number of averages
7	Be independently powered from a 12 V battery supply
8	Have the ability to connect to a laptop for viewing of program status.
9	Store data automatically onto SD card
10	Be compactly designed on a PCB protected by an enclosure suitable for field testing
11	Protect ADC all pins from overvoltage by limiting any voltage inputs to 3.3 V or less.

7.3 System Description

A fully integrated pulse-echo transceiver has been developed that accomplishes the system requirements based on the Teensy microcontroller [29]. A block diagram of the implemented system is presented in figure The Teensy 3.6 microcontroller is rated for 180 MHz clock frequency, but the system has been modified to run at an overclocked frequency of 240 MHz. As explored in the following sections, this was necessary to accomplish the system requirements for fast sampling and signal output. The output signal drives a piezoelectric transducer which sends an acoustic pulse down the steel rod. The echo is captured by the input amplifier and filter network which is then sampled by the ADC at 1.1 $\mu s/sample$. The samples are averaged 100 times at each frequency [20, 100] kHz, and the results are stored to an SD card onboard the Teensy. The block diagram of this system is represented in Fig. 7.1.

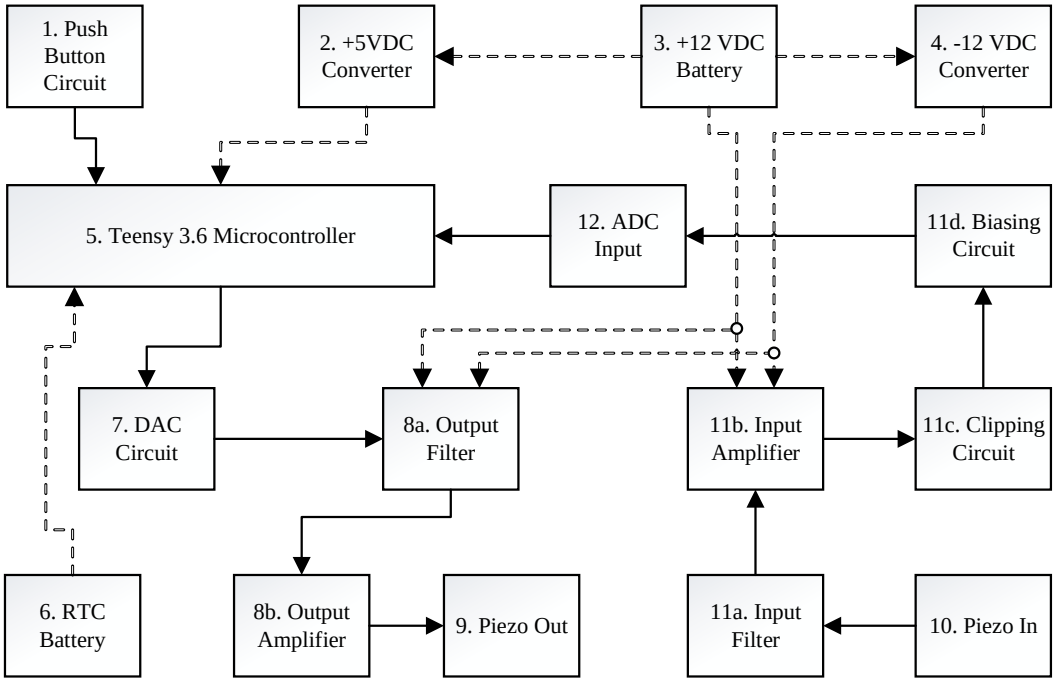

Figure 7.1: Block diagram for the implementation of the pulse-echo transceiver board

In the following sections the different components of the board represented in Fig. 7.1 are discussed in detail, including the nature of their design and implementation.

7.4 User Interface

The user interface consists of a push-button, an LED for visual feedback from the program during the test, and serial output which can be viewed from the Serial Monitor in the Arduino IDE. The user presses the pushbutton to initiate a test, and the LED flashes intermittently to signify the test is being performed, and the relevant verbose output is directed to the serial port to be observed by the user.

7.4.1 Push Button Circuit

A push button circuit was implemented to serve as the human-board interface. A user presses the button and the test begins. A hardware button debouncing circuit is also implemented using an RC filter. The pushbutton is used in conjunction with a pull-down resistor on the Teensy board. When the push button is pressed, the I/O pin attached to the push button is pulled to ground, triggering a hardware interrupt. The configuration of the interrupt and the pull-down resistor is configured in software. Additionally, a blue LED illuminates when the push-button is pressed, indicating that a test has begun. This LED stays lit until the test is complete, at which time it blinks 3 times.

7.4.2 LED Feedback

A blue LED is illuminated at the beginning of the test. The LED blinks twice after each pulse-echo-average sequence is completed for the current frequency under test. After all the frequencies have been tested, the LED blinks 3 times and turns off, signifying that the test is complete.

7.5 Power Supplies

The pulse-echo transceiver system draws power from 4 different power supplies, a +12 VDC battery, a -12 VDC switching converter, a 5 VDC voltage regulator, and an RTC battery. The power supplies are shown with dotted lines in Fig. 7.1.

7.5.1 +5 VDC Converter

To meet the requirements of 7 and 8, an LM7805C regulator converts the input 12 VDC from the battery to 5 VDC. It provides a power supply for the Teensy board via the V_{in} pin. The LM7805, made by Texas Instruments, can supply up to 1.5 A, which is a factor of 10 greater than the measured supply current for the entire system. A schematic of the 5 VDC converter is shown in Fig. 7.2. The 5 VDC to the V_{in} was required because the Teensy board specifications state that the power supplied to the V_{in} pin must be in the range of [3.6 V, 6.0 V], since the Teensy has a voltage regulator onboard, which converts the input voltage (normally from USB) to 5 VDC.

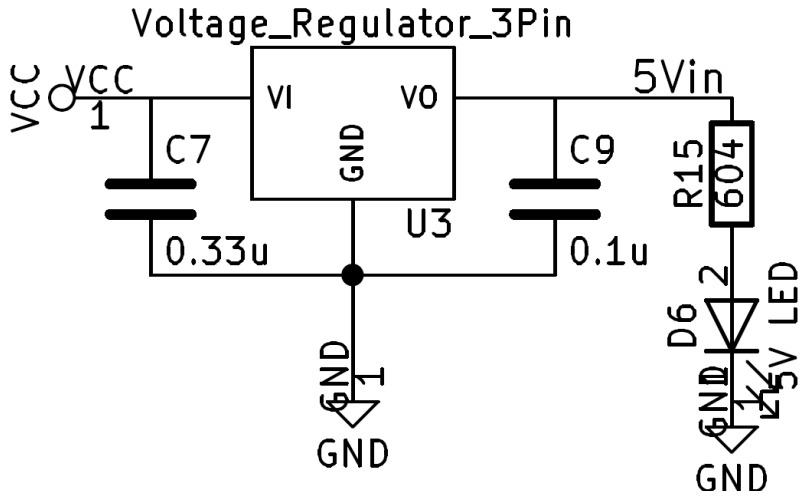

Figure 7.2: Diagram for 5VDC Converter

7.5.2 +12 VDC Supply

The +12 VDC supply is necessary to satisfy Requirement 7. The supply is a dual screw terminal connector that connects wire leads from a battery. This battery is taken into the field along with the board to perform testing.

7.5.3 −12 VDC Converter

The LT1054 is based on the switched-capacitor method and incorporates a voltage regulator as well. The switched-capacitor converter in the IC converts +12 VDC to −12 VDC at a switching frequency of 25 kHz. A schematic of the -12 VDC converter implementation is shown in Fig. 7.3.

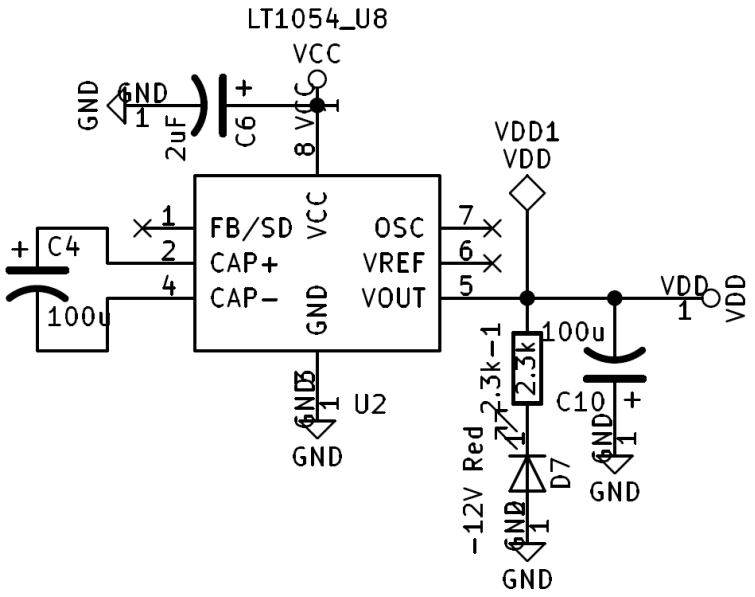

Figure 7.3: Diagram for -12VDC Converter

At the same time, the voltage regulator works to maintain a constant output voltage of -12 VDC. The drawback of using this switching converter is that it introduces 25 kHz noise into the power

supply of the input amplifier. To get rid of this noise, a simple low pass filter was placed in series with the -12 V supply bus at the output of the -12 VDC converter, marked VDD in Fig. 7.2.

7.5.4 Teensy 3.6 Microcontroller

The Teensy 3.6 is a microcontroller based on the Kinetis Microcontroller Unit (MCU), MK66FX1M0VMD18 [30], is made by NXP Semiconductor (formerly Freescale Semiconductor). The MCU package, shown in Fig. 7.4, is complete with RAM, ROM, crystal oscillator, and an I/O control unit. The Teensy board is developed by PJRC, a company who manufactures microcontrollers compatible with Arduino Interactive Development Environment (IDE) [29].

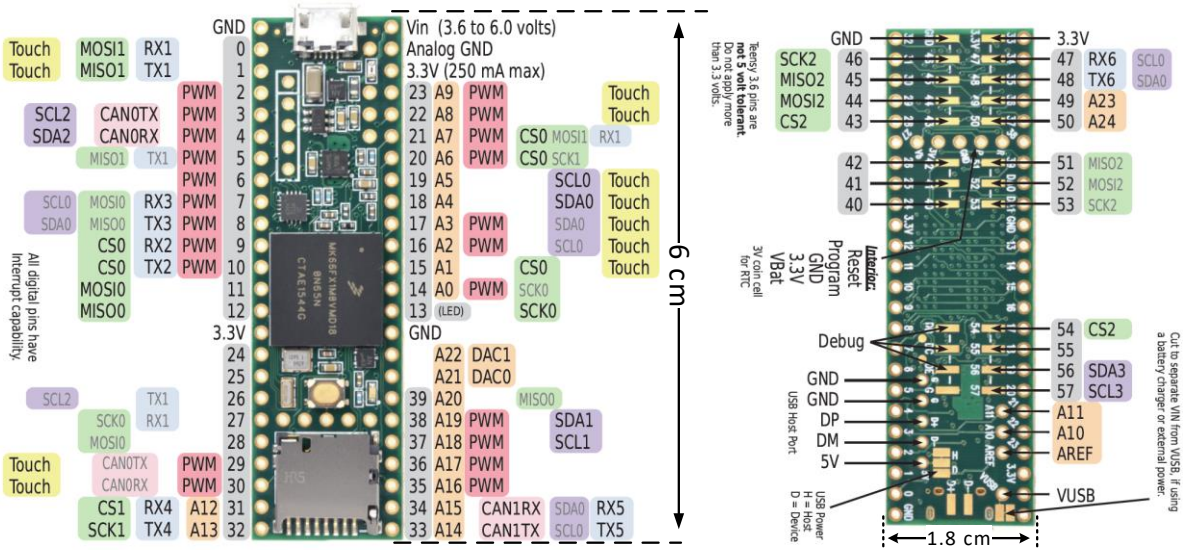

Figure 7.4: Pinout diagram of Teensy 3.6 by PJRC

The Teensy 3.6 is unique because it offers a variety of features not available in any Arduino Microcontroller, including much higher clock rates, fast ADC sampling, compact size, built in SD card, and I/O pin availability. Moreover, the Teensy libraries are designed to be compatible with existing Arduino functions and libraries while coming complete with a wide array of custom

functions and libraries. The Teensy was chosen in order to fully satisfy requirements 1, 2, 9 and 10. Additionally, the system was designed around the Teensy to be fully integrated on a custom PCB, and its compact size made it a convenient choice to fit on the PCB and inside the enclosure. The core of the Teensy 3.6 library is contained in the header file *kinetis.h*. In that header file the full memory space of the Kinetis chip is defined using C macros. The author took great care to account for the full spectrum of registers and modules outlined in the Kinetis reference manual. This was no small task as the reference manual is nearly 2300 pages long. Moreover, all the features offered by the Kinetis chip are provided with predefined classes in their respective libraries, including, the ADC, timers, RTC, PWM, etc. The Teensy requires the use of a plugin with Arduino called Teensyduino that is installed on top of the Arduino IDE package. The Teensyduino plugin provides the user the capability to select the global clock, with options to both under-clock the processor from 180 MHz down to 2 MHz and overclock up to 240 MHz. This functionality is not available in any Arduino model, to the best of this author's knowledge, at the time of this works' publication.

7.5.5 RTC Battery

The RTC battery is used to provide backup power to the RTC built into the Kinetis chip. The RTC battery is specifically dedicated to the RTC module on the Kinetis chip, who's memory contains the present date and time and is synced at the time of programing. The date and time is then maintained by the RTC module by means of the RTC oscillator. In field testing the time and date is used to form the name of the working directory for each corrosion detection measurement. The RTC module is fully defined in the Teensy library.

7.6 Custom DAC Implementation

A customized DAC was designed because the onboard DAC of the Teensy was not sufficiently fast to support signal generation up to 100 kHz. The DAC is implemented by means of a hardware timer available on the Teensy MCU, called the Periodic Interrupt Timer (PIT). The PIT triggers voltage samples to be delivered to the output of Port D on the MCU. The implementation of the custom DAC is described in this section.

7.6.1 Voltage Sample Outputs from PIT IRQ Vector

The PIT module is configured to trigger an interrupt service routine in software that outputs a sample to Port D at a fixed interval. This interval, called the PIT Load Value (N_{PIT}) is software configurable, and is stored into a physical register on the MCU. The PIT derives its clock directly from the bus clock of the Teensy board. For the Pulse-Echo board this clock frequency is 80 MHz. The PIT frequency corresponds to the PIT base period T_{base} = 12.5 ns.

Thus, the period between each IRQ from the PIT is governed according to the relationship:

$$T_{PIT} = N_{PIT} T_{base} \tag{7.1}$$

A vector of 32 PIT load values are stored in software, and their values are systematically loaded into the PIT LDVAL register over the course of the frequency sweep. The testing of these 32 values are presented later in this chapter. The period of the output signal, at the output of the DAC, is proportional to T_{PIT} and is found according to the relationship:

$$T_{out} = T_{PIT} N_T \tag{7.2}$$

Where N_T is the number of samples output by the DAC per signal period. On the Pulse-Echo board $N_T = 12$ was chosen. This value was high enough to produce a high-quality sine wave at the DAC output without burdening the PIT with a small T_{PIT} at higher output frequencies.

7.6.2 Implementation of DAC Using an R2R Ladder

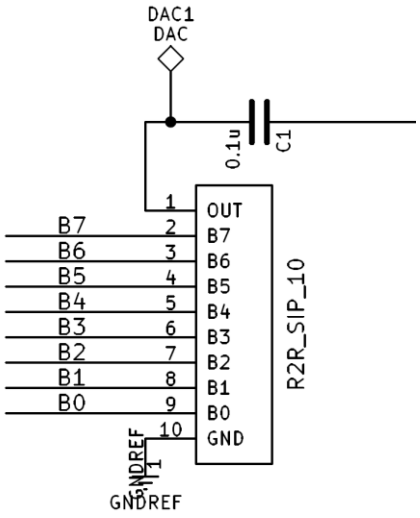

Figure 7.5: Diagram showing the 8 bits of Port D from Teensy MCU to DAC R2R ladder

The custom DAC uses 8-bits of Port D on the Kinetis MCU. These 8-bits are hardwired to 8 digital I/O pins on the Teensy board. These pins are then parallel connected to a 10-pin Single Inline Package (SIP) R2R resistor ladder network [31] as shown in Fig. 7.5. Pins B0 through B7 are connected to bits 0 through bit 7 of Port D of the MCU. The output analog voltage will be in the range of 0-3.3 V, and is accomplished by a hardware-implemented summation of the 8 bits according to the following relation [31]:

$$V_{out} = V_{Ref}\left(\frac{b_0}{2^8} + \frac{b_1}{2^7} + \frac{b_2}{2^6} + \frac{b_3}{2^5} + \frac{b_4}{2^4} + \frac{b_5}{2^3} + \frac{b_6}{2^2} + \frac{b_7}{2^1}\right) \tag{7.3}$$

From (7.3), an 8-bit resolution DAC can be achieved. Since DAC output has only 8-bit resolution, the resulting sinusoid will show step-like features because of the relatively low resolution, as shown in Fig. 7.6.

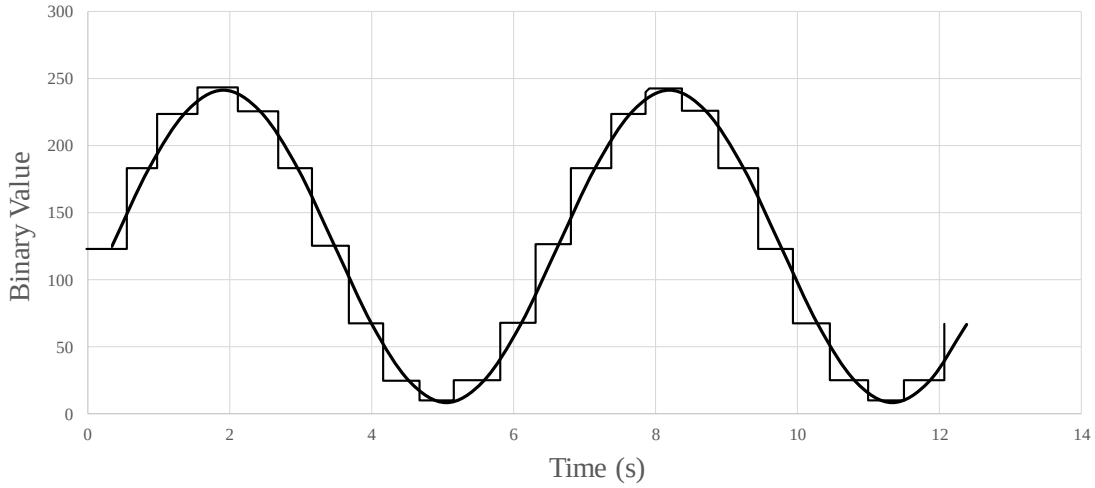

Figure 7.6: Figure for voltage steps of DAC

The effect of these voltage steps are the introduction of undesirable high frequency components into the output signal. To eliminate these high frequencies, an output filter is implemented after the DAC output.

7.7 Output Circuit

A schematic of the output circuit is presented in Fig. 7.7. The output circuit consists of two stages, filtering with amplification, then a second amplification stage to increase the system gain. A second amplification was chosen since the first stage became unstable when a higher gain was used in a single amplifier/filter stage. For both the output and input circuits a single quad dual inline package (DIP) amplifier IC is used. The chosen IC is the OPA228 made by Texas Instruments. Further information about this IC is provided in the Input Circuit section.

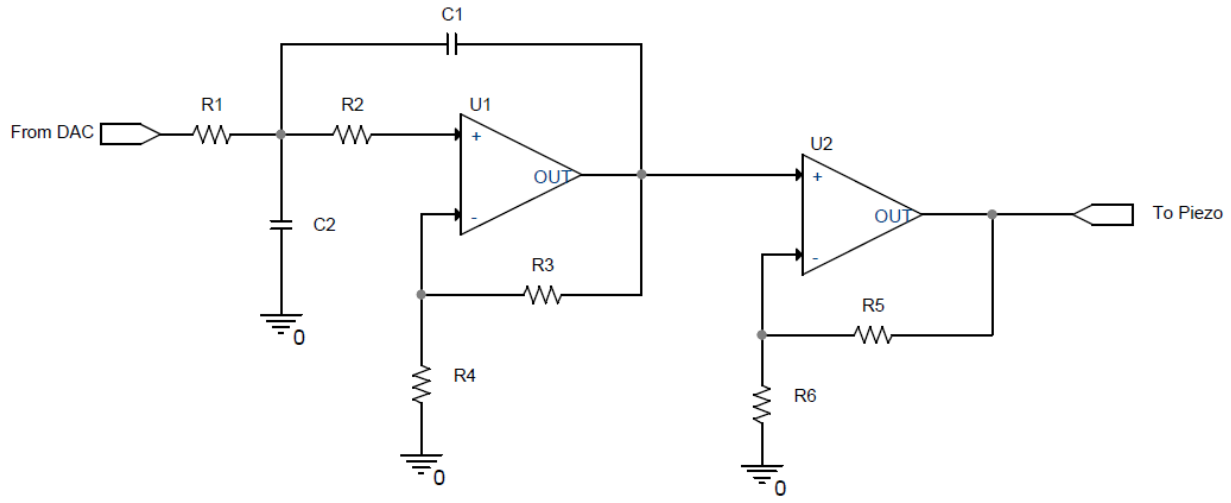

Figure 7.7: Schematic of Output Amplifier Circuit

A second amplification was chosen since the first stage became unstable when a higher gain was used in a single amplifier/filter stage. For both the output and input circuits a single quad dual inline package (DIP) amplifier IC is used. The chosen IC is the OPA228 made by Texas Instruments. Further information about this IC is provided in the Input Circuit section.

7.7.1 Output Filter

At the output of the DAC is a bandpass filter formed from an active low-pass filter (LPF) based on a single-pole, Sallen-Key topology [32] and a single pole RC high pass filter to cutoff DC. The LPF has a high frequency cut off of 106 kHz, with a gain of 2. Its main function is to remove high frequency noise introduced by the voltage stepping at the DAC output. The cutoff at 106 kHz ensures that the frequencies of interest are not cutoff, satisfying Requirement 2. The high-pass filter (HPF) is a simple RC filter whose function is to remove the DC bias at the DAC output. This is a necessary step since it is not understood what effect introducing a DC signal to the Piezo transducer would have on the pulse-echo response; moreover, all testing in the lab was performed

with a zero DC offset sinusoidal burst, and it was desired to have an equivalent signal on the field-testing board.

7.7.2 Output Amplifier

After the output filter, a second non-inverting amplification stage is used to further amplify the signal. The gain of this stage was selected to be 2.8 V/V. After a 2 V/V gain in the previous stage and given a voltage swing of 3.3 Vpp at the analog output, the maximum voltage swing over the two amplification stages is 18.5 Vpp. This is the voltage swing delivered to the Piezo Out BNC connector.

7.7.3 Piezo Out

The pulse signal is transferred to the Piezo transducer using a BNC connector. This connector was chosen for easy connection to oscilloscopes for system testing.

7.8 ADC Implementation

7.8.1 Configuration of ADCK

The ADC clock frequency ADCK configurable and can be changed to fit a variety of different applications. The ADCK is derived from the data bus clock, which in turn is derived from the system clock. The master clock is configurable from the Arduino graphic user interface (GUI). While the Kinetis chip is rated for a system clock of 180 MHz, overclocking is permitted and is achievable from the GUI. For our application 240 MHz and 192 MHz master clocks were tested during development. If the 240 MHz master clock is selected, the bus clock is then configured to

be 80 MHz, If the 192 MHz master clock is selected, the bus clock is automatically configured to be 48 MHz. For both cases the ADCK is derived from the bus clock by dividing it by 4. The configuration of the bus clock relative to the system clock is software configurable in the library file *kinetis.h*. The configuration of the ADCK relative to the bus clock is configurable in software through the library file *ADC.h*.

7.8.2 Determination of ADC Sampling Frequency from ADCK

The datasheet for the Kinetis MCU gives the following formula for the conversion speed of the ADC based on its clock frequency [30]:

$$T_{Conversion} = SFC_{Adder} + N_{AVG}(BCT + LST_{Adder} + HSC_{Adder}) \quad (7.4)$$

The total conversion time from (7.4), is then 22 ADCK cycles. Thus, for the 20 MHz ADCK the total conversion time is expected to be 1.1 $\mu s/sample$, and for the 24 MHz ADCK, this sampling period is expected to be 0.92 $\mu s/sample$. It would seem that a faster ADCK time would be more desirable, since it would result in faster sampling rates. However, if the jitter is increased with a faster ADCK speed, then this higher sampling rate is not good for our application. A test of the two clock frequencies is presented in the testing and results section.

7.9 Input Circuit

The input circuit consists of 5 stages, including: an input HPF, an amplifier stage, a voltage clipping circuit, an output HPF, a biasing circuit, and the ADC input. Like the output circuit, the input circuit makes use of the same OPA228 IC and makes use of a bandpass filter. The input

circuit, complete with a bandpass filter and voltage amplifier, was designed to meet Requirement 6. Since the input signal is sensitive to noise, and due to the large gain of the amplifier, a full noise analysis of the input circuit is presented in the next chapter. A schematic of the input circuit is presented in Fig. 7.8.

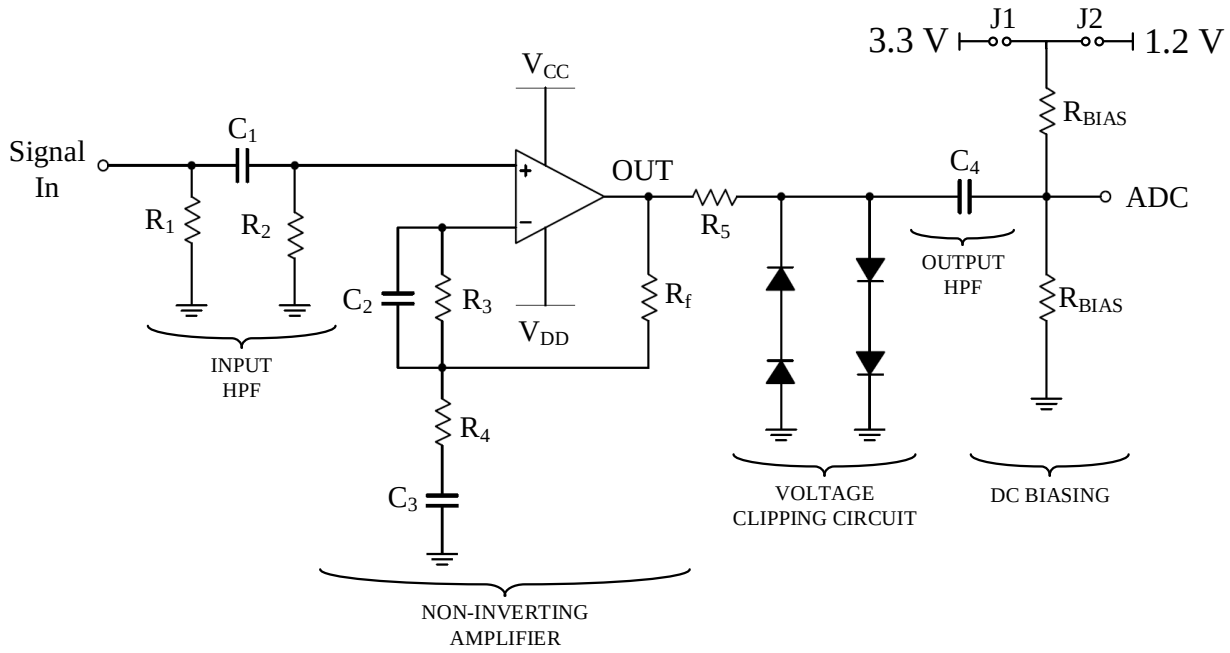

Figure 7.8 Schematic showing the implementation of the input circuit conditioning the signal from the piezo transducer

7.9.1 Piezo In

The echo signal from the piezo transducer is also implemented using a BNC connector. This was chosen so that signals from a function generator could easily be injected for system testing.

7.9.2 Input Filter 1

At the signal input, an RC high pass filter is used to cutoff any DC that may be present in the signal before amplification. The low frequency cutoff of the HPF, with $R_1||R_2 = 100\ k\Omega$ and $C_1 =$

3.2 nF is f = 4.97 kHz from (7.6). This filter constitutes the low frequency cutoff of the input circuit bandwidth.

7.9.3 Input Amplifier

The second stage is an NIA with a calculated gain of 101, and a measured gain of 120, which meets the first part of Requirement 4. The bandwidth of the input circuit is dependent on the high frequency cutoff of the amplifier, which in turn depends on the on the Gain Bandwidth Product (GBW) of the OPA228. The datasheet of the OPA228 specifies a 33 MHz GBW, and dividing the GBW by the gain gives a high frequency cutoff $f_{cutoff} = 275\ kHz$. As described in [33], the equivalent system bandwidth can be found according to (7.5).

$$B = \frac{\pi}{2}\frac{{f_2}^2}{{f_1}^2+{f_2}^2} \tag{7.5}$$

With f_1 being the lower cutoff of the input HPF, and f_1 the upper cutoff of the amplifier. The combined bandwidth is calculated to be 270 kHz.

7.9.4 Input Filter 2

The second input filter removes any added DC from the output of the amplifier. Any DC bias present in the signal after the amplifier is the result of input offset voltage at the amplifier input, being multiplied by the system gain and appearing at the output.

The low frequency cut-off of the input amplifier can be found from the following relationship [33]:

$$f = \frac{1}{2\pi RC} \tag{7.6}$$

With $R = 100\ k\Omega$ and $C_4 = 1\ nF$, the low frequency cutoff of the HPF at the output of the input circuit is f = 3.2 kHz, and the overall bandwidth of the input circuit is unchanged.

7.9.5 Clipping Circuit

A voltage clipping circuit acts as a protection against overvoltages at the ADC pin by limiting the voltage according to $|V_{clip}| \geq 3.3\ V$. The diodes are readily avaible in the tech shop and have a rated forward voltage of 1.6 V. The diodes are placed in series to ensure that the ADC input voltage is not greater than 3.2 V. Therefore, the clipping circuit accomplishes Requirement 11.

7.9.6 Biasing Circuit

The signal has a DC bias added back to the signal equal to $V_{REF}/2$, where V_{REF} is the selected analog reference voltage for the ADC. On the PCB this voltage a jumper connect connects either 1.2 V or 3.3 V to the V_{Ref} node shown in the figure. The reference voltage is selected according to what voltage range is desired for sampling. For sampling on the range of [0V,1.2V], J2 should be connected, and if the range for sampling is [0 V, 3.3 V], the J1 should be selected. In software the two different ranges are selected by configuring the internal voltage reference used the ADC. The reference voltage was designed to be selectable to meet Requirement 12. For information on the software configuration of the ADC reference voltage see the software section.

7.9.7 ADC Input

The final stage of the input circuit is the PCB hardwired connection to A14 input on the Teensy board. This ADC input was chosen for its physical proximity to the ADC input node on the PCB.

7.10 PCB Implementation

The transceiver system was developed and tested using a solderless breadboard. After finalizing the design and establishing proof of concept, the board was moved to a PCB. A picture showing the final PCB design is shown in Fig. 7.9. The PCB was designed through KiCAD, an open source PCB design software with a diverse component library. The PCB was designed with two different ground supplies, one for the input/output signal electronics, and other for the power supply electronics. The Teensy board itself provides two different ground pins, one for analog ground and one for digital ground. The analog ground of the Teensy board is connected to the input/output signal electronics and the digital ground is connected to the power supply electronics.

Figure 7.9: PCB Implementation of the Pulse-Echo Transceiver system

Test points were placed in strategic locations on the breadboard to make future testing and diagnostics of the breadboard easier. These test points were placed at a variety of locations,

including the 3 different voltage supplies, the DAC output, the output filter, output amplifier, input filter, input amplifier, and ADC input. The test points are shown in the PCB diagram as the relatively large silver pads. The physical dimensions of the PCB were chosen such that it would fit inside a purchased plastic enclosure. The screw holes on the PCB were positioned to align with the enclosure, and so that the physical length and width of the PCB were also chosen such that it would sit comfortably inside it. The board and enclosure is shown in the figure.

7.11 Testing and Results

The full functionality of the input and output circuits were tested to make sure that the behavior observed was according to design. The full description of these tests and their respective results are discussed in the following sections.

7.11.1 DAC Testing

The output frequencies of the DAC were tested using a Frequency Counter. The results of this experiment are presented in the following section.

7.11.1.1 Frequency Measurement of DAC Output

This test was designed to verify the relationship described in (7.1) and (7.2). Using a Agilent 53132A Frequency Counter, the frequency of the output wave was measured for 40 different PIT load values ranging from 22 to 130. Since the 53132A requires a continuous signal, and since the board was designed to output a sinusoidal burst, the following modifications were applied to the firmware.

i. The PIT ISR was modified so that a continuous sinusoid was output of the DAC instead of the 5-cycle sinusoidal burst.

ii. The push button ISR was modified so that when the user pressed the push button, an integer index was incremented. After each press a new value was loaded into the PIT LDVAL register by using the integer index to cycle through an array of PIT load values.

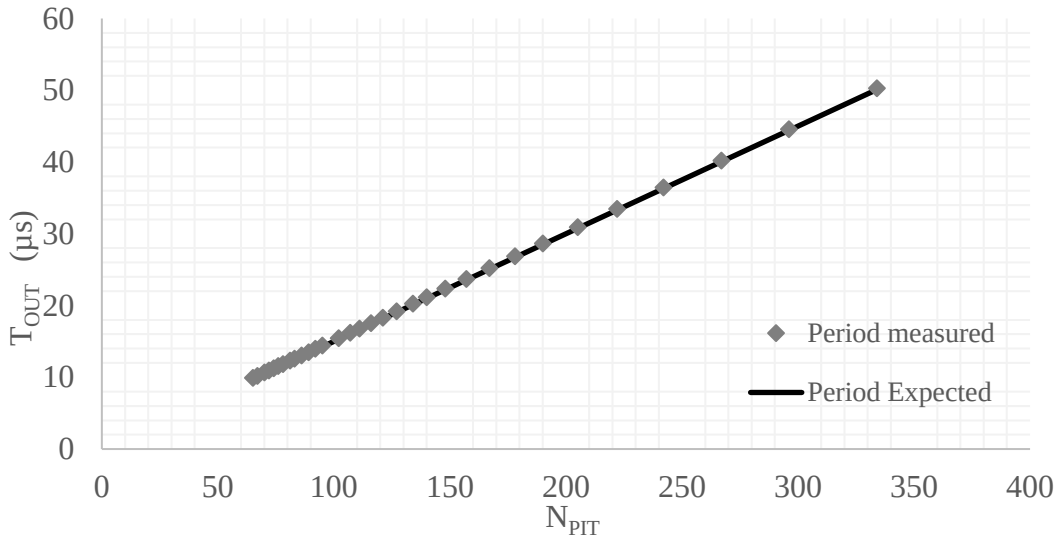

Figure 7.10 Results of frequency measurement experiment verifying the DAC Output

Then the inverse of frequency T_{out} was plotted against N_{PIT}. The results of this experiment are presented in Fig. 7.10, which compares the measured T_{out} with the expected T_{out} found from (7.2). The figure shows the period of the output signal vs the timer period. From the graph the measured relationship is in good agreement with the expected relationship. From the measurement it is observed that there is a constant offset between the measured and the expected result since the bus clock is not precisely 80 MHz.

7.11.2 ADC Jitter Testing

The ADC was tested to detect the presence of any jitter in the ADC clock (ADCK) signal. Two different ADCK frequencies were compared to see the amount of jitter present when sampling at each frequency. The test involved sampling the same square pulse 50 times consecutively to check for repeatability in the sampled signal.

7.11.2.1 Sampling Repeatability Test

A function generator was used to generate a square wave pulse. The output of the function generator is connected directly to the ADC for sampling, and the sync output of the was connected to the trigger pad on the PCB. A hardware interrupt was enabled on the board which triggered an ISR at the falling edge for the signal on the trigger pad. An example output of the pulse signal and the associated sync signal is shown in Fig. 7.11.

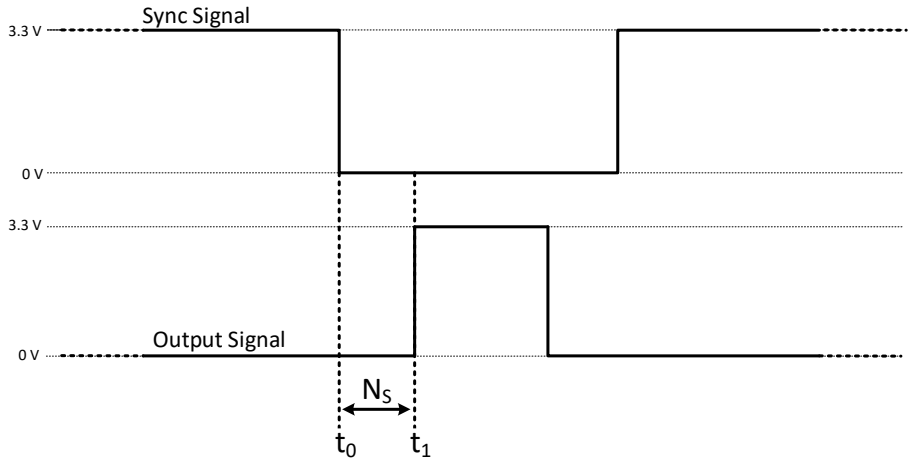

Figure 7.11: Diagram illustrating nature of the sampling repeatability test

The experiment begins when an ISR tied to the trigger pad is triggered at the falling edge of the Sync Signal, shown in Fig. 7.11 as t_0. Inside the trigger ISR, ADC interrupts are enabled, and the

ADC thereafter begins taking and storing samples of the Output Signal. The ADC continues to sample until 2500 samples have been taken, at which time the ADC interrupts are turned off. The samples are stored to a file on the SD card, completing one iteration. This process is repeated 50 times, where each successive iteration is stored to its own file on the SD card. The results were analyzed to determine the sample number at which the rising edge of the output signal was recorded N_s. Jitter was then quantified according to the variation in N_s over the 50 tests. The 50 tests were repeated for 7 different duty cycles of the square wave pulse, ranging from 20% to 80%. Both ADCK sampling frequencies were tested using this procedure. The results are presented in the following section.

7.11.3 Results of Sampling Repeatability Test

The results of three of the tests for each ADCK are presented. These three tests represent the typical jitter response, the best jitter response and the worst-case jitter response. The results are presented in the Figs 7.12-7.17.

7.11.3.1 Results of Testing for 20 MHz ADCK

These results show that the 20 MHz ADCK consistently show low jitter. The ADC samples the rising edge of the output signal within 1 sample over the 50 tests, for each duty cycle of the output signal.

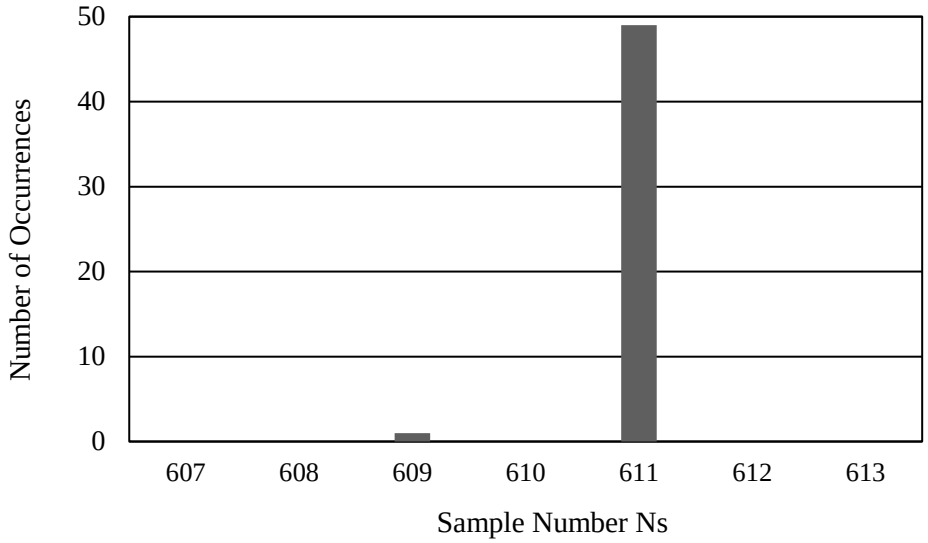

Figure 7.12: Typical-case response of Jitter Test for ADCK = 20 MHz, 20% Duty Cycle

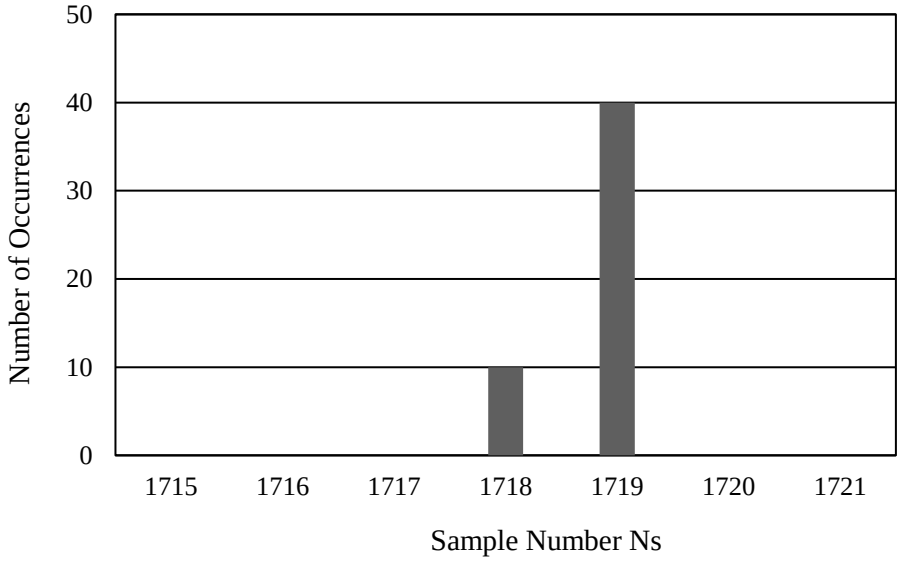

Figure 7.13: Worst-case response of Jitter test for ADCK = 20 MHz, 70% Duty Cycle

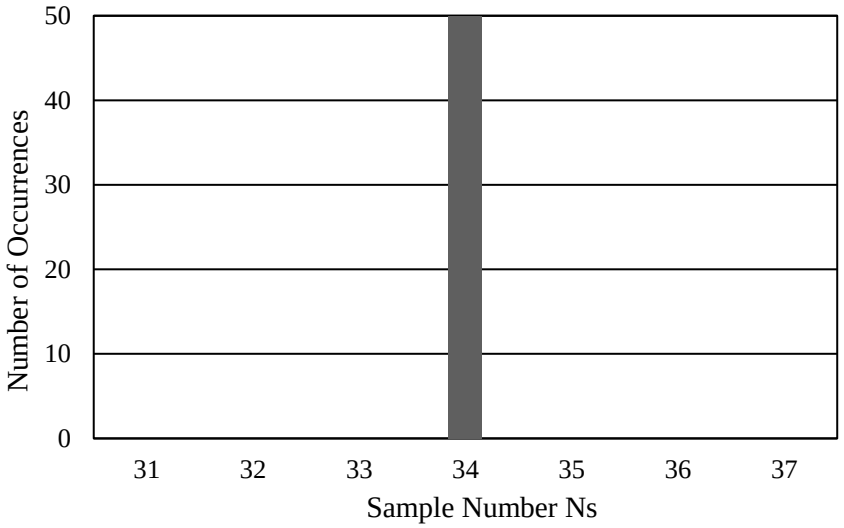

Figure 7.14: Best-case response of Jitter test for ADCK = 20 MHz, 50% Duty Cycle

7.11.3.2 Results of Testing for 24 MHz ADCK

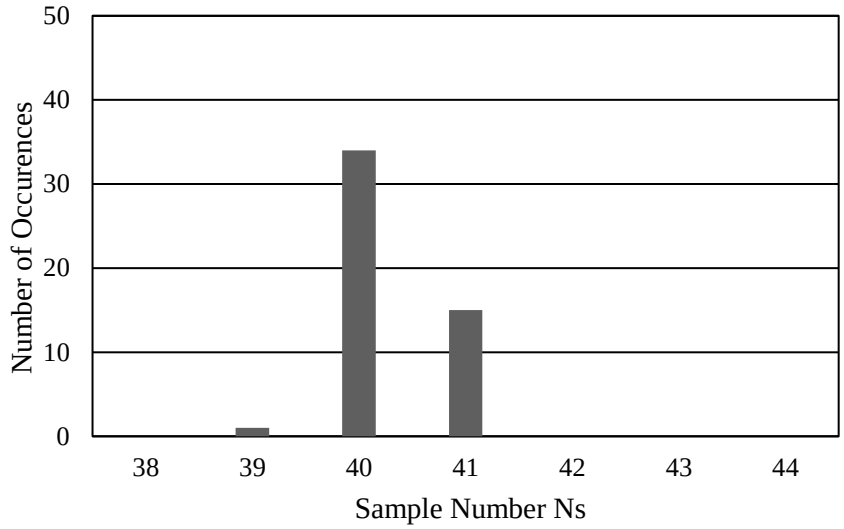

Figure 7.15: Typical-case response of Jitter Test for ADCK = 24 MHz, 50% Duty Cycle

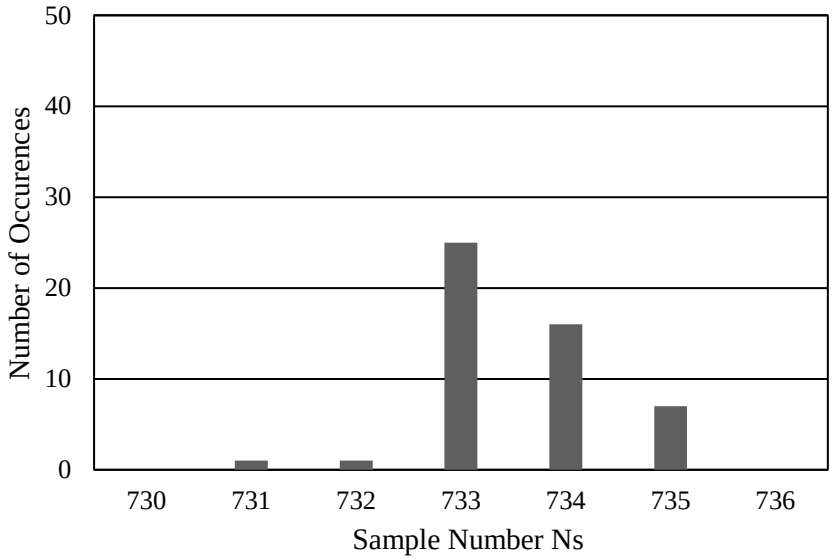

Figure 7.16: Worst-case response of Jitter test for ADCK = 24 MHz, 20% Duty Cycle

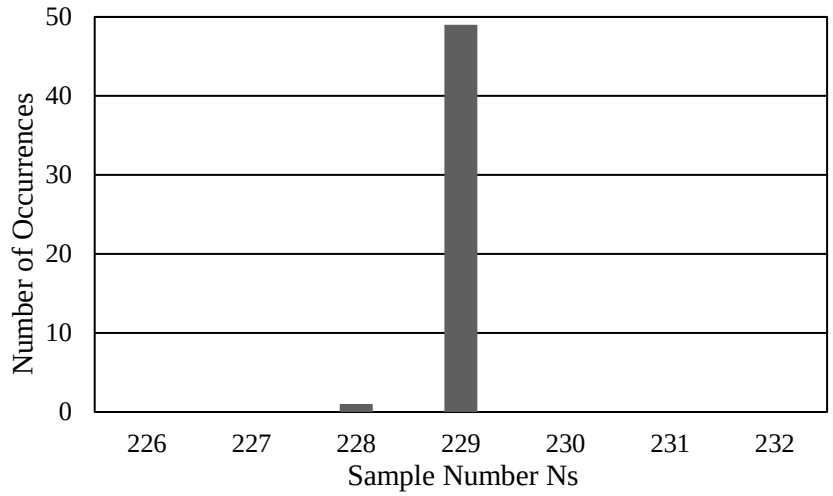

Figure 7.17: Best-case response of Jitter test for ADCK = 24 MHz, 40% Duty Cycle

These results show that the 24 MHz ADCK consistently show relatively large jitter in comparison to the 20 MHz ADCK. The ADC samples the rising edge of the output signal within 1 sample in only one of the duty cycles for 50 tests. Typically, the ADC samples the rising edge within three samples. In the worst case, the ADC samples the rising edge of the output signal within 5 samples.

We conclude that sampling at 20 MHz is the better option as the jitter is very low. From these results we are confident in its reliability for our application.

7.12 Comparison of Pulse-Echo Measurements with Digital Oscilloscope

The Pulse-Echo Transceiver board is compared with the digital oscilloscope for a pulse-echo measurement using the CRAS sensor for the three different rods. The results of the comparison for Rod A at 32.5, 40 and 50 kHz are presented in Fig. 7.18 – 7.20.

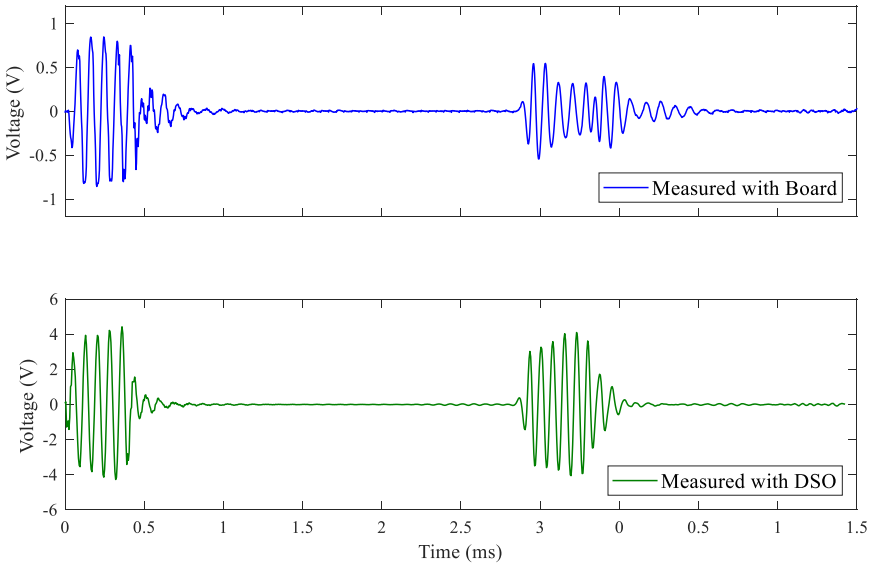

Figure 7.18: Comparison of board measurement to oscilloscope for Rod A at 32.5 kHz

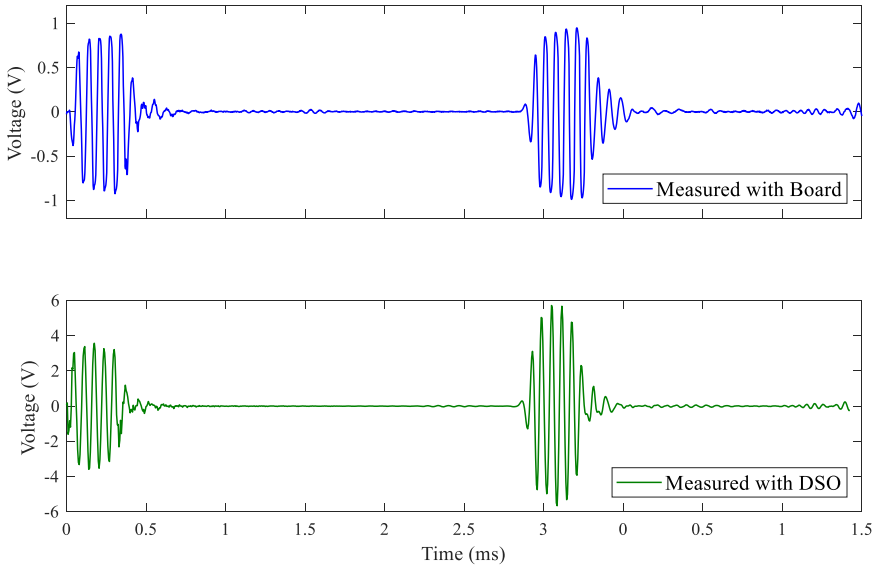

Figure 7.19: Comparison of board measurement to oscilloscope for Rod A at 40 kHz

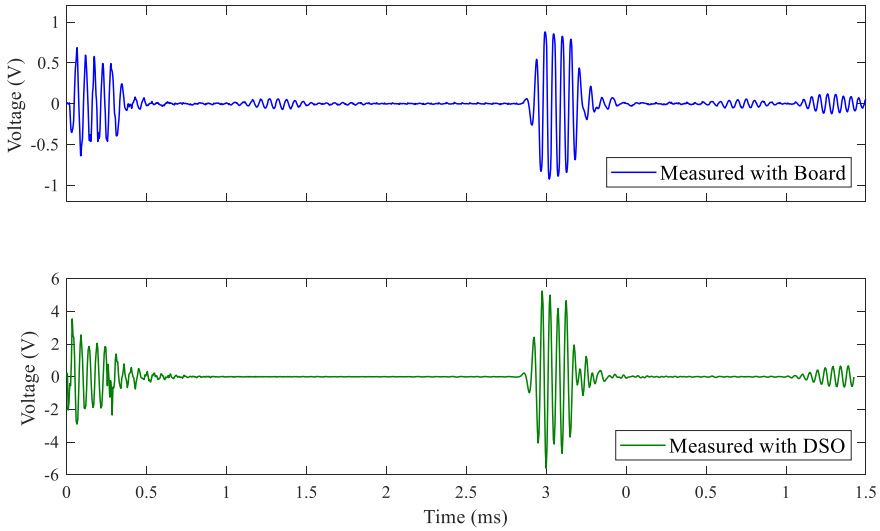

Figure 7.20: Comparison of board measurement to oscilloscope for Rod A at 50 kHz

The results of the comparison for Rod D at 32.5, 40 and 50 kHz are presented in Fig. 7.21 – 7.23.

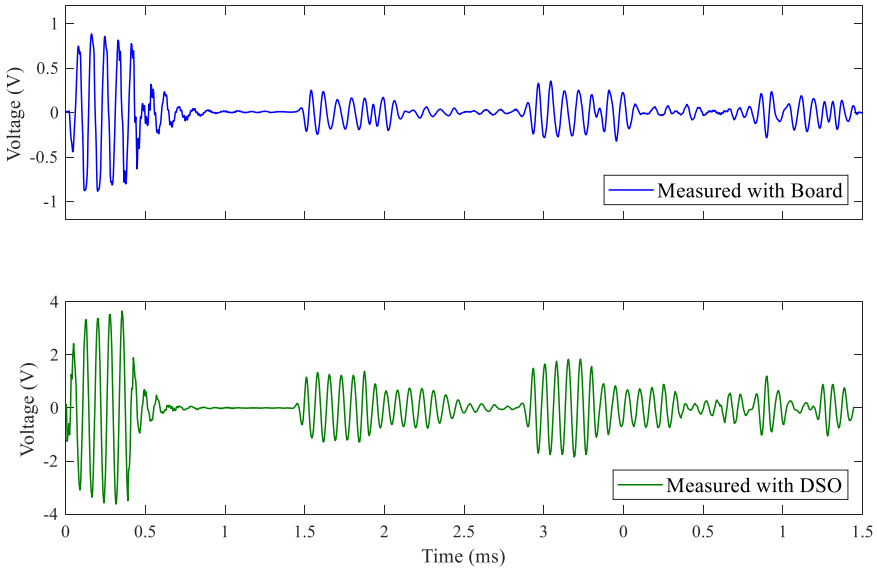

Figure 7.21: Comparison of board measurement to oscilloscope for Rod D at 32.5 kHz

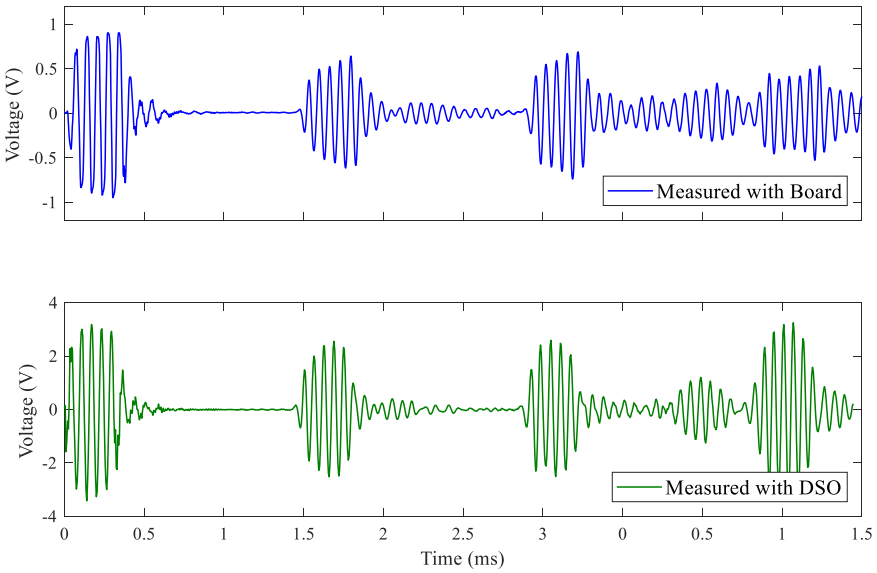

Figure 7.22: Comparison of board measurement to oscilloscope for Rod D at 40 kHz

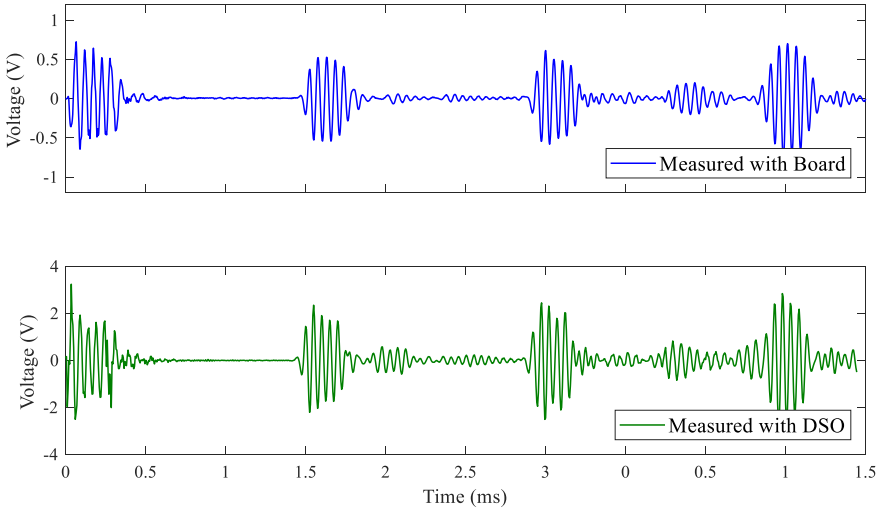

Figure 7.23: Comparison of board measurement to oscilloscope for Rod D at 50 kHz

Finally, the results of the comparison between the board and the oscilloscope using Rod E are presented in Fig. 7.24 – 7.26.

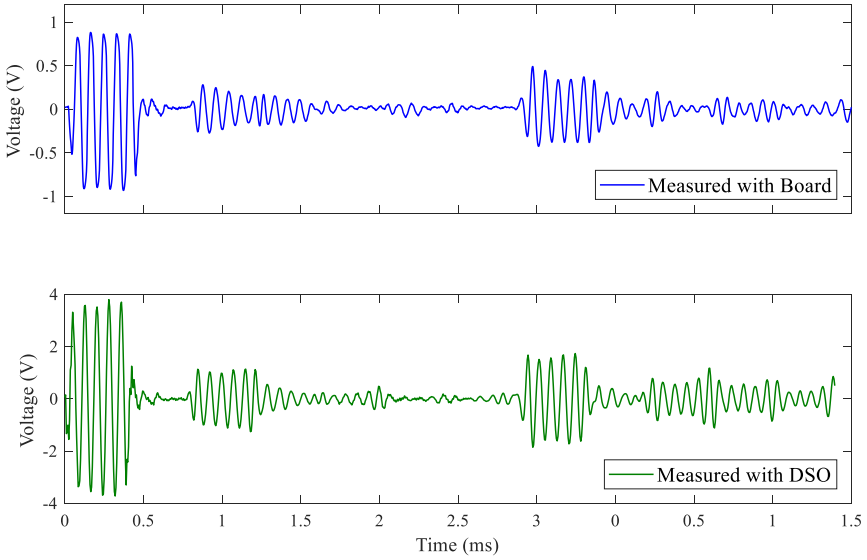

Figure 7.24: Comparison of board measurement to oscilloscope for Rod E at 32.5 kHz

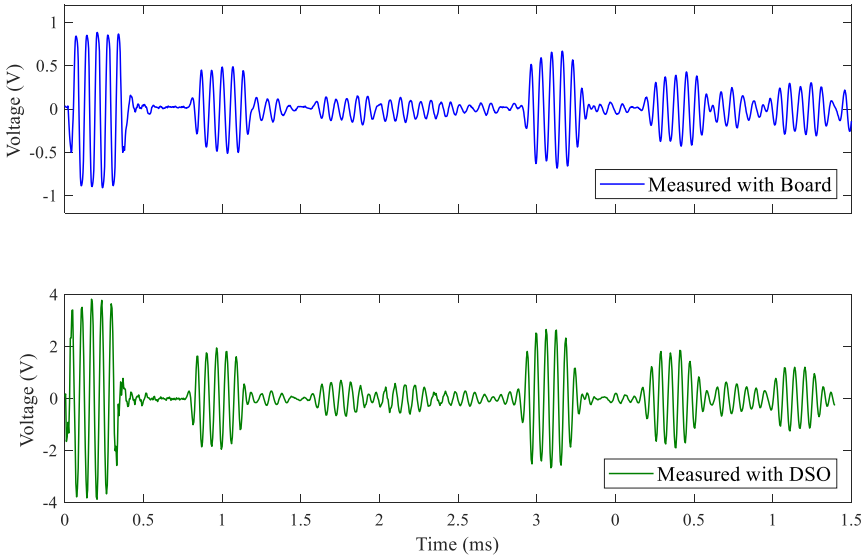

Figure 7.25: Comparison of board measurement to oscilloscope for Rod E at 40 kHz

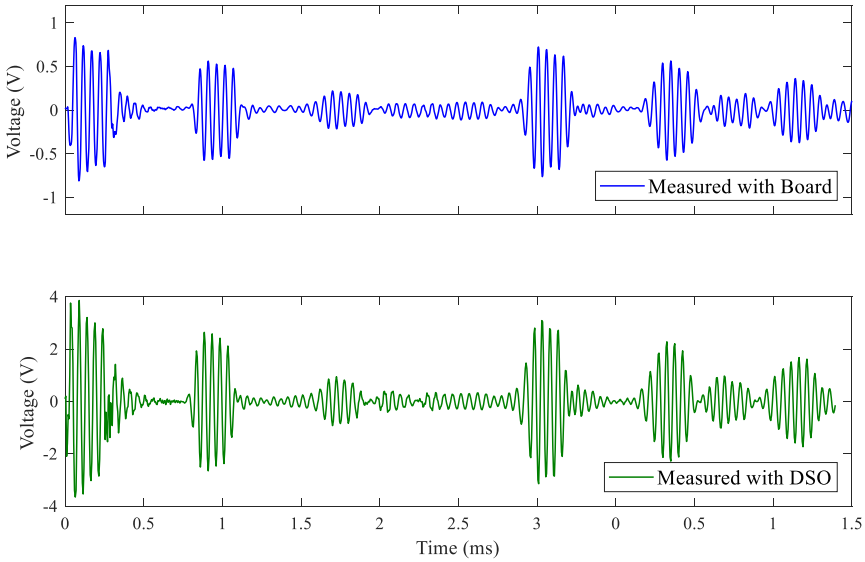

Figure 7.26: Comparison of board measurement to oscilloscope for Rod E at 40 kHz

7.13 Conclusions

The results obtained from using the Pulse-Echo Transceiver Board are in close agreement with the results obtained from the results obtained using the Digital Signal Oscilloscope. The measured results with the board have smaller signal levels received than the signals recorded by the oscilloscope, despite the transmitted signals being identical. An explanation for the discrepancy between the board and oscilloscope measurements are not immediately clear and are the topic of future discussion.

8 Conclusions and Future Work

A model for a defect detection system has been developed and implemented using PSpice software. The model is based on the controlled source electrical analogous circuit model developed by Leach. In developing the complete system model, first an idealized, lossless model was developed as a basis. To verify the model, an experiment involving a symmetrically-driven pair of steel rods was used to demonstrate that the model reproduced the major features of the signal generated in lab testing. The initial model revealed that in order to implement a model with real-world significance, loss needed to be taken into account, a precise determination of the piezoelectric parameters was required.

A suitable sensor for defect detection was developed and tested. Three different configurations were tested in the process of developing a transducer suitable for defect detection in a steel rod. The clamped configuration, a mass-backed piezo and the CRAS configuration, all demonstrated effective defect detection. However, the CRAS sensor was the configuration with the largest output-to-input ratio by far. The CRAS most effectively generated the first order longitudinal wave mode in the rod without adding other undesirable modes as observed in the mass-backed and clamped configurations. The CRAS was chosen as the best suited transducer configuration for defect detection in steel bars.

PSpice models for the standalone piezo transducer and the two CRAS variations were developed and tested. The piezoelectric parameters for the PZT transducer used in our experiments were determined using PRAP analysis software. Using the parameters from PRAP, a model of the standalone piezoelectric transducer was developed. The two sets of parameters obtained from

PRAP, were applied to the standalone sensor model and two different resonant curves were achieved for the modelled standalone piezo. Both impedance curves were in close agreement with the measured resonance curve of the piezo. The standalone piezo model was then combined with other elements to form PSpice models for the two CRAS variations. The CRAS models were verified through frequency and time domain testing, and the results were compared with those obtained in the lab. The results showed that model of the second CRAS variant was in strong agreement with the lab results. This close agreement was attributed to the fact that the second CRAS sensor does not have multiple resonances in close proximity to its resonant frequency of 40 kHz. The results obtained for the PSpice model of the first variant were not in close agreement with the lab results. This was attributed to the multi-resonance of the first CRAS sensor near its resonance frequency of 52 kHz, which could not be modelled. We concluded that the second CRAS sensor was the more suitable sensor to be used for future systems involving defect detection in grounding rods.

The model developed for the CRAS transducer was extended to model defect detection in grounding rods. Three grounding rod analogs, Rods A, D and E, were modelled in PSpice and connected in series with the CRAS model. The three rod models were tested with identical stimuli for three different frequencies, 32.5 kHz, 40 kHz, and 50 kHz. The results showed that the model demonstrated close agreement with the measurements obtained in the lab. However, the modelled defects resulted in simulation results that were not in close agreement to the measured behavior. Further development of the model for the rods, and in particular their defects, is an important consideration for future work.

The results obtained from using the Pulse-Echo Transceiver Board are were in close agreement with the results obtained using the Digital Storage Oscilloscope. The measured results with the board have smaller signal levels received than the signals recorded by the oscilloscope, despite the transmitted signals being identical. An explanation for the discrepancy between the board and oscilloscope measurements are not immediately clear and are the topic of future discussion.

References

[1] "IEEE Guide for Safety in AC Substation Grounding," *IEEE Std 80-2013 (Revision IEEE Std 80-2000/ Inc. IEEE Std 80-2013/Cor 1-2015)*, pp. 1–226, May 2015.

[2] "IEEE Guide for Measuring Earth Resistivity, Ground Impedance, and Earth Surface Potentials of a Grounding System," *IEEE Std 81-2012 (Revision IEEE Std 81-1983)*, pp. 1–86, Dec. 2012.

[3] J. Krautkrämer and H. Krautkrämer, *Ultrasonic testing of materials*. Springer Science & Business Media, 2013.

[4] K. F. Graff, *Wave motion in elastic solids*. Courier Corporation, 2012.

[5] M. Shoji and A. Hirata, "Ultrasonic guided wave testing of anchor rods embedded in soil," in *2016 IEEE International Ultrasonics Symposium (IUS)*, 2016, pp. 1–4.

[6] M. Shoji and Y. Higashi, "Fundamental study on guided wave testing of cylindrical bars embedded in soil," in *Ultrasonics Symposium (IUS), 2014 IEEE International*, 2014, pp. 1404–1407.

[7] U. Amjad, S. K. Yadav, and T. Kundu, "Detection and quantification of diameter reduction due to corrosion in reinforcing steel bars," *Struct. Heal. Monit.*, vol. 14, no. 5, pp. 532–543, 2015.

[8] Z. Zheng and Y. Lei, "Effects of concrete on propagation characteristics of guided wave in

steel bar embedded in concrete," *Shock Vib.*, vol. 2014, Aug. 2014.

[9] S. Sharma and A. Mukherjee, "Longitudinal guided waves for monitoring chloride corrosion in reinforcing bars in concrete," *Struct. Heal. Monit.*, vol. 9, no. 6, pp. 555–567, Nov. 2010.

[10] S. Sharma and A. Mukherjee, "Monitoring freshly poured concrete using ultrasonic waves guided through reinforcing bars," *Cem. Concr. Compos.*, vol. 55, pp. 337–347, Nov. 2015.

[11] B. L. Ervin and H. Reis, "Longitudinal guided waves for monitoring corrosion in reinforced mortar," *Meas. Sci. Technol.*, vol. 19, no. 5, p. 55702, Apr. 2008.

[12] B. L. Ervin, D. A. Kuchma, J. T. Bernhard, and H. Reis, "Monitoring corrosion of rebar embedded in mortar using high-frequency guided ultrasonic waves," *J. Eng. Mech.*, vol. 135, no. 1, pp. 9–19, 2009.

[13] W. M. Leach, "Controlled-source analogous circuits and SPICE models for piezoelectric transducers," *IEEE Trans. Ultrason. Ferroelectr. Freq. Control*, vol. 41, no. 1, pp. 60–66, Jan. 1994.

[14] N. Pérez, F. Buiochi, M. A. Brizzotti Andrade, and J. C. Adamowski, "Numerical characterization of piezoceramics using resonance curves," *Materials (Basel).*, vol. 9, no. 2, p. 71, 2016.

[15] M. Redwood, "Transient performance of a piezoelectric transducer," *J. Acoust. Soc. Am.*, vol. 33, no. 4, pp. 527–536, 1961.

[16] S. Sherrit and B. K. Mukherjee, “Characterization of piezoelectric materials for transducers,” *arXiv Prepr. arXiv0711.2657*, 2007.

[17] W. P. Mason, *Physical acoustics: principles and methods*. Academic press, 2013.

[18] R. S. Dahiya, M. Valle, and L. Lorenzelli, “SPICE model for lossy piezoelectric polymers,” *IEEE Trans. Ultrason. Ferroelectr. Freq. Control*, vol. 56, no. 2, pp. 387–395, 2009.

[19] A. Puttmer, P. Hauptmann, R. Lucklum, O. Krause, and B. Henning, “SPICE model for lossy piezoceramic transducers,” *IEEE Trans. Ultrason. Ferroelectr. Freq. Control*, vol. 44, no. 1, pp. 60–66, 1997.

[20] G. E. Martin, “Determination of Equivalent-Circuit Constants of Piezoelectric Resonators of Moderately Low Q by Absolute-Admittance Measurements,” *J. Acoust. Soc. Am.*, vol. 26, no. 3, pp. 413–420, 1954.

[21] H. Antlinger, R. Beigelbeck, S. Clara, S. Cerimovic, F. Keplinger, and B. Jakoby, “Investigation and Modeling of an Acoustoelectric Sensor Setup for the Determination of the Longitudinal Viscosity,” *IEEE Trans. Ultrason. Ferroelectr. Freq. Control*, vol. 63, no. 12, pp. 2187–2197, Dec. 2016.

[22] D. Zhao Junhui; Thomson, “No Title.” Jul-2018.

[23] T. T. S. Inc., “Piezoelectric Resonance Analysis Program (PRAP).” .

[24] D. M. Pozar, “Microwave Engineering 3e,” *Tramsmission Lines and Waveguides*, pp. 143–149, 2005.

[25] D. J. Jones, S. E. Prasad, and J. B. Wallace, “Piezoelectric materials and their applications,” in *Key Engineering Materials*, 1996, vol. 122, pp. 71–144.

[26] N. A.-H. K. M. C. T. D. Zhao Junhui; Durham, “Investigation on Acoustic Guided Waves based Techniques for Detecting Corrosion Damage of Electrical Grounding Rods,” 2018.

[27] “Piezo Material Properties,” no. SMD15T12S412. 2018.

[28] “High Temperature Ultrasonic Couplant,” no. Sono 600. 2014.

[29] R. Stoffregen Paul; Coon, “Teensy Microcontrollers.” .

[30] “K66 Sub-Family Reference Manual,” no. MK66FX1M0VMD18. 2015.

[31] G. Radulov, P. Quinn, H. Hegt, and A. H. M. Van Roermund, *Smart and flexible digital-to-analog converters*. Springer Science & Business Media, 2011.

[32] A. S. Sedra and K. C. Smith, *Microelectronic circuits*, vol. 1. New York: Oxford University Press, 1998.

[33] P. Horowitz and W. Hill, *The art of electronics*. Cambridge Univ. Press, 1989.